Universität Leipzig

Fakultät für Physik und Geowissenschaften
Abteilung Angewandte Quantensysteme

Study of cross polarizations and Landau-Zener transitions in the NV-P1-13C system for nuclear hyperpolarization

Master thesis

Fernanda Toledo
Matrikelnummer: 3710372

First evaluator:
Prof. Dr. Jan Meijer

Supervisor:
Dr. Ralf Wunderlich

i

Contents

Chapter 1

Motivation

Nuclear magnetic resonance (NMR) is a technique used in a wide range of disciplines such as medicine, explicitly MRI (magnetic resonance image) which is a non-invasive technique to observe anomalies in body tissues in order to detect pathologies. In biology and chemistry, the NMR technique is fundamental to determine the structure and functions of biological components and to perform chemical analysis in a broad range of substances.

This revolutionary technique was discovered in 1946 simultaneously by Edward Purcell at Harvard university and Felix Bloch at Stanford. Bloch's approach was in terms of dynamic macroscopic voltage signals induced by precession and the Faraday effect, whereas the Purcell group description was in optical terms of quantum mechanical susceptibility and absorption [1]. Both were awarded with the Nobel Prize in physics in 1952.

Principally, NMR measures the magnetic field originated by the Larmor precession of nuclear spins in the presence of an external magnetic field which induces the magnetization of the sample, this magnetization is the NMR signal,also called polarization, is proportional to the population difference between the states.

The action of increasing the polarization beyond thermal equilibrium is called nuclear Hyperpolarization, this can be attained through different mechanisms such as dynamic Hyperpolarization which can involve very high magnetic fields, cryogenic techniques and microwave fields , unfortunately these techniques can be expensive since they require special sets of equipment.

A relatively new approach to attain Hyperpolarization had became a promising technique which is possible to operate at room temperature. This method exploits one of the most important features of the negatively charged nitrogen vacancy centers (NV^-), which is the optical initialization through the irradiation of green laser light that enables the dynamic nuclear polarization techniques which can transfer the polarization of the (NV^-) centers to the ^{13}C nuclei.

In this work, we present a study of two Hyperpolarization techniques in a three spin system composed by two electron spins of NV^-, P1 and ^{13}C nuclear spin in the presence of external magnetic fields. These techniques are the Cross polarization technique and a technique based on inducing states transitions by employing time dependent magnetic fields which can be rationalized in terms of the Landau-Zener theory.

Chapter 2

Theory background

2.1 Diamond properties

The famous diamond is one of the allotrope forms of carbon, The diamond lattice is what is known as a *face centered cubic crystal structure* with a basis of two carbon atoms at each lattice point: one at (0,0,0) and the other at (1/4,1/4,1/4), where the coordinates are fractions along the cube sides, the diamond cubic cell belongs to the space group 226 or Fdbar3m [2]

Figure 2.1: Diamond unit cell [3]

The diamond cubic unit cell is composed by eight carbon atoms and each carbon atom is bonded via covalent bonds to the nearest four atoms (tetrahedrally coordinated) , the strength of the covalent bonds is what makes the diamond cubic order distinctly rigid and therefore the reason of its high hardness.

The hardness of diamond, between numerous properties of this material, has made it outstanding for a wide variety of applications in industry. Indeed, natural diamond is used as the maximum for the calibration of the Mohs (scratch-) hardness scale, on which it is assigned a value of 10 [2].Another notorious property is its thermal conductivity of 2300 W/m.K at room temperature (300 K), this value is four times the thermal conductivity of Copper. The diamond's thermal conductivity high value had been exploited by more than one industry, for example the gem and jewelry sector made use of this diamond property to create devices to differentiate between real and imitation diamonds.

The diamond thermal conductivity value in addition to its resistivity values from 10^{11} to 10^{18} $\Omega - m$ made it a promising material for electronic applications . In 2004 the discovery of superconductivity in boron-doped diamond synthesized at high pressure and high temperature were reported in [4].

The chemical inertness of diamond had a major impact in chemistry and biology, specifically the use of diamond films had led to the development of applications such as the development of biosensor, medical implants, electronic devices based on organic matter, etc.

Another property that makes diamond an attractive material is its transparency over a wide range of radiation wavelengths, this property has been exploited to produce windows and lenses for a broad variety of optical devices [5]

2.1.1 Artificial diamonds manufacture techniques

Due to the demand existing in industry and commerce for diamonds, two main techniques had been developed to achieve this goal will be described shortly in this subsection. High pressure high temperature (HPHT) synthesis operates as it name indicates to emulate the process through which natural diamonds are created. This technique proved its efficiency in 1955 when Bundy employed pressure vessel working up to 10 GPa under temperatures higher than 2000 °C [6]. Under such conditions, diamond is the thermodynamically stable allotrope of carbon, and therefore the phase transition of graphite to diamond is enabled.The diamond type Ib is the most common type produced with this technique, with longer and controlled growth periods the production of type Ib single crystals are also possible. The HPHT method is the favorite in industry because of its low production cost .The main disadvantage of this technique is its inability to produce diamonds with low impurities concentration (nitrogen) [7]. In contrast to the HPHT technique, the chemical vapor deposition (CVD) technique can produce high purity diamonds. This technique consists in growing diamond from a hydrocarbon gas mixture. The main steps of this process in diamond consists in placing the material inside a vacuum chamber and heat it to a temperature around 800 °C and low pressure (1 to 27 kPa) until it vaporizes, then the chamber is filled with gases rich in carbon such as methane, the last will react with the substrate and the new material will settle, if impurities are going to be added there are added in adequate moments during the process. [8]

2.1.2 Classification of diamond

Even though diamond structure is remarkably rigid, it always has certain types of impurities which can include also other crystallographic defects (e.g vacancies, interstitial carbons), the classification of natural and synthetic diamonds is based on the presence and absence of nitrogen and how these nitrogen atoms are arranged. The types are divided in the following manner [9]:

- **Type I**: The dominant impurity is nitrogen, it absorbs in infrared and ultraviolet region.

    ◇ Type Ia : Contains aggregates of substitutional nitrogen up to 3000 ppm

        ∗ Type IaA : The substitutional nitrogen atoms are mostly located in the closest neighbor positions, forming pairs of nitrogen. Usually, it presents any fluorescence.

        ∗ Type IaB : The nitrogen atoms are mostly located forming groups of four substitutional nitrogen atoms around a vacancy. Blue fluorescence is normally present

    ◇ Type Ib : The nitrogen impurities replace carbon atoms in the lattice (substitutional nitrogen) in an isolated manner, the nitrogen lead to a yellow colour fluorescence, the nitrogen concentration can

reach a maximum value of ≈ 500 ppm.

- **Type II**: Amount of nitrogen impurities is undetectable

    ◇ Type IIa : Its thermal conductivity is the highest and does not contain easily measurable nitrogen impurities as a consequence are colorless.

    ◇ Type IIb : This diamond type is also a *p-type* semiconductor due to the dominance of substitutional boron over the nitrogen impurities, this causes the diamond to exhibit a light blue color, it can also be colorless if concentration of boron is low.

2.1.3 Crystallographic defects in diamond

The crystallographic defects consist of substitutes of carbon, interstitial carbons and absent atoms also known as vacancies.

Both, artificial and natural diamonds usually contain defects. In the case of natural diamonds the substitutional defects can basically be nitrogen and boron. The defects can give color to the diamond even when present in very small quantities (in order of few ppm). The presence of boron gives diamond a blue color, the NV center can colour the diamond with a pink or purple color. In the case of Type Ib diamond, this is yellow colored due to the presence of single substitutional nitrogen also known as P1 centers.

P1 centers

As seen in section 2.1.2, the most abundant defect in Type Ib diamond is nitrogen. The P1 center is a neutral charged nitrogen atom formed by the displacement of a carbon in the diamond lattice. In addition, it has four possible orientations due to the Jahn-Teller distortion from T_d to C_{3v} symmetry [10] . The Hamiltonian of the P1 center in the presence of a magnetic field $\bar{B}$ oriented in Z direction can be described as follows:

$$H_{P1} = \gamma_{P1}\bar{B}.\bar{S}^{P1} + \bar{S}^{P1}\bar{\bar{A}}\bar{I}^{14N} \tag{2.1}$$

In the Hamiltonian , the terms $\bar{S}^{P1}$ and $\bar{I}^{14N}$ represent respectively the the P1 center (S=1/2) electron spin vector operator and the nuclear spin vector operator of its intrinsic isotope ^{14}N (I=1), this last is present in the Hamiltonian because of its natural abundance of 99.634% in contrast to the ^{15}N with an abundance of 0.366% .

The term $\bar{\bar{A}}$ is the anisotropic Hyperfine interaction tensor between the electron spin $\bar{S}^{P1}$ and the nuclear spin $\bar{I}^{14N}$. This tensor is composed by an axial component $A_{\parallel}=$ 114 MHz and a transverse component $A_{\perp} = 81$ MHz [11]

$$A^O = \begin{pmatrix} 81 & 0 & 0 \\ 0 & 81 & 0 \\ 0 & 0 & 114 \end{pmatrix} \tag{2.2}$$

The gyromagnetic ratio γ_{P1} can be taken in first approximation as the gyromagnetic ratio of the electron $\gamma = 28\,03$ MHz/mT.

2.2 NV center in Diamond

The NV center is a defect in the diamond lattice made up of a substitutional nitrogen atom and a first-neighbor vacancy in the lattice both situated along their symmetry axis [12] [13]. The defect has C_{3v} symmetry which means that it can be rotated into three equivalent rotations 120° and v refers to vertical symmetry plane. In the diamond, each carbon atom has four first neighbors that implies four different crystallographic axes ([111], [$\bar{1}\bar{1}1$], [$\bar{1}1\bar{1}$] and [$1\bar{1}\bar{1}$]) along which the NV center can be oriented, nonetheless the distinction between these orientations do not play any role in the spin properties of the NV center nor in their optical properties [14].
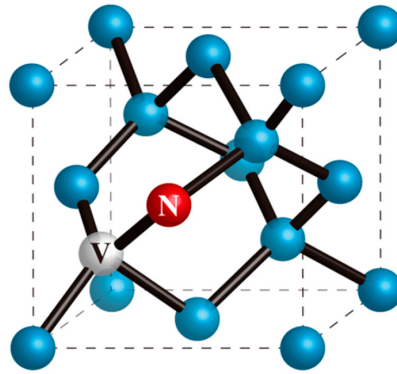

Figure 2.2: NV center in the diamond, the carbon atoms are depicted as blue spheres [15]
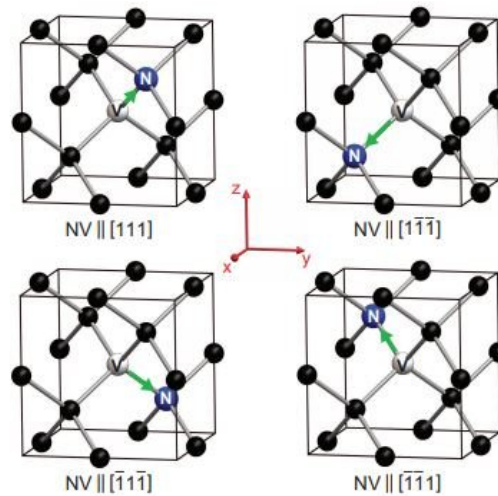

Figure 2.3: Four diamond orientations for the NV center [16]

2.2.1 NV⁻ electronic structure

The NV⁻ electronic structure is built from three carbon unpaired electrons (dangling bond electrons), which surround the vacancy, that contributes three valence electrons in total and the nitrogen atom that contributes with two electrons from their five valence electrons. In addition, an extra electron from neighbor donors gives a total of six valence electrons composes the NV⁻. Regarding its electron spin, its value is S = 1 [14].

The dynamic nuclear polarization methods presented in this master thesis depend on the remarkable properties of the negatively charged nitrogen-vacancy NV⁻ center. Therefore, **from this point, when mentioned NV**

center I refer to the NV⁻ center.

A description of the electronic structure of the NV center in the ground and excited states had been elaborated using *Ab initio* calculations and group theory. The electrons occupy four molecular orbitals with C_{3v} symmetry (u,v,e_x,e_y). These were constructed as orthonormal real linear combinations of the carbon atomic orbitals denoted as (a,b,c) and the nitrogen orbital denoted as d. The Hund's rule and Pauli exclusion principle are considered to fill up the ground state, the orbitals $\bar{u},u$ and $\bar{v},v$ are fully occupied and the e_x,e_y are each one occupied by an electron [13]. In the first excited state case, as shown the figure 2.5, the transition of an electron from $\bar{v}$ to one of the spins down orbitals $\bar{e}_x$ or $\bar{e}_y$ 2.4, the symmetry changes to C_{1h} due to the Jahn-Teller effect which involves the coupling between degenerate electronic states to degenerate phonon modes [17].

Schematic illustration of spin configurations for different charge states of NV center. Orange dotted horizontal line shows the relative position of the Fermi level EF .
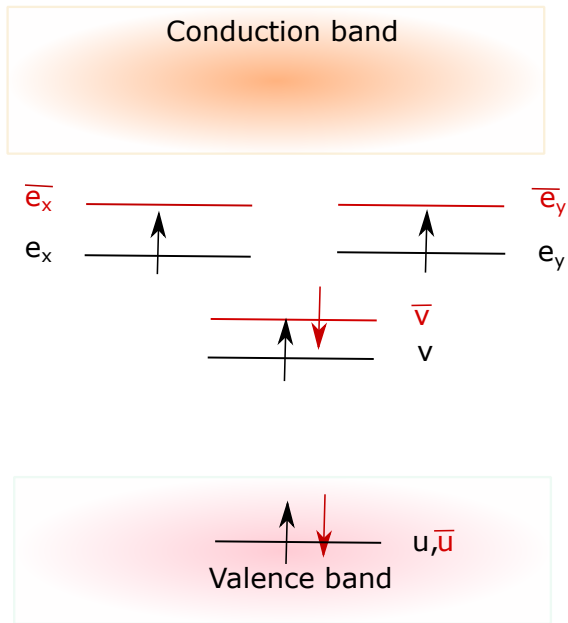

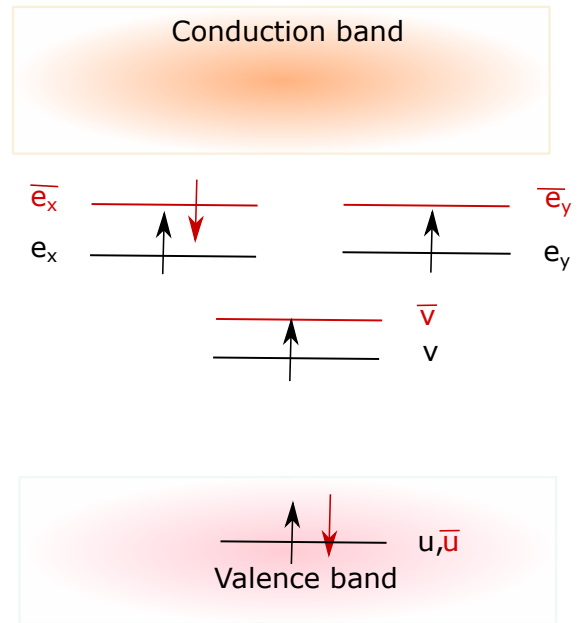**Figure 2.4:** NV⁻ center ground state spin configuration

Figure 2.5: NV⁻ center excited state spin configuration

NV⁻ Optical properties and dynamics

The theoretical description already mentioned in addition to the experimental results led to the energy diagram 2.6

The ground state is a spin triplet with orbital symmetry $^3A_2$, the excited state is also a spin triplet but with ^3E orbital symmetry. In the ground state, spin-spin dipolar interaction takes place between the unpaired electrons 2.4 causing the zero field splitting (ZFS) of value D_{gs}=2870 MHz between $m_s = 0$ and $m_s = \pm 1$. Similarly occurs in the excited state leading to a ZFS and a value of D_{es}=1420 MHz 2.5 [14]
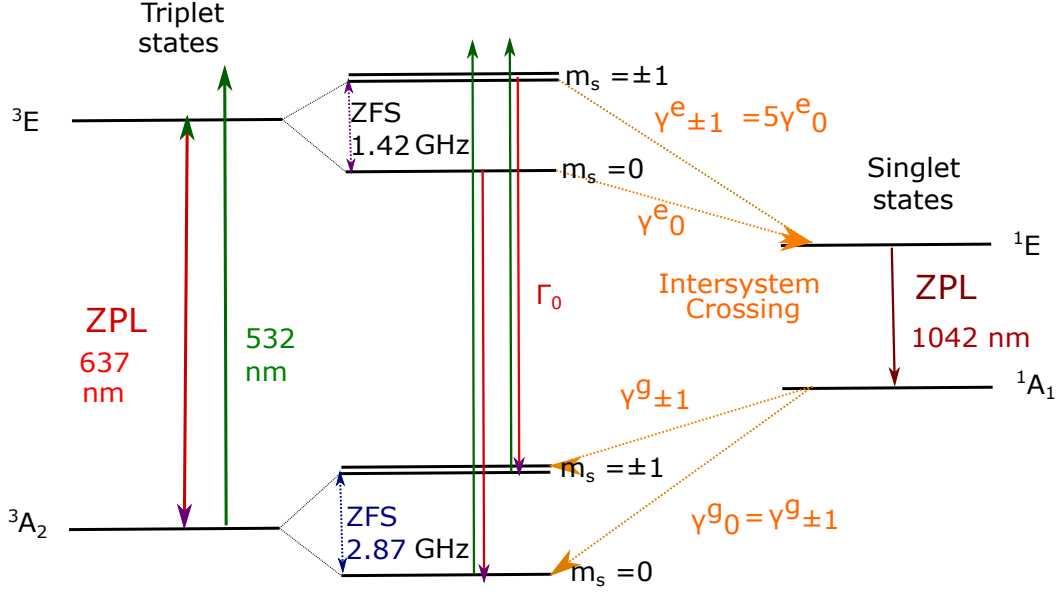
Figure 2.6: NV$^-$ energy levels diagram : Here, m_s denotes the electron spin-projection quantum number. The relaxation rates from the singlet state ^1E to the triplet ground state $^3A_2$ are represented by γ_0^g and $\gamma_{\pm1}^g$, while γ_0^e and $\gamma_{\pm1}^e$ are the correspondent from the triplet excited state ^3E to the singlet state $^1A_1$ [8][18]

Under laser illumination the optical properties and spin dynamics of the NV$^-$ center are revealed. The green laser irradiates the NV$^-$ center driving the ground state to the excited state. Radiative transition decay path to the ground state triplet $^3A_2$ from the excited state ^3E is characterized by the emission of a photon in the red visible spectrum region, also it is spin conserving . Conversely, the decay path via the metastable singlet states ^1A and ^1E also known as inter system crossing (ISC) is spin non-conserving. For the $m_s = \pm1$ excited states the probability to go through ISC is significantly higher than for the $m_s = 0$ excited state, the relaxation rates depicted in orange color indicate this fact. As well the probability of decaying from the intermediate metastable states to the ground state $m_s = 0$ is also favored. Therefore, after a few optical excitation emission cycles a strong spin polarization of the ground state $m_s = 0$ spin sublevel is established [19]

The feature that makes possible the NV$^-$ *optical initialization (optical polarization)* is that no matter which is the initial state the probability of the NV$^-$ to decay to the $m_s = 0$ is favored, the transition rates are indicators of this feature. On the other hand, For the $m_s = \pm1$ excited states the probability to go through ISC is significantly higher than for the $m_s = 0$ excited state, this dominance of the ISC path makes the *optical readout* possible. This has been experimentally observed in photoluminescence experiments [20], as already mentioned the decay path between the ground and excited states is radiative in the visible region spectrum, conversely the ISC paths are non-radiative, therefore the $m_s = \pm1$ states are called *dark states* and $m_s = 0$ are called *bright states*, therefore, this last present a higher average fluorescence intensity [21]. In the figure 2.7 n_0 and n_{-1} show the accumulated number of response photons per ns for the systems with initial $m_s^{NV} = 0$ state and $m_s^{NV} = -1$ respectively, the difference is what distinguish the states between each other.
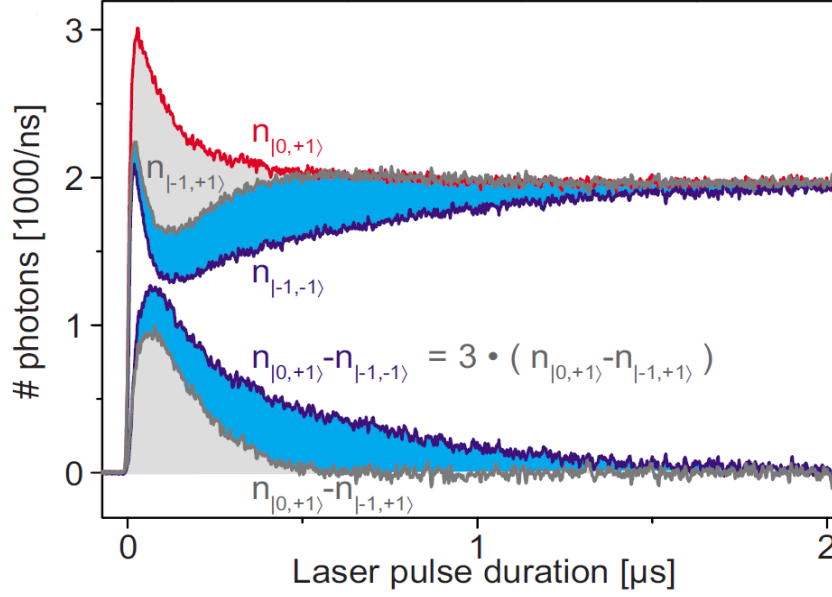
Figure 2.7: Optical readout of NV⁻ Fluorescence response. Obtained from [21]

2.3 Zeeman effect

In essence, the Zeeman effect can be described as a phenomena that electrons and nuclei undergo in the presence of a magnetic field. These particles possess a dipole moment associated with their angular momentum, therefore,in the presence of a magnetic field, they acquire additional energy which leads to a positive or negative shift in their original energy levels. In the case of degenerate energy levels in an atom, the Zeeman effect cause the split into more than one levels with different energy values.

The normal Zeeman effect is the name of the Zeeman effect that occurs for transitions between singlet states in which the spin is zero and the total angular momentum $\bar{J}$ is equal to the orbital angular momentum $\bar{L}$, conversely, the more general case, when $\bar{S} \neq 0$, is called Anomalous Zeeman effect.

2.3.1 Normal Zeeman effect

To treat the simplest case of the Zeeman effect it is appropriate to introduce the Hamiltonian of a particle with $S = 0$ in the presence of an homogeneous magnetic field B [22]

$$H_Z = \frac{1}{2m}(\bar{P} - \frac{q}{c}A)^2 + q\phi \tag{2.3}$$

Where A is the vector potential and ϕ the scalar potential of the electric field, m_e is the mass of the particle and q is its charge.

In order to simplify 2.3, the second term can be expanded as following:

$$\frac{1}{2m}(\bar{P} - \frac{q}{c}A)^2 = \frac{1}{2m}\left[\bar{P}^2 - \frac{q}{c}\bar{P}.\bar{A} - \frac{q}{c}\bar{A}.\bar{P} + \frac{q^2}{c^2}\bar{A}^2\right] \tag{2.4}$$

On the right hand, the third term is $\frac{q^2}{2mc^2}\bar{A}^2$ is not significant for atoms where $\langle L_z \rangle \neq 0$. For that reason, the only term that leads to the Zeeman Hamiltonian term ($\bar{H}_Z$) is $-\frac{q}{c}\bar{P}.\bar{A} - \frac{q}{c}\bar{A}.\bar{P}$.

8

In order to obtain the Zeeman Hamiltonian part of 2.3, the relation between the vector potential **A** and magnetic field **B** will be applied.

$$A_i(x) = -\frac{1}{2}\varepsilon_{ijk}x_j B_k \tag{2.5}$$

$$\begin{aligned}
\bar{P}.\bar{A} &= -\frac{1}{2}\bar{P}.(\hat{x}\times\bar{B}) \\
&= -\frac{1}{2}\bar{B}.(\bar{P}\times\hat{x}) \\
\bar{P}.\bar{A} &= \frac{1}{2}\bar{L}.\bar{B}
\end{aligned} \tag{2.6}$$

Where $\hat{L}$ is the angular momentum of the particle, as well, the term $\mathbf{A}.\hat{P}$ leads to the H_Z

$$\frac{q}{2mc}(\bar{P}.\bar{A}+\bar{A}.\bar{P}) = \frac{\mu_B}{\hbar}\bar{L}.\bar{B} \tag{2.7}$$

$$H_Z = \frac{\mu_B}{\hbar}\bar{L}.\bar{B} \tag{2.8}$$

In 2.8, the constant μ_B=5.788381 eV/T is the Bohr magneton.

In this regard, we can define the magnetic moment μ as :

$$\bar{\mu} = \frac{\mu_B}{\hbar}\bar{L} \tag{2.9}$$

2.3.2   Anomalous Zeeman effect

In this more general case we have the total angular momentum [23]:

$$\bar{J} = \bar{L} + \bar{S} \tag{2.10}$$

Where the total magnetic moment μ is represented as:

$$\bar{\mu} = -\frac{\mu_B}{\hbar}(\bar{L}+g\bar{S}) \tag{2.11}$$

In the last expression g is the Landé factor for the electron $g \approx 2$. With this new expression of the magnetic moment μ

$$H_Z = -\frac{\mu_B}{\hbar}(\bar{L}+g\bar{S}).\bar{B} \tag{2.12}$$

The energies associated with the Zeeman Hamiltonian H_Z are determined by the eigenvalues m_i of $\mathbf{L}+g\mathbf{S}$. This is the splitting of the energy levels that characterize the Zeeman effect.

2.4 Dipole-Dipole magnetic interaction

In the presence of an external magnetic field $\bar{B}$, the interaction between two particles is induced by their local interaction with the field [24]. In the classical description, the interaction energy between two particles separated by a vector of distance $\hat{r}$ the magnetic moments μ_1 and μ_2 is given by

$$E = \frac{\mu_0}{4\pi r^3}(\vec{\mu}_1 \cdot \vec{\mu}_2 - 3(\vec{\mu}_1 \cdot \hat{r})(\vec{\mu}_2 \cdot \hat{r})) \tag{2.13}$$

For a quantum mechanics interpretation, the Hamiltonian can be expressed when the magnetic moments are written in terms of their operators [25]

$$\bar{\mu}_1 = \gamma_1 \hbar \bar{I}_1 \qquad\qquad \bar{\mu}_2 = \gamma_2 \hbar \bar{I}_2 \tag{2.14}$$

Which leads to:

$$H_{dd} = \frac{\mu_0 \gamma_1 \gamma_2 \hbar^2}{4\pi r^3}(\bar{I}_1.\bar{I}_2 - 3(\bar{I}_1.\hat{r})(\bar{I}_2.\hat{r})) \tag{2.15}$$

The Hamiltonian can expressed in terms of the spin operators components, ladder operators $I_1^+, I_1^-, I_2^+, I_2^-$ and the polar coordinates (r, θ, ϕ) of the particles relative positions.
The ladder operators are given by:

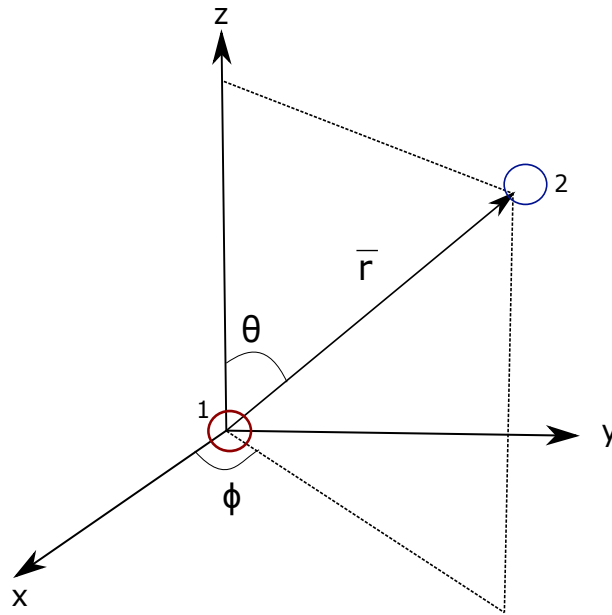$$I^+ = I_x + iI_y \qquad\qquad I^- = I_x - iI_y \tag{2.16}$$

Figure 2.8: Relative position r of two particles

$$H_{dd} = \frac{\mu_0 \gamma_1 \gamma_2 \hbar^2}{4\pi r^3} (A + B + C + D + E + F) \tag{2.17}$$

$$A = I_{1z} I_{2z} (1 - 3\cos^2 \theta)$$

$$B = -\frac{1}{4}(I_1^+ I_2^- - I_1^- I_2^+)(1 - 3\cos^2 \theta)$$

$$C = -\frac{3}{2}(I_1^+ I_{2z} - I_{1z} I_2^+) \sin \theta \cos \theta \exp\{-i\phi\}$$

$$D = -\frac{3}{2}(I_1^- I_{2z} - I_{1z} I_2^-) \sin \theta \cos \theta \exp\{i\phi\}$$

$$E = -\frac{3}{4} I_1^+ I_2^+ \sin^2 \theta \exp\{-2i\phi\}$$

$$F = -\frac{3}{4} I_1^- I_2^- \sin^2 \theta \exp\{2i\phi\}$$

Each term has certain effect, to describe what effect each term has let's considering that both magnetic moments 1 and 2 with $I = 1/2$ and quantum numbers m_1=1/2 and m_2=1/2. The term A is completely diagonal, commutes with the Zeeman Hamiltonian, and connects $|m_1 m_2\rangle$ to $\langle m_1 m_2|$. The term B connects $\langle m_1 m_2|$ to $|m_1 + 1, m_2 - 1\rangle$ or to $|m_1 - 1, m_2 + 1\rangle$, a simultaneous flip of both spins happens. The term C contains a raising operator corresponding to each particle, connecting levels separated by ΔM=+1, while the term D contains lowering operators that connects levels separated by ΔM=−1 (single quantum transitions). The terms E contains two raising operators one for each spin, connecting levels separated by ΔM=+2, conversely F connects and ΔM=−2 ("forbidden" double quantum transitions). C, D, E, F terms can not be neglected for low external magnetic fields.

2.4.1 Zero field interaction

In the section 2.2.1 the zero field splitting (ZFS) of the NV$^-$ center (spin S=1) was already mentioned to be caused by the spin-spin dipolar interaction of the unpaired electrons and , in second order, by spin-orbit interactions [26]

$$H_{ZFS} = \bar{S}^T \bar{\bar{D}} \bar{S} \tag{2.18}$$

It is composed by the following components:

$$\bar{\bar{D}} = \begin{pmatrix} D_{xx} & D_{xy} & D_{xz} \\ D_{yx} & D_{yy} & D_{yz} \\ D_{zx} & D_{zy} & D_{zz} \end{pmatrix} \qquad\qquad \mathbf{S} = (S_x, S_y, S_z)$$

The tensor $\bar{\bar{D}}$ is the *Zero field splitting tensor*, the Hamiltonian can be rewritten in a simplified form considering it to be in a coordinate system where $\bar{\bar{D}}$ is diagonal.

$$H_{ZFS} = D\left(\hat{S}_z^2 - \frac{1}{3}S(S+1)\right) - E(S_x^2 - S_y^2) \tag{2.19}$$

$$D = \frac{3}{2}D_{zz} \qquad\qquad\qquad E = D_{xx} - D_{yy} \tag{2.20}$$

11

2.4.2 Hyperfine interaction between an electron and a nuclear spin

Hyperfine interaction is the name given to the interaction between an electron spin S and a nuclear spin I.

$$H_{HF} = \bar{S}.\bar{\bar{A}}.\bar{I} \tag{2.21}$$

The description of the magnetic coupling between an electron and a nearby nuclei requires to consider the fact that the electron is distributed over a single occupied molecular orbit (SOMO). Two types of orbitals are important to distinguish, the s-orbitals an the other orbitals p, d, f. In the s-orbitals, the probability of the electron to be at the nucleus is finite, leading to a singularity of the dipole-dipole interaction, this contribution to the hyperfine coupling is isotropic and called *Fermi contact interaction*. [27]

In the case of the non-s orbitals (p, d, f) the dipole-dipole interaction averaged result in an anisotropic contribution to the hyperfine coupling.

Both contributions compose the hyperfine Hamiltonian, these can be written separately.

$$H_{HF} = a_{iso}\bar{S}.\bar{I} + \bar{S}.\bar{\bar{A}}_{dd}.\bar{I} \tag{2.22}$$

In the case on which the nuclear spins are weakly coupled to the electron spin (nuclei far from the electron), the Hyperfine interactions is reduced to:

$$H_{ne} = \frac{\mu_0 \gamma_n \gamma_e \hbar^2}{4\pi r^3}(\bar{S}.\bar{I} - 3(\bar{S}.\hat{r})(\bar{I}.\hat{r})) \tag{2.23}$$

2.5 NMR basics

The nuclear magnetic resonance (NMR) experiments can be described in general terms as a group of techniques to investigate the properties of nuclei ensembles by studying the recorded transitions between nuclear spin energy levels, the samples are located in a magnetic field $\mathbf{B}_0$ and subjected to radiofrequency (RF) radiation. As explained in section 2.3, the energy separation is determined primarily by the Zeeman interaction, which varies linearly with the magnitude of $\mathbf{B}_0$, nevertheless, the local environment of the nuclei has some observable effects due to coupling with nearby particles. The NMR method leans in the property of particles spin, as we already grasped in 2.3 section, a particle with a spin angular momentum $\bar{I}$ has an angular magnetic moment $\bar{\mu}_I$ associated with it. Specifically, in the case of the nucleus and electron

$$\bar{\mu}_I = \hbar\gamma_n\bar{I} \tag{2.24}$$

Accordingly, the nuclear Zeeman Hamiltonian $H_{Z,I}$ that represents the interaction between the static magnetic field barB$_0$ and the magnetic moment intrinsic to the nuclei barB$_0$.

$$H_{Z,I} = -\hbar\gamma_n\bar{I}.\bar{B}_0 \tag{2.25}$$

For the case of a particle with spin I=1/2, consider the conventional orientation established for the static magnetic field $\bar{B}_0$ in the Z direction, that being the case, the only component from $\bar{I}$ to be considered is I_Z with eigenstates denoted by $|\uparrow\rangle$ and $\langle\downarrow|$ and respective eigenvalues $m_I = +1/2$ and $m_I = -1/2$ [28]
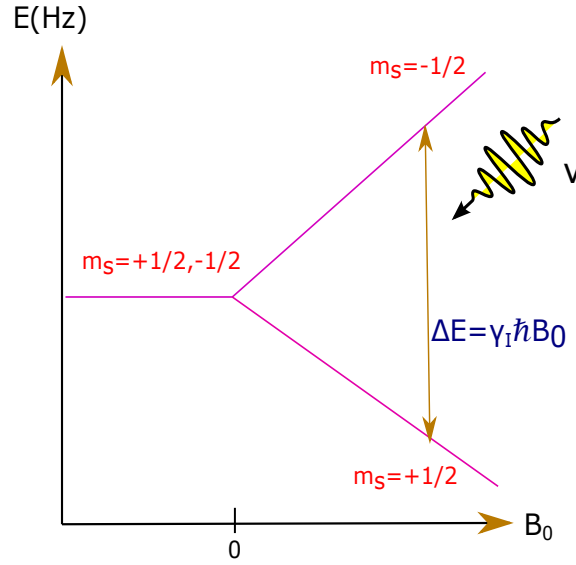
Figure 2.9: Zeeman splitting for a nuclei S = 1/2 system in the presence of an external magnetic field $\bar{B}_0$, a transition between the two states can take place if radiation with a given frequency ν that matches the resonance condition is applied

On that account, the energy eigenvalues that correspond to the Zeeman Hamiltonian are condensed in the following expression:

$$E_{m_I} = \gamma_I m_I \hbar B_0 \tag{2.26}$$

As we can see in the figure, the energy difference between the two states that arise because of the presence of the magnetic field:

$$\Delta E = \gamma_I \hbar B_0 \tag{2.27}$$

Here we can introduce a key concept also in NMR : The *Larmor frequency* $\omega_0 = \gamma_I B_0$. Clearly, the energy gap between two states depend on ω_0. We can rewrite this explicit dependence

$$\Delta E = \hbar \omega_0 \tag{2.28}$$

As explained in the introduction, a NMR sample is not just one spin, but an ensemble of N spins, each of this spins contribute with the expectation value of I_z, these values are summed and averaged in order to define what is called *Magnetization*. [29]

$$\mathbf{M} = \gamma \hbar N \overline{\langle I_z \rangle} \tag{2.29}$$

We can define the populations of each of the two levels to be the number of spins polarized parallel to the magnetic field B_0 are denoted $N_\uparrow$ and those polarized in the antiparallel fashion are denoted $N_\downarrow$. Under the condition of thermal equilibrium, we can describe the populations for each level using the Boltzmann's distribution.

$$\frac{N_\uparrow}{N} = \frac{\exp\left(\frac{E_\uparrow}{k_B T}\right)}{\exp\left(\frac{E_\uparrow}{k_B T}\right) + \exp\left(\frac{E_\downarrow}{k_B T}\right)} \tag{2.30}$$

$$\frac{N_\downarrow}{N} = \frac{\exp\left(\frac{E_\downarrow}{k_B T}\right)}{\exp\left(\frac{E_\uparrow}{k_B T}\right) + \exp\left(\frac{E_\downarrow}{k_B T}\right)} \tag{2.31}$$
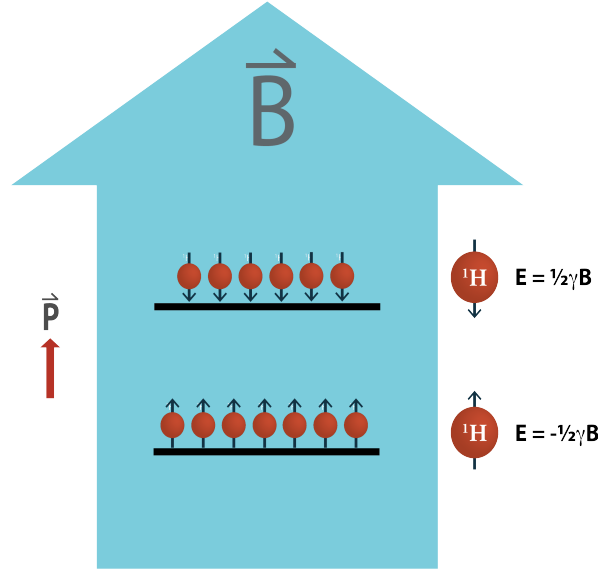

Figure 2.10: Polarization sketch in a two energy level system [30]

It is appropriate to introduce the concept of polarization:

$$P = \frac{N_\uparrow - N_\downarrow}{N_\uparrow + N_\downarrow} \tag{2.32}$$

In the special case of thermal equilibrium, we can combine (2.28) , (2.33) and (2.32) to obtain

$$P = \tanh\left(\frac{E_\uparrow - E_\downarrow}{k_B T}\right) = \tanh\left(\frac{\hbar\omega_0}{k_B T}\right) \tag{2.33}$$

To build up high polarization in traditional NMR, high magnetic fields of order or tens Tesla are used. For instance, suppose we have at room temperature 300 K the sample of ^{13}C spins in our NMR spectrometer at a field $B_0 = 7$ T [8], in order to have in average one spin aligned to the magnetic field we would need 160000 spins from which most of them will "cancel" one another . This would lead to a polarization value of $P \approx 0.0006$, this insignificant percentage is interpreted as the energy levels to be equally populated. Therefore, the signal intensity in the NMR experiment is also small.

It is possible to notably enhance the signal intensity through an *Hyperpolarization* technique, this is done by creating population differences between nuclear spin state. Accordingly, an ensemble that is prepared so that all the nuclear spins are occupying a certain state is called *Hyperpolarized state*. Two hyperpolarization techniques are revisted in this master thesis, these are described in chapter 5.

Signal detection in NMR

The signal detected in a NMR experiment is the precession of the net magnetization vector **M** from nuclear spins. As showed in the diagram below, there is a set of coils which are aligned in the X − Y plane. This set of coils plays the role of detection coils and also generates the radio frequency (RF) fields need it to be able to detect the magnetization vector **M**. The goal of the RF fields is to rotate the magnetization **M** to the X direction in order to detect it. Since it is not possible to change suddenly the magnetic field in this manner, the concept of resonance is used by applying a very small oscillating magnetic field in near or at resonance with the *Larmor precession frequency* in order to make the magnetization **M** to move towards the transverse X − Y plane. The effect of this oscillating field applied is better understood under a change of reference frame, from the *laboratory frame* to the so called *rotating frame*.
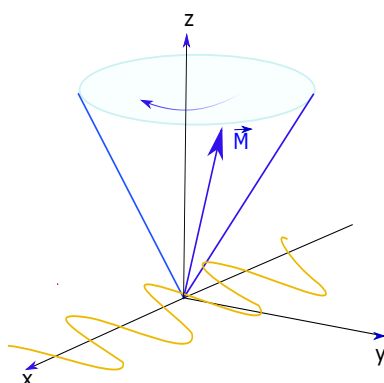

Figure 2.11: Magnetization precessing inducing current in a detection coil around the x-axis . The amplification of this current is the free induction decay signal (FID)

Starting with reinterpret the RF field as a sum of B_1^+ and B_1^- two counter rotating fields with the same magnitude B_1, we can rewrite the RF field as $B(t) = 2B_1 \cos \omega_0 t$ [29].
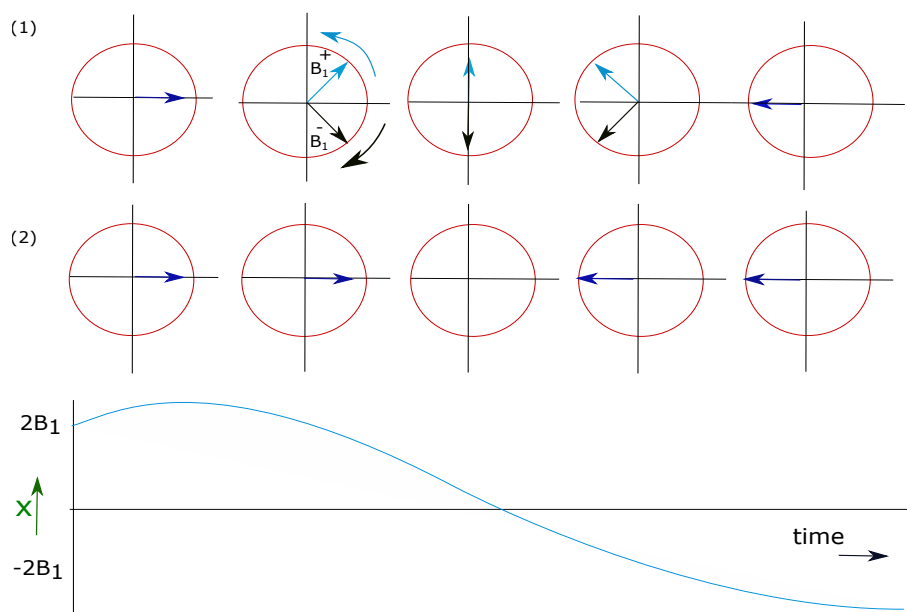

Figure 2.12: In (1) two fields rotating in opposite directions B_1^+ and B_1^+ which add to give an oscillating field along the x-axis (2)

15

The magnetization from the sample will be precessing around the z direction with a positive gyromagnetic ratio, which means that the component B_1^+ can be discarded since it will not interact with the magnetization vector. Nevertheless, the component remaining is still time dependent and B_0 is a static field, in order to being able to establish a relation between this two fields it becomes a necessity to change to a rotating frame where B_1 is also static. The rotating frame rotates about the Z axis with a frequency $(-\omega_{RF})$ and in the same direction as B_1^-. Consequently, the Larmor precession frequency of the magnetization vector ω_0 in the rotating frame is $\Omega = \omega_0 + \omega_{RF}$ and its respective magnetic field associated ΔB is called *reduced magnetic field*

$$\Delta B = -\frac{\Omega}{\gamma} \tag{2.34}$$

As illustrated in the figure above, ΔB and B_1 originate the called *effective magnetic field* B_{eff}

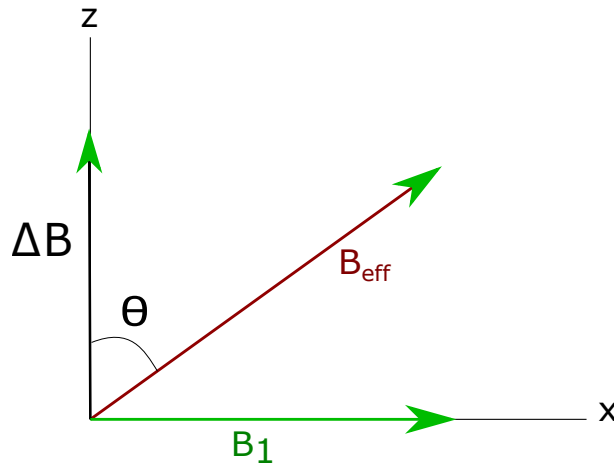$$B_{\text{eff}} = \sqrt{B_1^2 + (\Delta B)^2} \tag{2.35}$$

Figure 2.13: In the rotating frame the magnetization precess around the B_{eff}

When $\Omega \to 0$ approaches the resonance condition , which means that the equilibrium magnetization vector rotates far from the Z-axis, at this point B_1 become relevant since $\Delta B \to 0$

In terms of frequency the fields in the figure can be expressed as:

$$\omega_1 = |\gamma| B_1 \tag{2.36}$$

$$\omega_{\text{eff}} = \sqrt{\omega_1^2 + \Omega^2} \tag{2.37}$$

$$\omega_{\text{eff}} = |\gamma| B_{\text{eff}} \tag{2.38}$$

2.5.1 On-resonance pulse

As already mentioned in the previous subsection, the resonant condition is crucial to detect the magnetization **M**. When the transmitter has a frequency is on resonance to the Larmor frequency, this oscillating field is called an *on-resonance pulse*. From 2.35 it shows that this resonant condition being met means that $\Omega=0$, therefore the effective field angle tilt $\theta=\pi/2$ (90°).

Through the precession frequency ω_1, the duration of the applied RF pulse t_p is related to the angle that the magnetization is rotated in the following way:

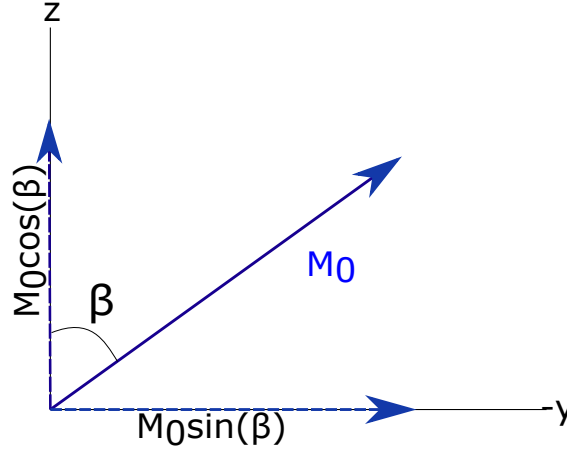$$\beta = \omega_1 t_p \tag{2.39}$$

Figure 2.14: Components of the magnetization vector after applied an on-resonance pulse with a *flip-angle β*

In general the components of the magnetization after applying a pulse of certain angle are as showed in the figure 2.14 are:

$$M_z = M_0 \cos(\beta)$$
$$M_y = -M_0 \sin(\beta)$$

The two most common pulses are the $\pi/2$-pulse that inverts the magnetization from Z-axis to $-$Y-axis. And the π-pulse also known as *inversion pulse* that brings the magnetization from Z-axis to -Z-axis.

In NMR spectroscopy the resulting spectrum have several Larmor frequencies. Accordingly, the RF field are made large enough to make the effective field to lay on the x-axis, therefore the magnetization behaves as if the pulse is on resonance.

Bloch-Maxwell equations

The magnetization vector **M** evolves in time according to the following motion law [31]:

$$\frac{d\mathbf{M}}{dt} = \gamma[\mathbf{M} \times \mathbf{B}] \tag{2.40}$$

In the rotating frame of reference, the magnetic field **B** is the effective magnetic field

$$B_x = B_1 \cos(\omega_0 t) \qquad\qquad B_y = -B_1 \sin(\omega_0 t) \qquad\qquad B_z = B_0 \tag{2.41}$$

Nevertheless, the equation (2.40) does not accurate describe the magnetization vector evolution, since it does not consider the fact that the last returns to its equilibrium state $\mathbf{M} = M_0\hat{z}$, this process is known as *Relaxation*. In the rotating frame the relaxation of **B** components can be described by the following expressions.

$$\frac{dM_x}{dt} = -\frac{M_x}{T_2} \qquad\qquad \frac{dM_y}{dt} = -\frac{M_x}{T_2} \qquad\qquad \frac{dM_z}{dt} = -\frac{(M_z - M_0)}{T_1} \qquad (2.42)$$

Adding these set of equations to (2.40) we obtain the differential equations set for the three components of the magnetization vector $\mathbf{M}$

$$
\begin{aligned}
\frac{dM_x}{dt} &= \gamma(\mathbf{M} \times \mathbf{B})_x - \frac{M_x}{T_2} \\
\frac{dM_y}{dt} &= \gamma(\mathbf{M} \times \mathbf{B})_y - \frac{M_y}{T_2} \\
\frac{dM_z}{dt} &= \frac{M_0 - M_z}{T_1} + \gamma(\mathbf{M} \times \mathbf{B})_z
\end{aligned}
\qquad (2.43)
$$

The solutions for the set of Bloch equations above are:

$$
\begin{aligned}
M_x(t) &= M_x(0)\cos(\omega_0 t)\exp\left(-\frac{t}{T_2}\right) \\
M_y(t) &= M_y(0)\sin(\omega_0 t)\exp\left(-\frac{t}{T_2}\right) \\
M_z(t) &= M_z(0)\exp\left(-\frac{t}{T_1}\right) + M_0\left(1 - \exp\left(-\frac{t}{T_1}\right)\right)
\end{aligned}
\qquad (2.44)
$$

From the asymptotic limit ($t \to \infty$) we find the steady solution:

$$M_z(\infty) = M_0 \qquad\qquad M_x(\infty) = M_y(\infty) = 0 \qquad (2.45)$$

In case of the transversal component ($M_x(t)$ and $M_y(t)$) their time dependent solution have a sinusoidal component that represents the precessional motion, while the exponential factor represents the transverse relaxation effect, the transversal component rotates until it vanishes, this process is called *spin-spin relaxation* and is characterized by the constant T_2 . On the other hand the longitudinal component $M_z(t)$ relaxes to its equilibrium value M_0, this process is named *spin-lattice relaxation* or *longitudinal relaxation* and its characterized by the constant T_1

2.6 NMR spectroscopy system

The center of the spectrometer is the superconducting magnets that produce an homogeneous magnetic field B_0, the magnetic field is generated by a special coil of wire made with a combination of copper,niobium and tin through which the current that generates B_0 passes, this coil has to be at a extremely low temperature ($< 6K$), to maintain the superconducting property of the coil this last is inserted in a liquid helium bath. A "heat shield" at $77K$ at contact with a bath of liquid nitrogen helps to reduce the amount of helium that boils off due to heat flow from the environment. To achieve the levels of field homogeneity necessary to satisfy the NMR experiment demands, the sample is surrounded by a set of *shim coils*, the current that flows through this set of coils is adjusted to cancel out the inhomogeneities of B_0. In addition of inhomogeneities, drifts from the magnetic field B_0 is a factor to control, to compensate the drifts a feedback system called *field-frequency*
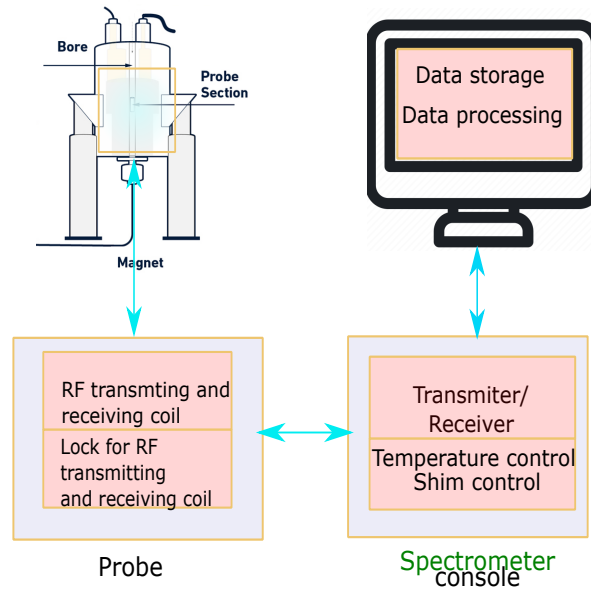
Figure 2.15: Simplified diagram of a nuclear magnetic resonance spectrometer

lock is implemented to control the stability of B_0 [29]. The piece that connects the outside environment with the superconducting magnets is a vertical tube that goes through the magnet, it is called the *bore tube* and it is also where a cylindrical metal tube, which carries the sample and bring it to the center of the superconducting magnet, is located, the last is called *the probe* and on top of it there are the *RF-coils* which are responsible for the excitation (*transmitter*) of the nuclear spins on the sample and at the same time for the detection of the NMR signal (*receiver*), a circuit constituted by the probe, a capacitor and the [32] RF-coils control the "tunning probe" process which consists on adjusting the capacitor until the circuit is resonant at the Larmor frequency (ω_L), this process goes in hand with "matching the probe" that is performed for optimizing the power transfer between the probe and the RF-coils.

2.7 NMR signal acquisition and detection

[33] [29]

The data acquisition starts with converting the NMR signal voltage received to a binary number so it can be digitally stored, this is done with an apparatus called *Analogue to digital converter* (ADC) at a certain sample interval Δ, also called *dwell interval* determined by the relation $\Delta = 1/2f_{max}$, where f_{max} is the *Nyquist frequency* that establish which should be the sample interval to be able to represent frequencies up to this f_{max} frequency value

As mentioned in the section above, the *shim coils* detect the magnetization that constitute the FID (free induction decay), this signal is mixed with the Spectrometer reference frequency ω_{rf}, consequently the offset frequencies Ω are passed to the ADC since ω_{rf} has a defined phase and the detection takes place on the rotating frame fixed axis.

The FID signal is the sum of a series of periodic waves with different amplitude, phase and frequencies. This is detected by the detection channels along the axis X and Y, the general form of the detected signal is the following
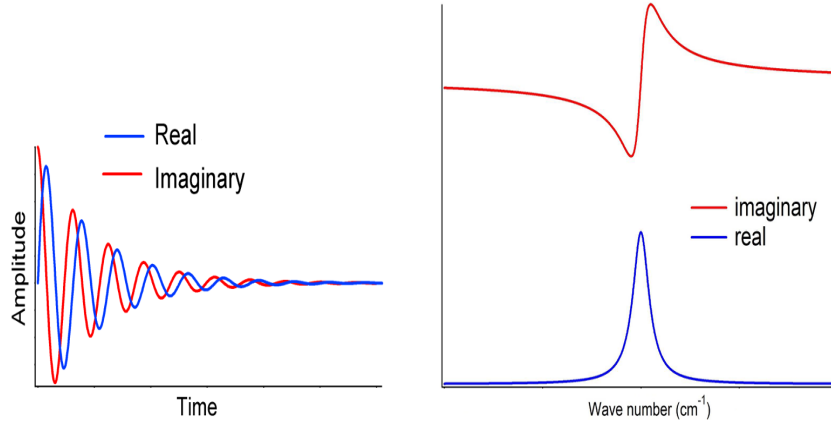
Figure 2.16: Components of the free induction decay : Real and imaginary

$$S(t) = \cos(\Omega t)\exp(-t/T_2) + i\sin(\Omega t)\exp(-t/T_2) \qquad\qquad t \geq 0$$
$$S(t) = 0 \qquad\qquad t \leq 0$$

Applying the Fourier transform to the signal to convert it onto the frequency domain as indicated by the expression

$$S(\omega) = \int_{-\infty}^{+\infty} S(t)\exp(-i\omega t)\,dt \tag{2.46}$$

The spectrum contains a real and an imaginary part denoted as $R(\Delta\omega)$ and $I(\Delta\omega)$, respectively, while the frequency parameter is centered around the resonance frequency $\Omega : \omega = \omega - \Omega$.

The real part is the one that corresponds to the absorption and the imaginary correspond to the dispersion part, both are Lorentzian curves and just the real part is of interest.

$$S(\omega) = R(\Delta\omega) - iI(\Delta\omega) \tag{2.47}$$

Nevertheless, in practice the dispersion and absorption parts are not totally differentiated since generally the magnetization acquires phases due to the reason that the $\pi/2$-pulse applied does not align the magnetization with the detection real channel and also because of the delay between the end of $\pi/2$-pulse and the start point of the data acquisition step.

To obtain the absorption part of the spectrum phase correction is applied. There are two types of phase correction, the zero-order phase correction that helps to differentiate the absorption part of the spectrum from the dispersion part, and the first-order phase correction that is required to correct the effect of the delay between pulse and acquisition when these delays are of the same order of the frequency offset Ω. The phased spectrum is expressed as

$$S_p = S(\omega)\exp(-i(\phi_0 + \phi_1\omega\Delta t)) \tag{2.48}$$

2.7.1 EPR Basics

[27][34]

The electron paramagnetic resonance (EPR) spectroscopy, also known as electron spin resonance (ESR) is a method for studying materials that have unpaired electrons. This section briefly explains the most relevant features of this technique since some samples used in this master thesis were characterized using this spectroscopy technique.

The principles in which the EPR spectroscopy are basically the same as the principles in which the NMR spectroscopy are based. The differences result from the fact that the gyromagnetic ratio of the electron γ_e is much larger than the one of the nuclei γ_I due to the fact that the nuclear particles have masses ($1836 \times m_e$), for this reason the nuclei spin at a much slower frequency, therefore the Boltzmann polarization 2.33 is much larger at the same magnetic static field . The photons detected have a much higher frequency (in order of GHz) and the relaxation times are approximately 6500 shorter, this features make EPR much more sensitive and allows a much faster repetition of experiments than NMR.

This can be seen by the electron Zeeman effect for an electron spin with $S = 1/2$ two level system, the nuclear Zeeman effect for a two level system is described section 2.5. Both are basically the same, but with the difference in energy scales just mentioned. The electron Zeeman effect will be described with the nomenclature usually employed in the EPR community.

Considering that, in the absence of an external magnetic field, the magnetic moment of the electron spin is randomly oriented and the two energy levels are degenerate. The presence the presence of an external magnetic field $\bar{B}_0$ leads to the splitting of the energy levels. The following Hamiltonian expressed in frequency units describes the system

$$H_{ZEI} = \frac{g_e \beta_e}{h} \bar{S} . \bar{B}_0 \tag{2.49}$$

Here g_e is the free electron Landé factor $g_e = 2.0023$, the constant $\beta_e = \frac{eh}{4\pi m_e}$ which after simplifying is $\beta_e = 9.274 \times 10^{-24}$ J/T. The energy eigenvalues obtained from the Hamiltonian H_{ZEI} are solely determined by the projection of the electron spin m_s which in this case can take the values (-1/2,1/2).

$$E(m_s) = \frac{g_e \beta_e}{h} B_0 m_s \tag{2.50}$$

Consequently, the energy difference between the two Zeeman states is given by :

$$\Delta E(m_s) = \frac{g_e \beta_e B_0}{h} \tag{2.51}$$

In this simple case of Zeeman interaction, the most basic EPR experiment could consist in irradiating the system with a field of varying frequency ν. The resonance condition met means that the frequency ν matches the energy difference ΔE, allowing transitions between the two states $m_s = \pm 1/2$
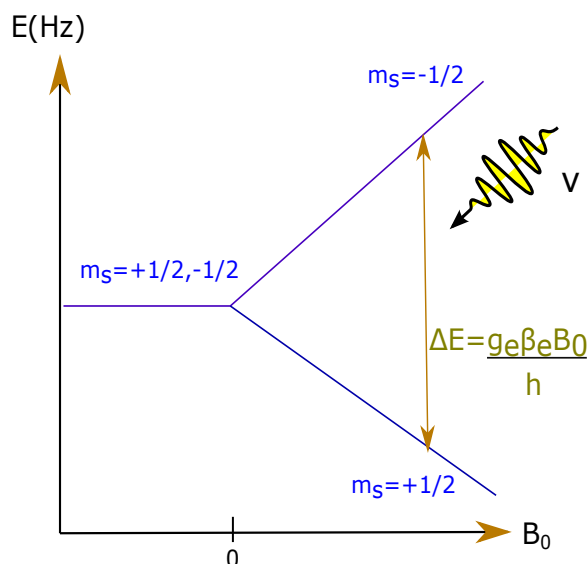
$$\Delta E = \nu \tag{2.52}$$

Figure 2.17: Zeeman splitting for an electron S = 1/2 system in the presence of an external magnetic field B_0, a transition between the two states can take place if radiation with a given frequency ν that matches the resonance condition is applied
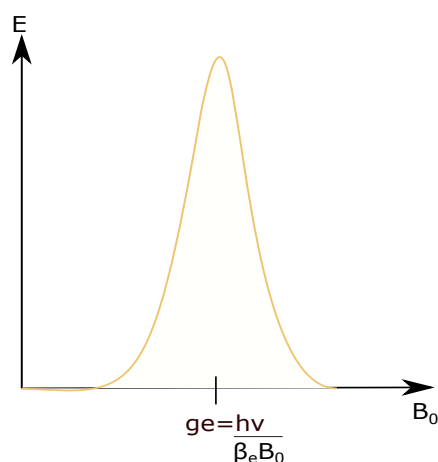

Figure 2.18: Absorption spectrum

CW EPR experiment

In contrast to the NMR spectroscopy where Fourier transform techniques covers the whole spectrum that can be excited simultaneously by pulses. On the contrary, the EPR spectra are much broader than the bandwidth of a microwave resonator, on account of this reason the continuous wave (CW) approach is a pulsed method used in most of EPR spectrometers. Unlike NMR spectroscopy, the frequency of the radiation (CW) is kept constant, and the magnetic field B_0 is varied, sweeping this last establishes the resonance condition for the spins to obtain the absorption spectrums.

It is shown in figure 2.19 a block diagram of an standard EPR spectrometer. The source of CW radiation is fixed frequency established, the microwave (CW) generated by the source passes through an attenuator in order to adjust its power, after that the CW passes through a circulator to the sample located in a resonant cavity placed

in the middle of an electromagnet, the microwave that returns from the sample undergo the same circulator and combined with reference microwave of adjustable power and phase before it detected by a microwave diode, the output signal is detected by a phase-sensitive detector (PSD) where is demodulated and amplified, finally the output signal is digitalized and processed by a computer software.
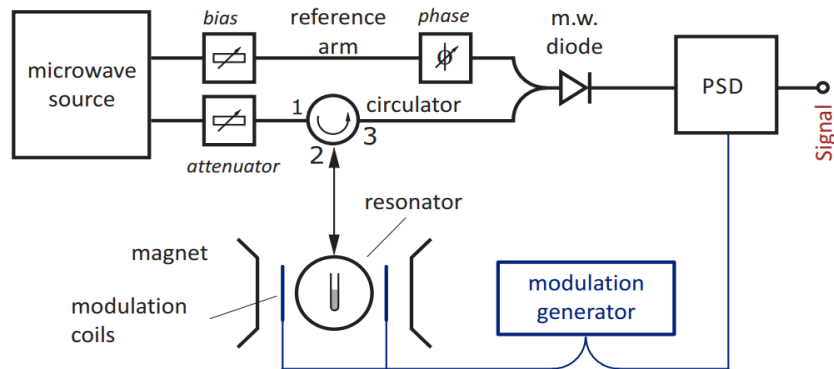

Figure 2.19: Scheme of a CW EPR spectrometer [27]

Chapter 3

Experimental methods

3.1 Experimental set up for hyperpolarization

In chapter 5 the two polarization transfer mechanisms were explained. In this section is described the experimental set up used to induce the polarization transfer of the electron spins of the NV centers to the ^{13}C nuclear spins through the cross polarization mechanism and through the Landau Zener mechanism.

The experimental set up is composed by the following parts :

- PC control
- NMR spectroscopy system
- Helmholtz-like coil pair I (Low field unit)
- Helmholtz-like coil pair II (generate sweep fields)
- Programmable power supply
- Power supply
- Shuttling system
- Cooling system
- Laser
- Laser diode
- Arduino controller board
- Red Pitaya board
- Analog controlled current regulator

Two very similar hyperpolarization setups were employed. The first hyperpolarization setup (set up 1) was designed to improve NMR signals of the ^{13}C nuclei by using a range of static magnetic fields in order to induce cross polarization. And the second setup improve NMR signals by employing time dependent magnetic fields superposed to static magnetic fields in order to induce Landau Zener transitions (set up 2)

The hyperpolarization set up 1 is managed by modules written in Python that control and automatize the experiment cycles. The sample probe is positioned in the shuttling system in the middle of the low field unit that generate a range of static magnetic fields in the z-direction, they values lay within a range of 48 mT and 54 mT. At the same time the sample is irradiated with a 532 nm laser with a power between 1 to 3 W is employed in order to polarize the NV centers to $m_s = 0$ state during an irradiation time that can take values between 10 to 30 s , the light undergoes a fiber optic and positioned in a hole located in the metal shield that covers the sample. The current and temperature stabilization of the laser is managed by a laser diode that is fed by the programmable power supply. This last is controlled by the Arduino board, along with the cooling system, is also controlled by the Python modules . After the laser pumping time, the sample is transferred by the shuttling system to the center of superconducting magnet (at $\approx$ 9T and proton Larmor frequency of 300 MHz) and with the help of the spectrometer part of the NMR setup the free induction decay signal is recorded.
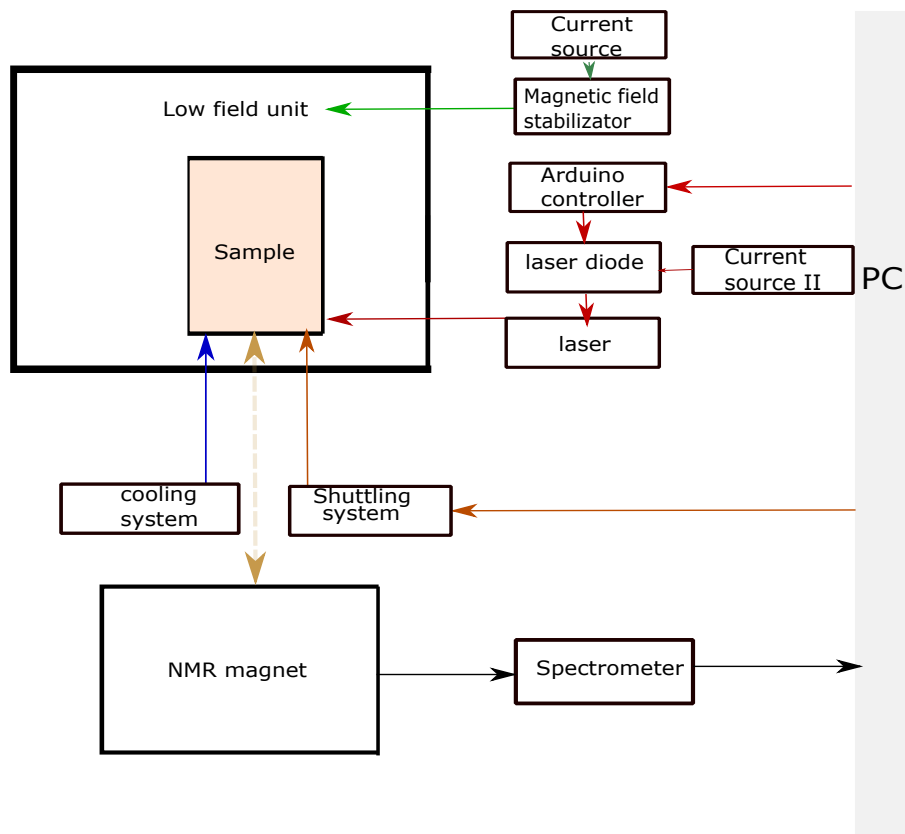

Figure 3.1: Diagram of the experimental set up 1

The hyperpolarization set up 2 is different from the hyperpolarization set up 1 in that a smaller set of Helmholtz-like coils set array is placed concentric to the low field unit as showed in the setup scheme. This additional piece generates the magnetic field sweeps superposed to the static magnetic fields. In order to generate the sweep fields, the Red Pitaya board sends a saw-tooth profile signal through SCPI commands, this signal is stabilized by an analog controlled current regulator fed by a power supply.
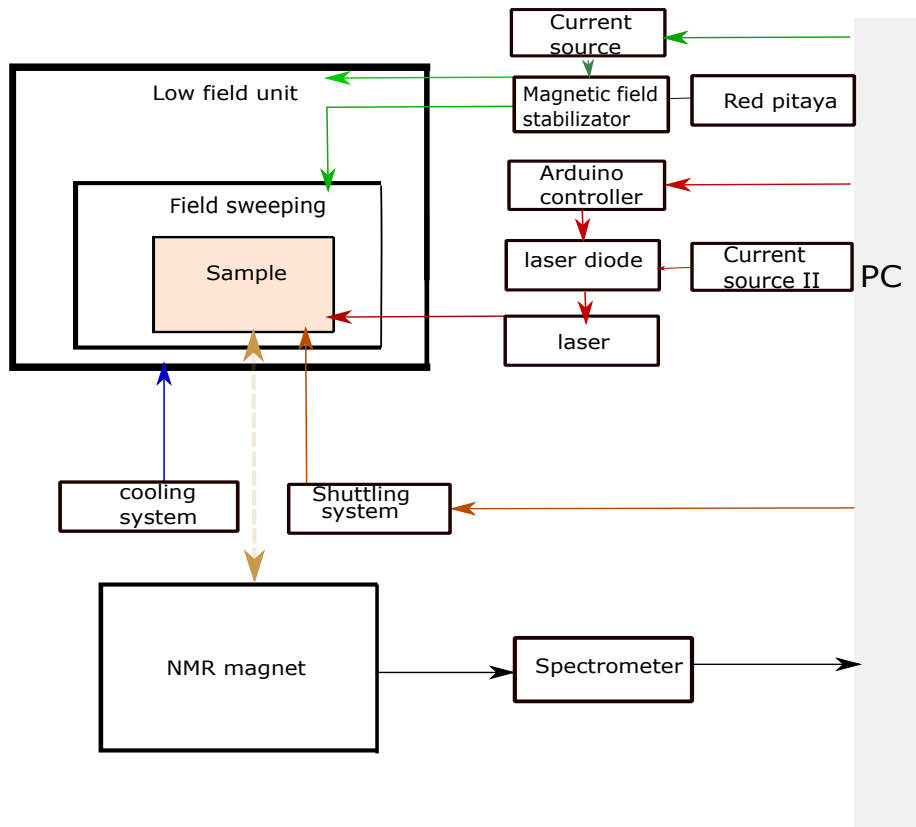
Figure 3.2: Diagram of the experimental set up 2

3.2   Diamond samples

The experiments performed were done with two types of samples : HPHT produced diamond micro particles (also called as diamond powder) and single milimeter-sized crystals.

3.2.1   Diamond micro particles

The concentration of substitutional nitrogen P1 and NV centers were obtained from cw EPR experiments . The measurements were performed at room temperature without illumination by Prof. Andreas Pöppl. The spin numbers for P1 and NV centers were determined for each of the five samples. No CW EPR measurements were taken for the sample id273, an approximation was estimated based on the P1 concentration of the sample id275 since both were exposed to similar fluence values.

sample id	fluence	NV$^-$ number of spins	P1 number of spins	C_{NV-}(ppm)	C_{P1}(ppm)
280	no irradiation	0	2.6×10^{17}	0	89.1 ± 17.8
277	1.2×10^{16}	0	1.9×10^{17}	0	53.9 ± 10.8
276	4.4×10^{17}	1.2×10^{15}	1.7×10^{17}	1.23 ± 0.37	68.8 ± 13.8
275	1.2×10^{18}	2×10^{15}	1.5×10^{17}	0.49 ± 0.123	58.0 ± 11.6
274	8.1×10^{17}	3.4×10^{15}	1.9×10^{17}	0.82 ± 0.25	61.7 ± 12.3
273	2.8×10^{18}	-	-	≈ 1	≈ 60

Table 3.1: NV$^-$ and P1 spin concentrations in diamond powder samples
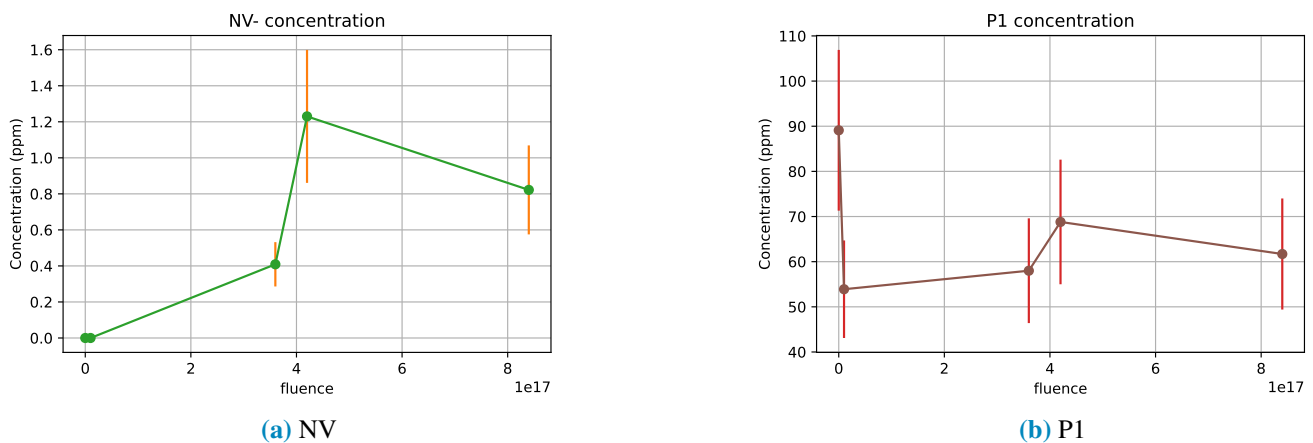

(a) NV

(b) P1

Figure 3.3: The plots relating the concentration of NV center and P1 vs electron fluence are showed below, considering the 30% error bar for NV center and the 20% error bar for P1 on the CW measurements.

3.2.2 Diamond single crystals

The sample id291 is composed by single milimeter-sized crystals randomly oriented respect to one another. The concentration characteristics were obtained from ([11]).

sample id	fluence	C_{NV-}(ppm)	C_{P1}(ppm)
291	2.8×10^{18}	3	30

3.3 Nutation experiment

To determine the correct π pulse duration was a required step for the experiments performed for this master thesis.

In this section, the *Nutation experiment* is briefly described in order to explain how the calibration of the π-pulse was performed.

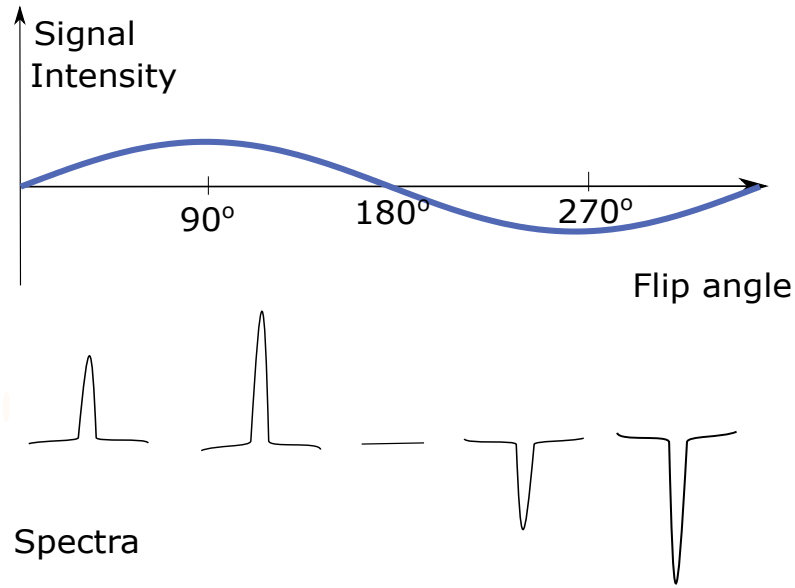**Figure 3.4:** Scheme of the pulse sequence used for the nutation experiment

Figure 3.5: Scheme of a pulse calibration experiment

As showed in the expression 2.39, the the nutation angle is proportional to the pulse length, which leads to the following expressions to determine the π-pulse length

$$\pi = \omega_1 \tau_{180} \tag{3.1}$$

$$\omega_1 = \frac{\pi}{\tau_{180}} \tag{3.2}$$

The nutation experiment is based on measuring the nutation of the magnetization vector $\mathbf{M}$ in a direct way. This is achieved by applying a pulse sequence of systematic increasing duration length (t_p in 3.4) consecutively [35]. One can observe how the spectra changes according to the change of the pulse flip angle.

The sequence of pulses make $\mathbf{M}$ to rotate on the $Z - Y$ plane, after a period of time a $\pi/2$-pulse is applied to record the FID signal. The FID signals are then processed in order to obtain the integral part of the spectra obtained through FFT. After that, the integral values are plotted with respect to the duration of the applied pulses from which the duration of the π-pulse is obtained through a fitting process.

3.4 Determination of π-pulse length

To determine the π-pulse length a nutation experiment was performed using 20 pulses of increasing duration. The FID set processing step was performed using `PyNMR`, this is an open source set of python modules developed to analyze NMR data. The integral values were plotted with respect to the duration of the 20 applied pulses and fitted with the function:

$$f(t) = A \sin\left(\frac{\pi t}{\tau_{180}}\right) \tag{3.3}$$

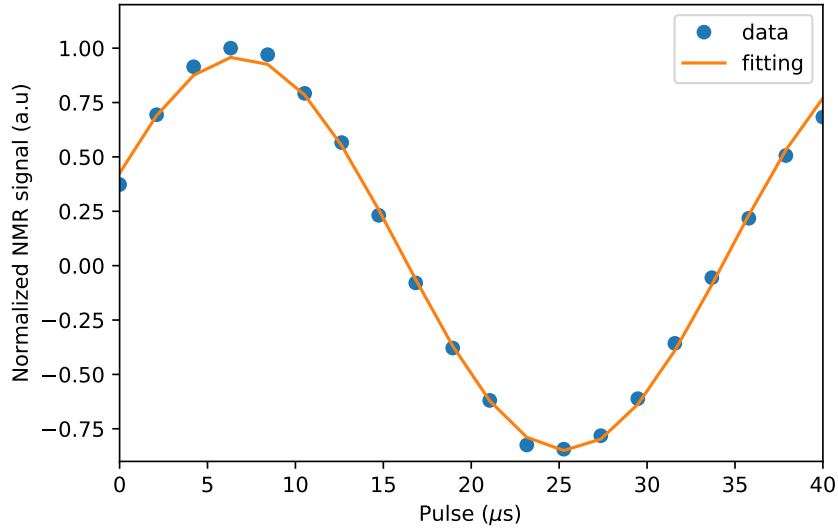Here τ_{180} represents the duration of the π-pulse, A is the amplitude.

Figure 3.6: Inversion recovery sequence

The result of the fitting leads to a a τ_{180}=18.5549 μs

3.5 Inversion recovery method to estimate T_1

In this master thesis the value of T_1 for ^{13}C in diamond powder was estimated from inversion recovery experiments. The pulse sequence of this technique consists in applying first a π pulse in order to invert the initial magnetization to $M_z(0) = -M_0$ and leave it to for a time interval τ, this transforms $M_z(t)$ (2.44) [29] to :

$$M_z(\tau) = M_0 \left(1 - 2\exp\left(-\frac{\tau}{T_1}\right)\right) \tag{3.4}$$

After τ a $\pi/2$ pulse is applied, the FID is recorded and processed, in our case with the PYNMR package. The experiment has to be repeated and the time between experiments t_r is determined by T_1 value of the species that is going to be measured in the following manner, since it is necessary to wait until the magnetization goes back to equilibrium. :

$$t_r = -T_1 \ln(1 - f) \tag{3.5}$$

Where f is the fraction of the equilibrium magnetization value to which the system returns. For a 99% of equilibrium magnetization value, the suitable time between experiments is $t_r = 5 \times T_1$.
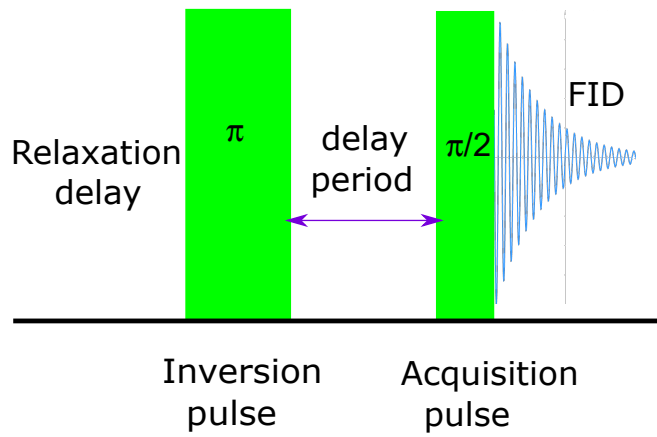
30

Figure 3.7: Inversion recovery sequence

3.6 T_1 measurements through the inversion recovery method

The T_1 values for ^{13}C have been obtained for the samples id280 and id291. The magnetization recovery curve were fitted with the expression (3.6) characterized by the γ parameter.

$$M_z(t) = M_z(0)(1 - 2\exp(-\gamma t/T_1)) \tag{3.6}$$

sample id	fluence	C_{NV-}(ppm)	C_{P1}(ppm)
291	2.8×10^{18}	3	30

Figure 3.8: id291

31

In the case of the diamond micro particles sample id280, four inversion recovery experiments were conducted

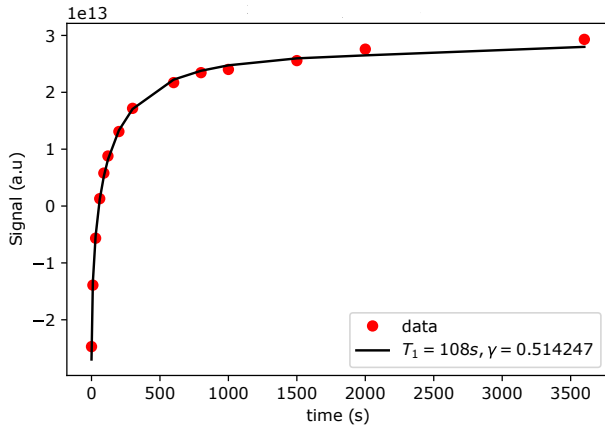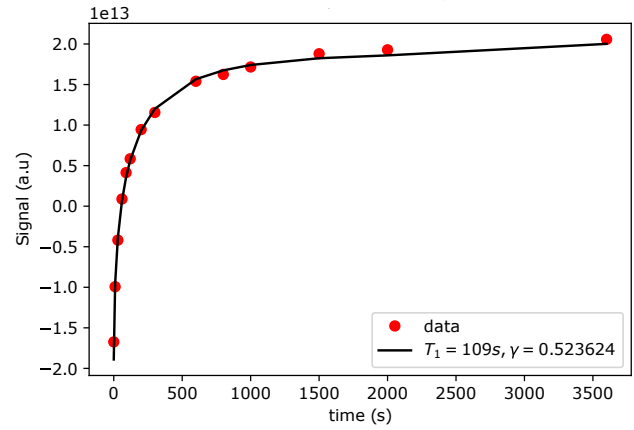| sample id	fluence	C_{NV-}(ppm)	C_{P1} (ppm)
280	no irradiation	0	89.1 ± 17.8

Figure 3.9: id280 (1)
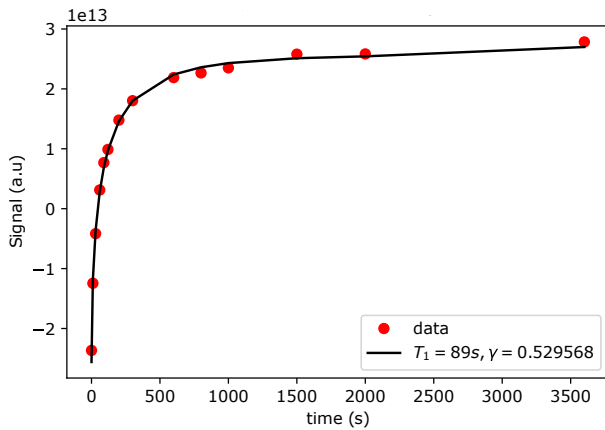

Figure 3.10: id280 (2)
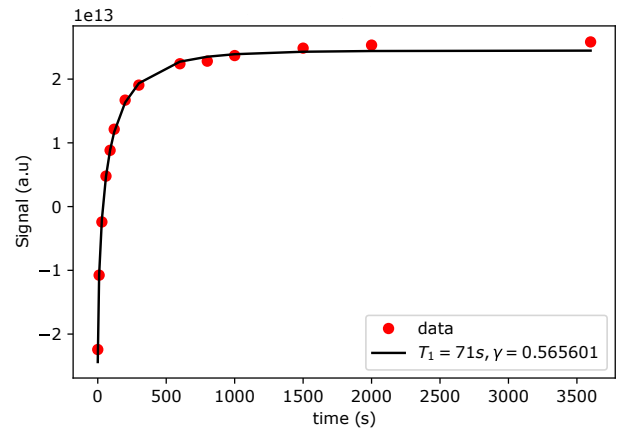

Figure 3.11: id280 (3)

Figure 3.12: id280 (4)

3.6.1 Calibration

Calibration of Helmholtz coil pairs

In this section it is showed the calibration plots of the low-field unit Helmholtz coils that generates the offset magnetic field and the second pair of Helmholtz coils that generate the sweeping field for the Landau-Zener transitions. The calibration procedure is the same for each set of coils.

The calibration set up consists in a Hall sensor supported by a micrometer set up that operates in the three directions, a current source connected to the set of coils.

The first step of the calibration process is performed by locating a Hall sensor between the coils at a certain fixed position in the Z symmetry axis and sweeping the Hall sensor on the X − Y plane , the power source is fixed at a certain current value I. A color map is plotted to find the position where the magnetic field B is the highest. With this position already found, the second step is to fix this position and vary the current up to I = 7A for the low field unit and up to I = 1A to the set of coils that generate the sweeping field. The relation between the magnetic field B and the current I is, as expected, linear.
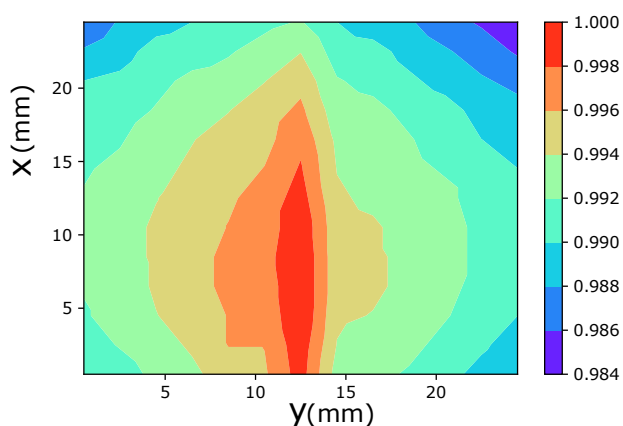

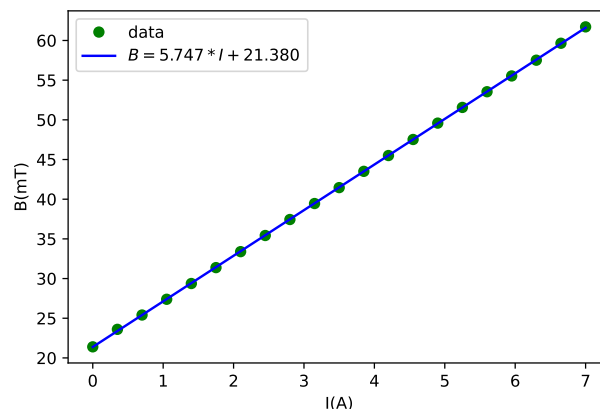Figure 3.13: Low field unit coils set colored map

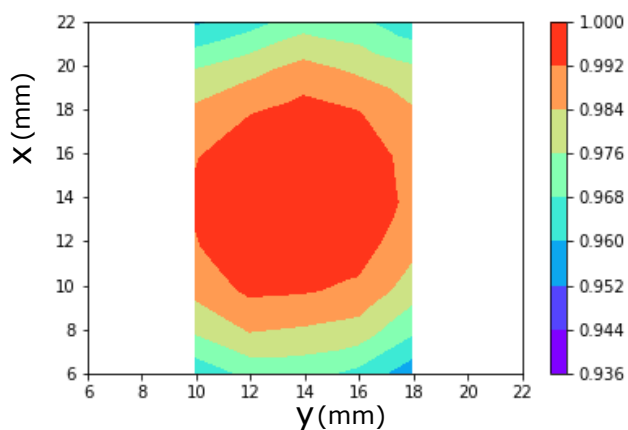Figure 3.14: B and I relation between the coils of the low field unit

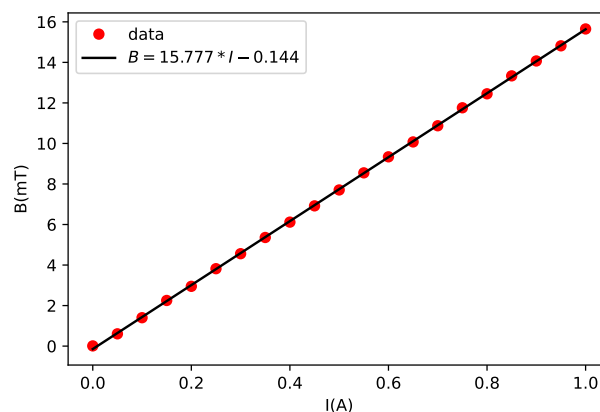Figure 3.15: Sweeping field coils set colored map

Figure 3.16: B and I relation between the coils of the sweeping field coils set

Red pitaya

Half-ramp (sawtooth) magnetic field sweeps are necessary to induce the Hyperpolarization of ^{13}C and study the spin dynamics due to Landau-Zener transitions. The Red Pitaya STEMlab 125-10 platform is used to estimate the time dependence of the magnetic field sweeps.

The Red Pitaya platform is basically a data acquisition system that generates and acquire digital and analog signals for general purposes. The principal benefit that offers is its affordability and capability to replace
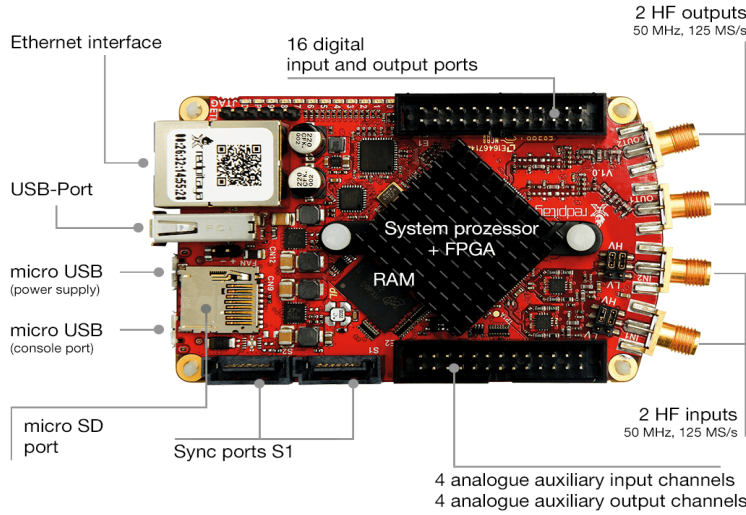
33

Figure 3.17: Red Pitaya board, position of components .

a variety of costly measurement and control instruments. Additionally, the board features two ADCs and two DACs which operate at 125 MS/s (10^6 samples per second). These are the interface between the SoC processing system and the Red Pitaya fast analog I/Os, and it is this unique combination of data-acquisition and processing components that gives the platform its versatility as an instrumentation tool. The main element of the Red Pitaya is a Xilinx Zync 7010 system-on-chip (SoC) device that contains a dual core ARM Cortex-A9 processor and a Field Programmable Gate Array (FPGA). The ARM processor is capable of running full operating systems, and the Red Pitaya uses this feature to run a custom Linux operating system which is loaded on an SD card [36]. The connection between the PC and the RP a is done with a LAN cable, at the same time the RP board must be connected to the network router so the DHCP server that runs in the router gives an IP address to the Red Pitaya board. To control the RP board the RP SCPI (Standard Commands for Programmable Instrumentation) were used, the commands to perform the generate the data and acquire it were written in a Python script.

Calibration of the magnetic field sweeps

The magnetic field sweeps are saw-tooth shaped and characterized by their slope, which will be called rate R_s from this point.
The sweep field rate R_s is defined by the sweep field range δB which plays an important role since it defines the beginning and end of the sweep field. With both δB and R_s, the duration of one magnetic sweep field is established t_{period}.

$$\delta B = B_F - B_I \tag{3.7}$$

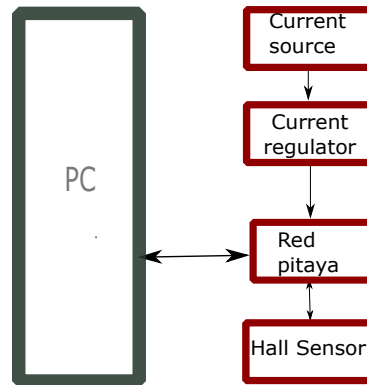$$t_{period} = \frac{\delta B}{R_s} \tag{3.8}$$

Figure 3.18: Diagram of the calibration set up of the magnetic field sweeps
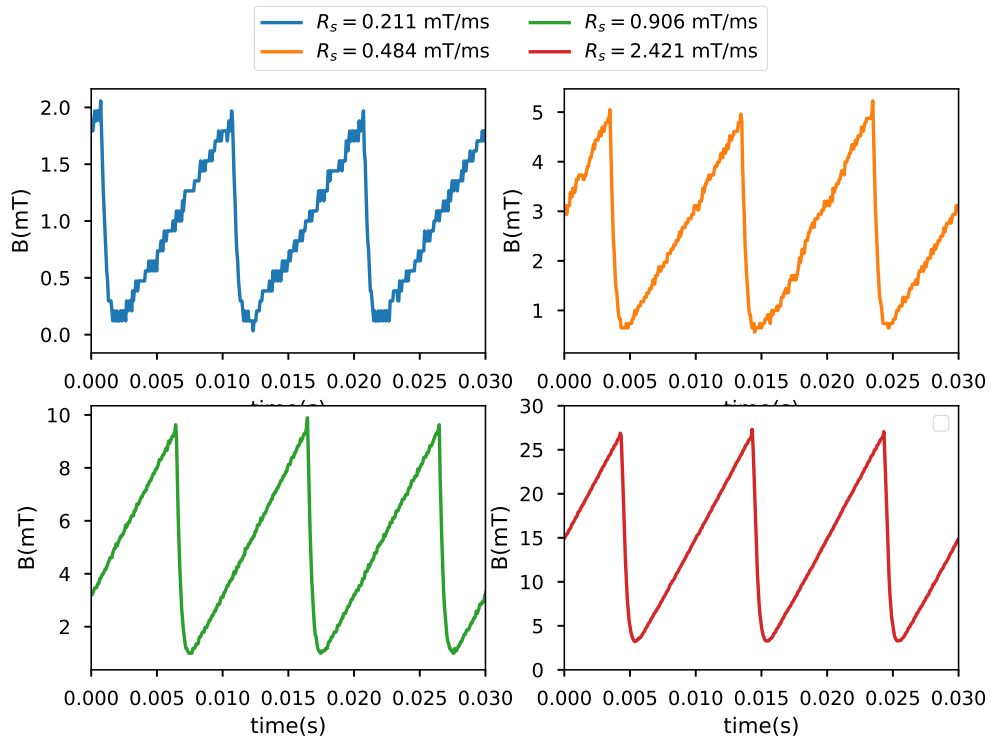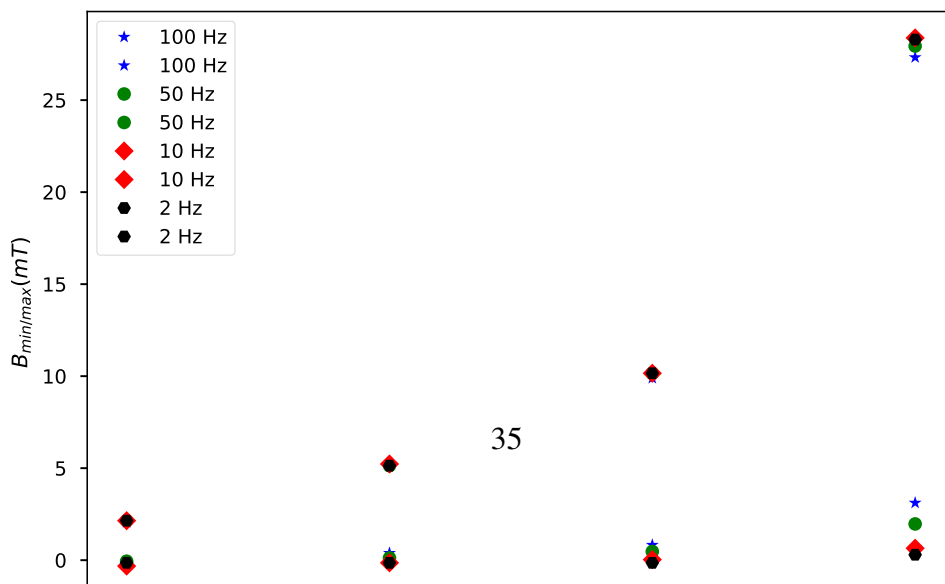

Figure 3.19: Sweep fields time dependence for a saw-tooth signal with frequency= 100 Hz. The legend shows the sweep fields for the respective field ranges in clockwise order $[2, 5, 10, 28 \cdot 292]$mT

35

The calibration of the magnetic field sweeps were performed with the set up showed on 3.18. The RP SCPI commands in a python script generates the saw-tooth signal and acquires the voltage read by the Hall sensor, in the middle of the diagram there is an analog controlled current regulator which is connected to a power source and also connected to the concentric Helmholtz array that receives the saw-tooth signal, between the two concentric coils the Hall sensor is positioned to read the output voltage.

With the help of (3.9), where s=31.25 V/T is the sensitivity parameter found in the Hall sensor's datasheet ([37]), V_{off} is the offset voltage and V_{out} is the output data read from the Hall sensor, the values of the magnetic field are obtained and the magnetic field dependence of time can be established.

$$B(T) = \frac{V_{out} - V_{off}}{s} \tag{3.9}$$

This procedure were repeated with different saw-tooth signal frequency values (e.g 2,10,50,100 Hz). In the figure (3.19) it is showed the dependence between the magnetic field sweeps and time obtained for a saw-tooth signal with 100 Hz sent through the RP to the small Helmholtz coil array. The figure (3.20) shows the maximum and minimum magnetic field values that compose the ranges [2, 5, 10, 28.292] mT of the magnetic field sweeps for different frequencies of the output saw-tooth signal.

Chapter 4

Experimental results

This chapter is divided three parts: The data post-processing and the other two sections : Induced Landau-Zener transitions experimental results and Cross polarization induced experimental results.

The first section is subdivided in four subsections that are defined in function of the parameter that is altered during the experiments . These parameters can be the magnetic field sweep rate R_s, the static magnetic field B, or the magnetic field sweep range δB. The samples mentioned in this subsection are described in the table 3.1

4.1 Data post-processing

All the analysis were performed using the `PyNMR` open source set of python modules to parse, process and analyze NMR data. This tool kit support Bruker Topspin data format among others.

In this section presents the post-processing procedure of the data obtained from the experiments performed. One of the data sets from the experiment array to induce Landau Zener transitions is used as an example.

The purpose of the post-processing is to obtain the integral of the real part of the spectrum which is the polarization signal of the ^{13}C nuclei in the sample. The sample used correspondent to this data set is the sample id275. This sample was irradiated by the laser beam with power of 3 W during 25 second per scan. The magnetic sweep field rates were varied 7 different values which lay within the range $R_s = [100, 1000]$ mT/s and δB= 6 mT . The magnetic field sweeps are superposed on a static magnetic field of B = 49 mT, the measurements for each magnetic sweep field rate is repeated 128 times (scans)

The first step of the data processing start with reading of the free induction decay signal (FID) recorded. In the set of FID signals a persistent initial noise is displayed, this noise had to be eliminated by applying a "left shift" which is the process of discarding the data points caused by the noise . The first miliseconds of the FID signals were discarded ,this is done by eliminating the first 20 data points. The left shift is applied in the same way to all data sets

The second step is to average the FID signals over the repetitions of a experiment with the same parameter values. In the data set used as example, the only parameter that varies is R_s, therefore the FID signals for each measurement with the same R_s value are averaged.

The third step consists in suppressing the data at the end of the FID signal which is mostly noise, this is done through a process called *Apodization* which consists on multiplying the FID by the called Apodization

function, in this case an exponential decay function were chosen for the Apodization step with a decaying factor determined by the *Line broadening* parameter which was fixed to be LB= 300 Hz.
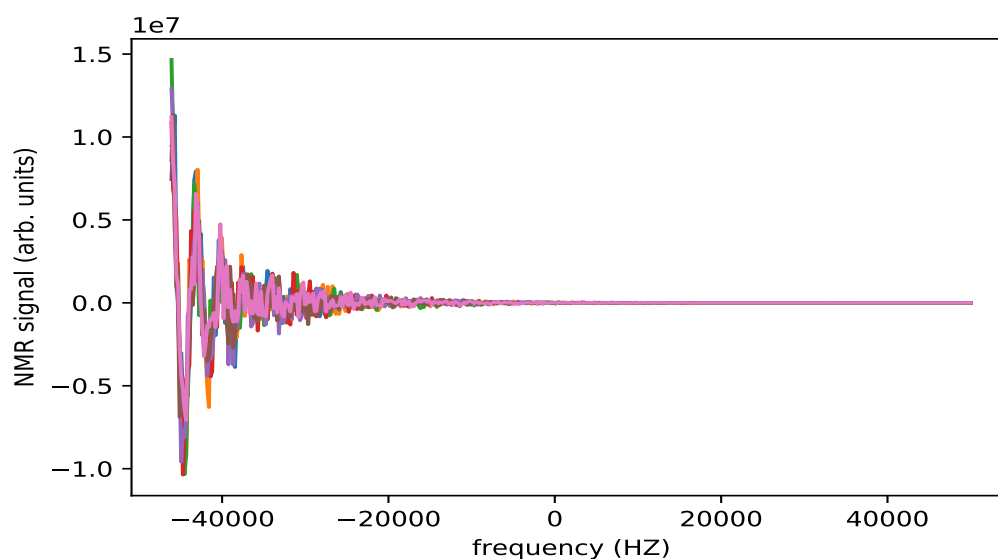

Figure 4.1: Sample id275: Set of averaged FID signals

The fourth step consists in applying a fast Fourier Transform (FFT) to the averaged FID signals to obtain the NMR spectra.

The fifth step consists in applying a zero order phase correction to each one of the averaged resulting FFT spectra set .These phase values are stored and the one that corresponds to the real part integral highest value was chosen to multiply all the averaged FFT.
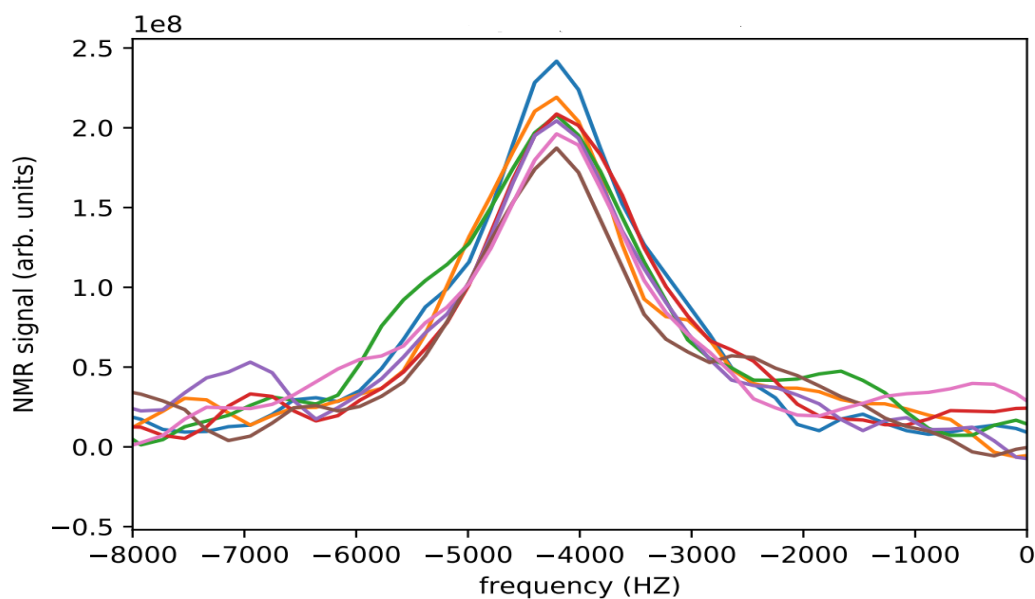

Figure 4.2: Sample id275: Set of averaged FFT NMR spectra

38

The last step is to calculate the area under each NMR spectra by integrating its real part . The values of the integrals are the measurement of the polarization, these are plotted with respect to R_s.
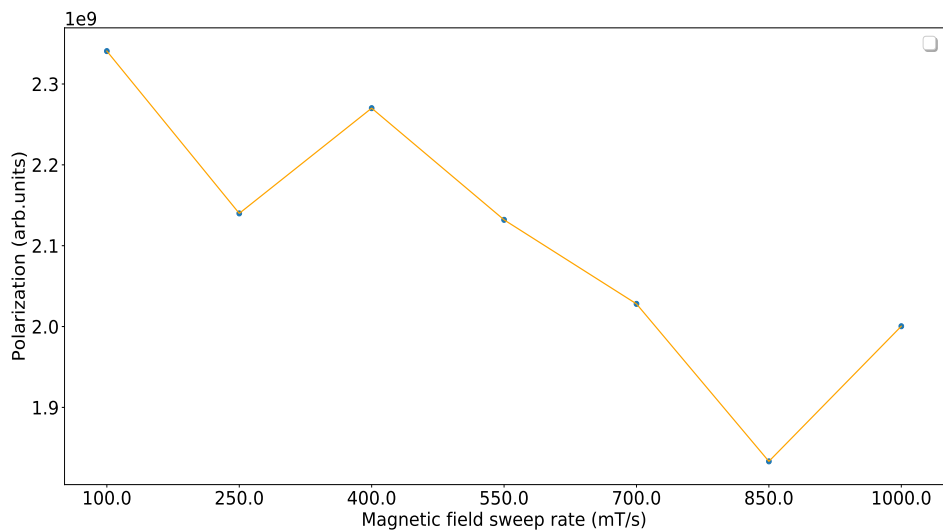

Figure 4.3: Sample id275: Real part of NMR spectra integral for the set of magnetic sweep field velocities R_s values indicated in the figure. This sample was irradiated by the laser beam with power of 3 W during 25 second per scan, the magnetic field sweeps are superposed on a static magnetic field of B = 49 mT, measurement for each magnetic sweep field rate is repeated 128 times

4.2   Induced Landau-Zener transitions experimental results
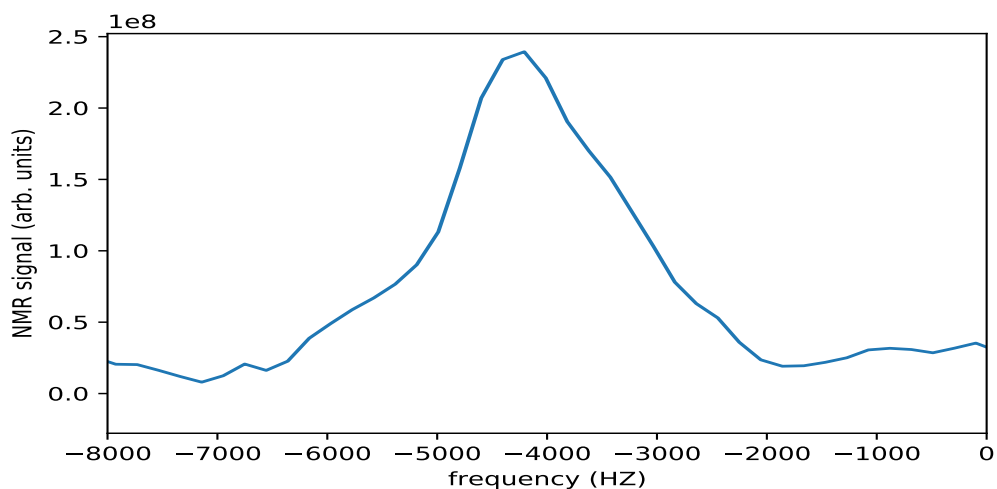

Figure 4.4: Sample id275: Real part of NMR spectra integral for a static magnetic field B = 49 mT, the laser irradiates the sample in three spatial directions with power of 3 W during 20 second per scan, at the same time the magnetic field sweeps are superposed on a static magnetic field with rate R_s = 800 mT/s and range δB = 5 mT , this measurement is performed 128 times
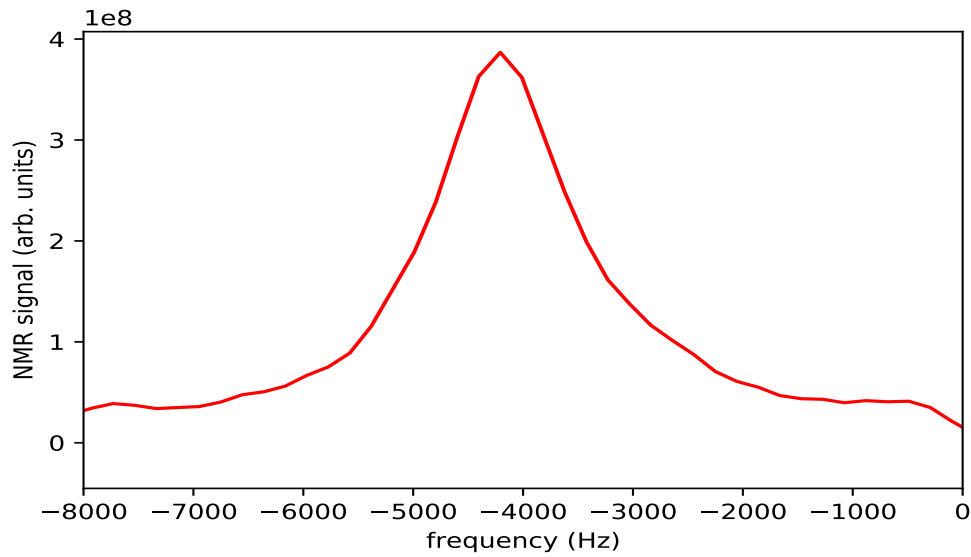
Figure 4.5: Sample id275: Real part of NMR spectra integral for a static magnetic field B = 49 mT, with the laser is off, at the same time the magnetic field sweeps are superposed on a static magnetic field with rate R_s = 800 mT/s and range δB = 5 mT , this measurement is the thermal signal measurement and it is also performed 128 times

Comparing the values of the integral spectra showed in figure 4.5 and figure 4.4, the integral value of the thermal signal is bigger than the integral value of the signal generated with the laser . Therefore, if transitions are induced it is done the thermal state, this extends to the results showed in 4.3 since the sample is the same.

4.2.1 Results by varying the magnetic field sweep rate R_s

In the data post processing section, one of the data sets originated by varying the magnetic field sweep rate R_s was used as an example. The set of parameters used for the sample id275 that give the results in figure 4.3 are also used for the sample id280. This results can be partially interpreted as the polarization obtaining its maximal value for a magnetic field sweep rates of R_s= 250 mT/s with a magnetic field range of δB= 6 mT. Then the polarization decays and increases again for the last two values of the magnetic field sweep rates, I can not suggest a reason for this. The parameter T_1 was calculated for this sample, leading to a T_1 of approximately 100 s, this measurement was done with a magnetic field of 7T. In the reference [38], the T_1 values for a sample of similar concentration for a magnetic field of around 50 mT was calculated to be 2.5, we can approximate the T_1 for our sample to have a value of the same order. With this, we can estimate the relaxation process of the polarization signal between 400 mT/s to 700 mT/s to lay within the value of T_1.
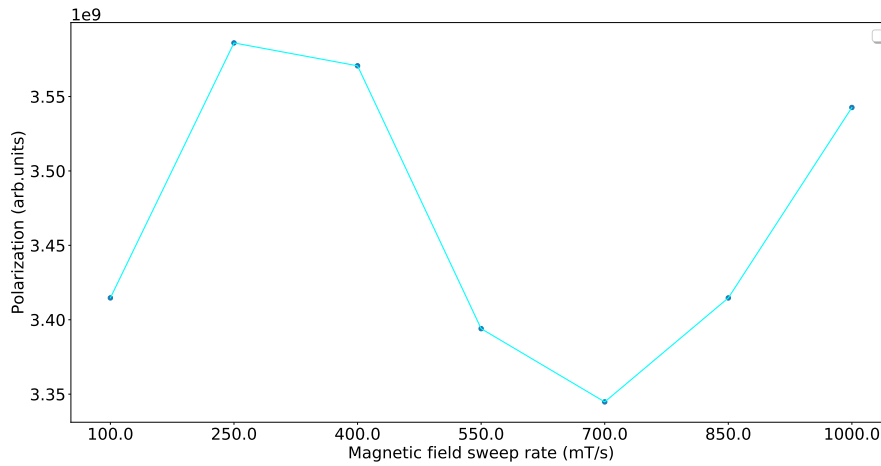
Figure 4.6: Sample id280: Real part of NMR spectra integral for the set of magnetic sweep field velocities R_s values indicated in the figure. This sample was irradiated by the laser beam with power of 3 W during 25 second per scan, the magnetic field sweeps are superposed on a static magnetic field of B = 49 mT and with a magnetic field range of δB= 6 mT, measurement for each magnetic sweep field rate is repeated 128 times

4.2.2   Results by varying the static magnetic field B

The sample used was the sample id273 in the table3.1. The irradiation power of the laser employed was of 1 W and the irradiation time was set to be 15 s. For each magnetic field value 32 scans were performed, leading to a total of 352 scans. The static magnetic field set is $B_0 = [45, 55]$ mT, the magnetic field sweep rate was set to be $R_s = 700$ mT/s and a magnetic field range δB= 2 mT. We can see in figure 4.7 that at beginning of the signal it is unclear why the polarization is built in that value, on the other hand in the magnetic field value of 48 mT, since the magnetic field range is δB= 2 mT we could suggest that the polarization is built up because of the Hyperfine coupling interaction between intrinsic ^{14}N and P1 centers, similarly with the magnetic field value of 49 mT. After passing that region the polarization decays, which is expected because of the spin lattice relaxation process.
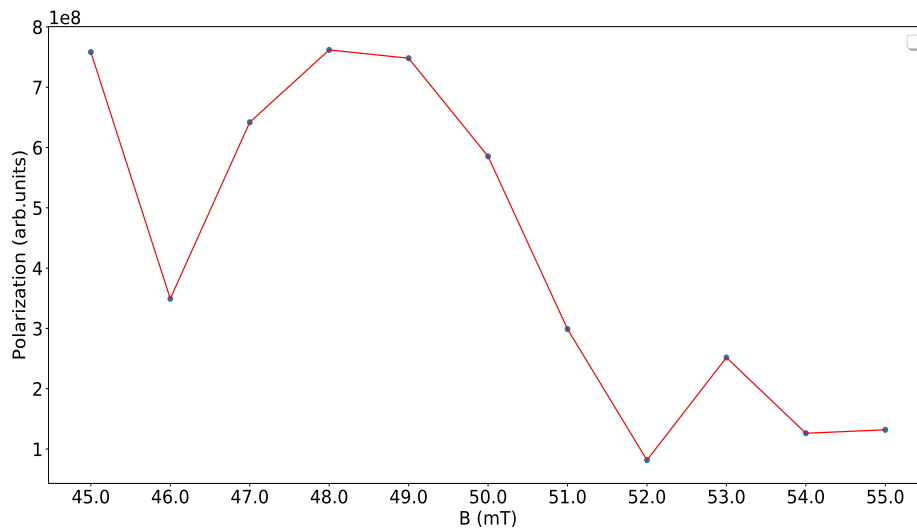
41

Figure 4.7: Sample id273: Real part of NMR spectra integral for the set of static magnetic fields indicated in the figure. This sample was irradiated by the laser beam with power of 1 W during 15 second per scan, magnetic field sweeps of δB= 2 mT and R$_s$ = 700 mT/s are superposed on a static magnetic field set of values, measurement for each magnetic sweep field rate is repeated 32 times, leading to a total of 352 scans

4.2.3 Results by varying the magnetic field range δB

The sample used was the sample id273 in table 3.1. The magnetic field range is the parameter that varies, it took five different values δB = 1, 2, 3, 4, the static magnetic field value was set to be B= 48.5 mT, and the magnetic field sweep rate that superpose the static magnetic field was set in the value R$_s$ = 700 mT/s. The irradiation power of the laser employed was of 1 W and the irradiation time was set to be 15 s. For each magnetic field range value 16 scans were performed, leading to a total of 80 scans. It shows in 4.8 that the polarization takes maximum values for the first two data points for unclear reasons, after that the relaxation occurs.
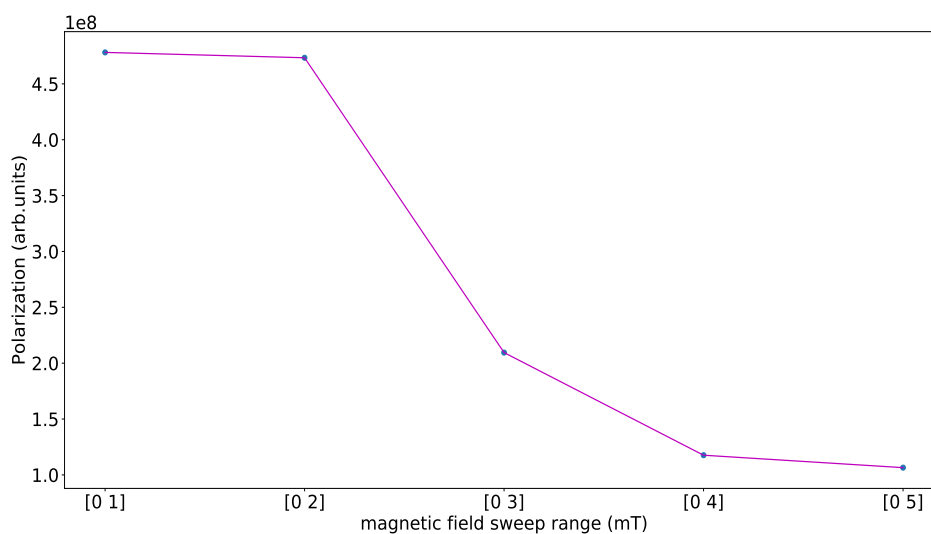
Figure 4.8: Sample id273: Real part of NMR spectra integral. The magnetic field sweep range varied through 5 values depicted in the figure . The static magnetic field was set B= 48.5 mT while the magnetic field sweep rate was set at R_s = 700 mT/s. For each magnetic field range value 16 scans were performed, leading to a total of 80 scans.

4.3 Induced cross polarization experimental results

To take this measurements, the experimental set up 1 was used with the sample id291 in table 3.1.

For this experiment 44 static different magnetic field values were applied, these laid on within a range of B = [48.5, 53.5] mT. The applied irradiation power of the laser was of 1 W. The laser irradiation time was set to be of 15 seconds per scan. The total number of scans per magnetic field value was of 33, leading to a total of 1408 scans. The irradiation power of the laser employed was of 1 W and the irradiation time was set to be 15 s. For each magnetic field value 32 scans are performed, leading to a total of 352 scans.

Figure 4.9: Sample id291: Set of averaged FID signals

Figure 4.10: Sample id291: Set of averaged FFT NMR spectra

Figure 4.11: Sample id291: Real part of NMR spectra integral for the set of static magnetic field values showed in the figure. The irradiation of the laser onto the sample was done with a power of 1W during 15 s per scan in the presence of the static field different values. The number of measurements per static magnetic field value is of 32, leading to a total of 352 scans

The polarization pattern is analyzed in the simulations chapter 6

Chapter 5

Mechanism of polarization transfer

5.1 Cross-polarization

The Cross-Polarization is a key NMR technique used to enhance the polarization signal of a nuclei spin system with a small gyromagnetic ratio (S) (e.g 13C) present in a low concentration from other spin system with larger gyromagnetic ratio (e.g 1H) present in larger concentration. This polarization transfer is possible from the last system to the first because of the dipolar coupling between the spin systems.

The Cross Polarization technique consists on applying two pulses (RF fields) at the same time to the two nuclei systems A and B, the goal is to transfer the polarization from B to A, the fields are adjusted to induce the cross-polarization,the Hartmann-Hahn condition must be fulfilled for the polarization transfer to take place.

$$\gamma_A H_{1A} = \gamma_B H_{1B} \tag{5.1}$$

The terms H_{1A} and H_{1B} are the resonant radio-frequency fields while γ_A and γ_B are the gyromagnetic ratios for the nuclei spin systems A and B. The sensitivity, which is the Magnetization enhancement is proportional to γ_B/γ_A.

In this master thesis radio-frequency fields were not employed. Nevertheless a condition an energy matching condition will be necessary for the cross-polarization to happen. This energy matching condition depends on the eigenstates of the systems involved in the Cross-polarization process and the parameters on which the evolution of the system depends.

$$\Delta E_A = \Delta E_B \tag{5.2}$$

5.2 Landau-Zener transitions

5.2.1 Landau-Zener theory

In 1932, the first description of the Landau-Zener dynamics were explained [39]. In this paper the system under study is a molecule composed by two protons separated by a distance R . Consider two electronic configurations $\varphi_1(x, R)$ and $\varphi_2(x, R)$

We have two energy eigenstates in our system. The Hamiltonians are

$$H(R)\varphi_i(x, R) = E_i(R)\varphi_i(x, R) \tag{5.3}$$
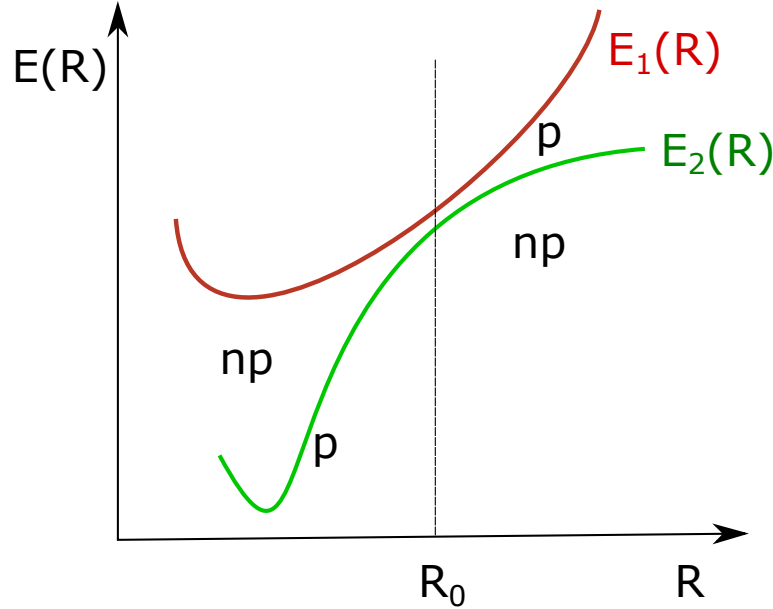
The figure (6.8) is a copy of the diagram found in [39]

Figure 5.1: Crossing of polar and non polar states at R_0 [40]

In the figure p stands for "polar molecule" (molecule with a permanent dipole moment) and np stands for "non-polar" , this figure shows how the polar and non polar characteristics in the states depend on the distance R when $R = R_0$. The relevance of the system lies on the following possible phenomena : If R changes slowly around R_0 then the states remain the same, if it changes fast then $\varphi_1(x, R) \rightarrow \varphi_2(x, R)$. This molecule can be subjected by outside interactions , therefore R can be time dependent $R(t)$.

$$H(R(t))\varphi_i(x, R(t)) = E_i(R(t))\varphi_i(x, R(t)) \tag{5.4}$$

Solving (5.3) for all values of R it is equivalent to solve (5.4) for all times t. Therefore we have the instantaneous energy eigenstates $E_i(R(t))$.

From this point, we can generalize the problem to a two level system as shown in [41] , and the position R to any parameter q which is time dependent, in the case of this master thesis this parameter would be the magnetic field sweeps amplitudes.

The generalized problem is represented by this diagram

We have now two states of a two level system $|1\rangle$ and $|2\rangle$, and two Hamiltonian operators: H_0 corresponding to the unperturbed system and $H_p = H_0 + V'$ that represents the perturbed system.

$$H_0 |n\rangle = E_n^0 |n\rangle \tag{5.5}$$

$$H_p |n\rangle = (E_n^0 + V') |n\rangle \tag{5.6}$$

47

Which leads to the energy eigenvalues for the perturbed system:

$$E_n(q) = E_n^0(q) + \langle n| V' |n\rangle \tag{5.7}$$

The perturbed Hamiltonian H_p in the ordered basis $|1\rangle$ and $|2\rangle$ can be expressed in a matrix form.

$$H_p(q) = \begin{pmatrix} E_1^0 + \langle 1| V' |1\rangle & \langle 1| H_0 |2\rangle + \langle 1| V' |2\rangle \\ \langle 2| H_0 |1\rangle + \langle 2| V' |1\rangle + & E_2^0 + \langle 2| V' |2\rangle \end{pmatrix} \tag{5.8}$$

The terms $\langle 1| V' |1\rangle$ and $\langle 2| V' |1\rangle$ are zero, as well as the terms $\langle 2| H_0 |1\rangle$ and $\langle 1| H_0 |2\rangle$. The non-diagonal terms can be rewritten in terms of a new variable $E_0 = 2 \langle 1| V' |2\rangle$. With these simplifications 5.8 is reduced to :

$$H_p(q) = \begin{pmatrix} E_1(q) & \frac{1}{2}E_0 \\ \frac{1}{2}E_0 & E_2(q) \end{pmatrix} \tag{5.9}$$

The eigenvalues of the perturbed Hamiltonian H_p are :

$$E_\pm = \frac{1}{2}\left(E_1 + E_2 \pm \sqrt[2]{(\Delta E(q))^2 + E_0^2} \right) \tag{5.10}$$

The term $\Delta E(q) = E_1 - E_2$ The eigenstates of the perturbed Hamiltonian (H_p)are $|a\rangle$ and $|b\rangle$ with the respective energy eigenvalues $E_a = E_+$ and $E_b = E_-$.

From the diagram we can see that in the unperturbed case H_0 (with eigenenergies represented by the dashed straight lines) the system has a degeneracy point q_c. According to the *non-crossing theorem*, the degeneracy of the unperturbed system H_0 is broken due to the presence of the perturbation V' that couples the energy levels , this cause the energy levels to repel . The avoided crossing area is characterized by the separation between the energies E_0 and by the width q_0.

The behaviour of the system during a time interval (t_i, t_f) that correspond to the change of the general parameter $q(t)$ in the interval $(q_i(t_i), q_f(t_f))$. Assuming that the state of the perturbed Hamiltonian H_p is a linear combination of its basis $|a\rangle$ and $|b\rangle$: $\psi(t) = c_a(t) |a\rangle + c_b(t) |b\rangle$, and that at time t_i the initial state is $|b\rangle$, the probability that the system has to made a *diabatic* transition to $|a\rangle$ is given by:

$$P_{b\to a} = |c_a(t_f)|^2 = |\langle \psi(t_f)|a\rangle|^2 \tag{5.11}$$

E_1 and E_2 are a linear in function of q, and q is swept at a constant rate Γ through the avoided crossing, in the limits of $t_i \to -\infty$ and $t_f \to +\infty$ the *diabatic transition* (non-adiabatic transition) from $|b\rangle$ to $|a\rangle$ is equivalent to go through $|1\rangle$ to $|1'\rangle$, as well as the state to remain *adiabatic* in $|b\rangle$ is equivalent for the state to go from $|1\rangle$ to $|2'\rangle$. Under these time limits the probability (5.11) can be solved as it is shown in [41] and in more detail in

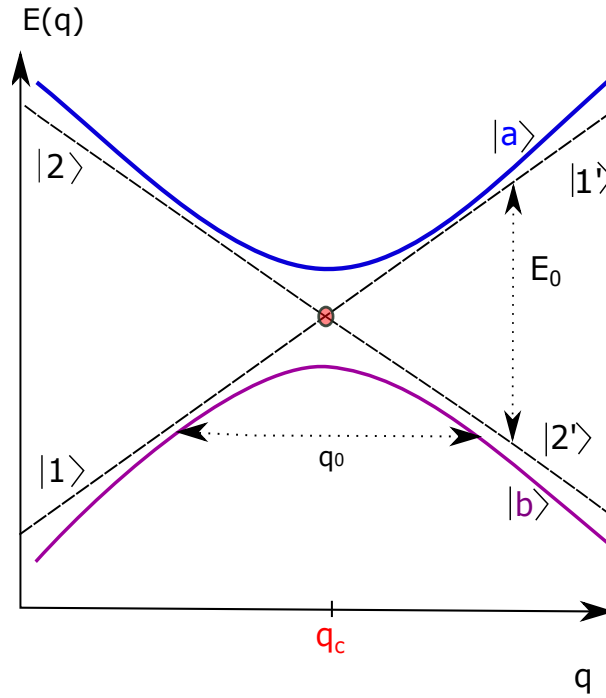$$P_{1\to 1'} = \exp(-2\pi\Gamma) \tag{5.12}$$

Figure 5.2: Energy diagram as a function of the general parameter q, the unperturbed states are represented by $|1\rangle, |1'\rangle$ and $|2\rangle, |2'\rangle$, the primed states are the states of the system for $q > q_c$, the perturbed states by $|a\rangle$ and $|b\rangle$

The parameter *Landau Zener* parameter Γ is

$$\Gamma = \frac{|\langle 1| V' |2\rangle|^2}{\hbar (dE/dq)(dq/dt)} \tag{5.13}$$

The expression 5.12 is the *Landau Zener transition probability* for this special case with the time conditions $t_i \to -\infty$ and $t_f \to +\infty$. In practice, the Landau-Zener transition problem can not be solved analytically, but numerically. Nevertheless, from this simple case we can gain some understanding of the Landau-Zener transitions which are transferable to real systems.

From (5.13) it is clear that when the sweep is very slow $dq/dt \to 0$ the system will stay in the initial state $|b\rangle$ which means that the diabatic probability transition from $|1\rangle$ to $|1'\rangle$ is $P_{1\to1'} \to 0$. Conversely, when the sweep is fast $dq/dt \to \infty$ the diabatic transition probability is high $P_{1\to1'} \to 1$. In addition, the parameter E_0 also plays a complementary role to the sweep dq/dt, this is also noticeable from the energy levels diagram 5.2 : If $|\langle 1| V' |2\rangle| \to 0$ then the diabatic transition $P_{1\to1'} \to 1$ [42]

Chapter 6

Simulations

In this section the results and simulations are presented in two separate subsections according to the polarization transfer mechanism under which each of the two experimental arrays were prepared.

The simulations performed in this master thesis were performed using the `Python` based toolkit named `Qutip`[43] were employed.

6.1 Cross Polarization transitions

Studies such as [38] already demonstrated the efficiency of NV centers to transfer at room temperature electronic polarization to nuclear ^{13}C spins by exploiting the optical initialization property of NV centers and the Hyperfine interactions of a NV-P1-^{13}C.

In this master thesis the experiment and simulations performed to study the polarization transfer in the system NV-P1-^{13}C, following the work in [44]. In this reference, the Hyperpolarization is attributed to the optically induced cross relaxation (cross-polarization) of the NV centers in $m_s^{NV} = 0$ with the P1 center at certain magnetic field values.

This section is based on the work [44]. The experimental procedure already explained in chapter 3 is based on optically initializing the NV centers to $m_s^{NV} = 0$ by laser irradiation and applying a set of magnetic fields in the Z direction (considered to be parallel to one of the four equivalent [111] NV center orientations), the values of this magnetic field are chosen to be in the range of 48 and 54 mT.

It is necessary to describe the quantum mechanical model used to perform the cross polarization simulations. This is composed by two independent subsystems which are described by the following two Hamiltonian operators:

$$H^{NV} = D(S_z^{NV})^2 + \gamma \bar{B}.\bar{S}^{NV} + {}^{13C}A\bar{S}^{NV}.\bar{I}^{13C}$$

$$H_{O,NO}^{P1} = \gamma \bar{B}.\bar{S}^{P1} + A^{O,NO}\bar{S}^{P1}.\bar{I}^N$$

(6.1)

Z axis. The first term in H^{NV} corresponds to the zero-field splitting term of the *NV* center in its ground state $m_s = 0$ at room temperature , the parameter D denotes the ZFS parameter for the ground state D=2870 MHz .

The second term represents the Zeeman interaction of the NV center due to $\bar{B}$, the constant γ=28.03 MHz/mT is the gyromagnetic value for the electron. The third term represents the isotropic fine interaction between the NV electron spin S^{NV} and the neighboring nuclear spin I^{13C} with an Hyperfine constant ^{13C}A= 2 MHz .

Considering the tetrahedral structure of the lattice, the P1 Hamiltonian subsystem is also divided into two subsystems according to the P1 centers aligned (O) with the Z axis and the P1 centers not aligned (NO) forming an angle ϕ=109° with the NV center , the non aligned and aligned P1 centers exist in a relative abundance of (1:3). Their respective Hyperfine coupling tensors ,in MHz units, for the aligned and non-aligned P1 centers are given respectively by A^O and A^{NO}.

$$A^O = \begin{pmatrix} 81 & 0 & 0 \\ 0 & 81 & 0 \\ 0 & 0 & 114 \end{pmatrix} \qquad A^{NO} = \begin{pmatrix} 100 & 0 & 10 \\ 0 & 81 & 0 \\ 10 & 0 & 85 \end{pmatrix}$$
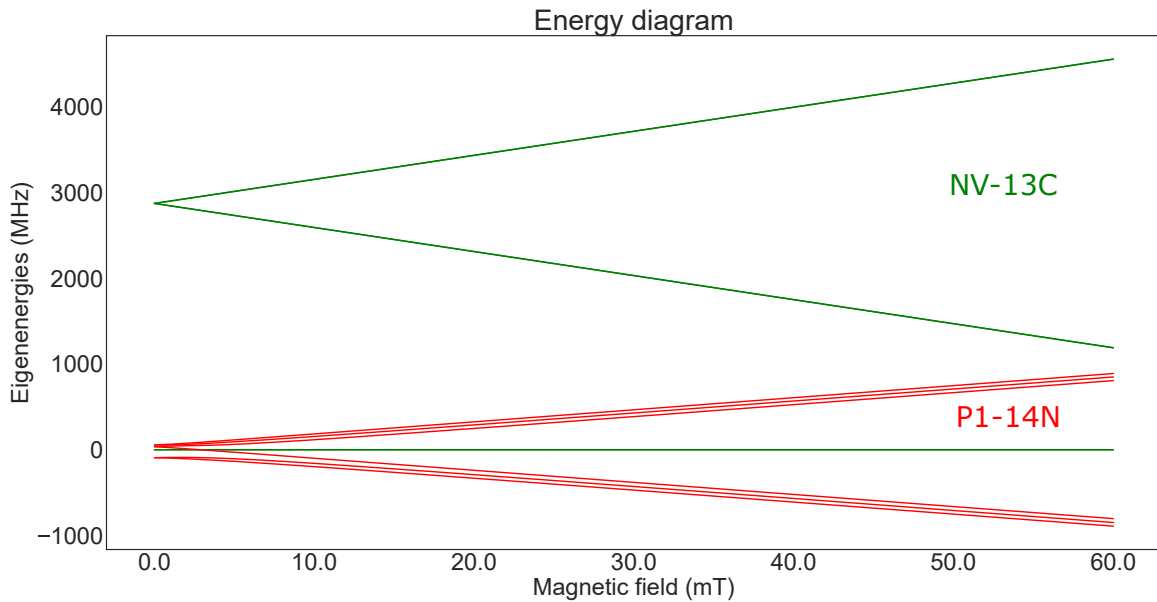

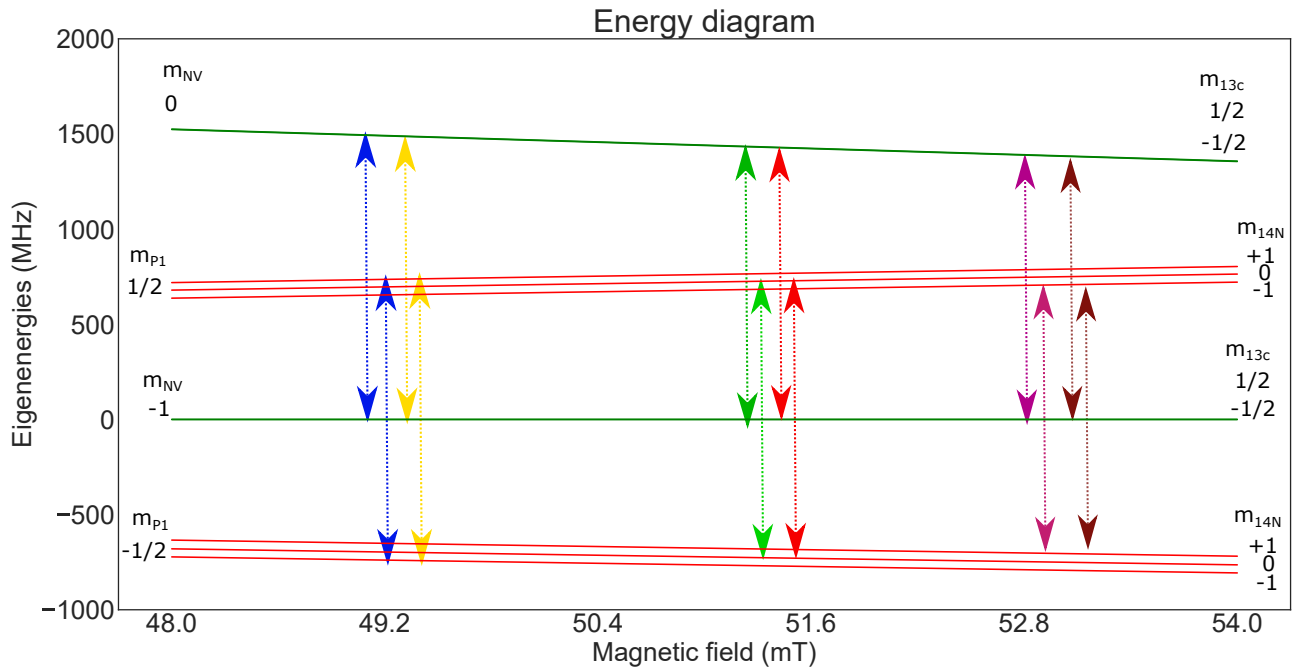**Figure 6.1:** Energy diagram of the composite system 6.1 for a magnetic field range B(mT)=(0,60)

51

Figure 6.2: Amplified energy diagram of the composite system on the magnetic field range B(mT)=(48,54). The arrows represent roughly the magnetic field values at which the cross polarization can occur

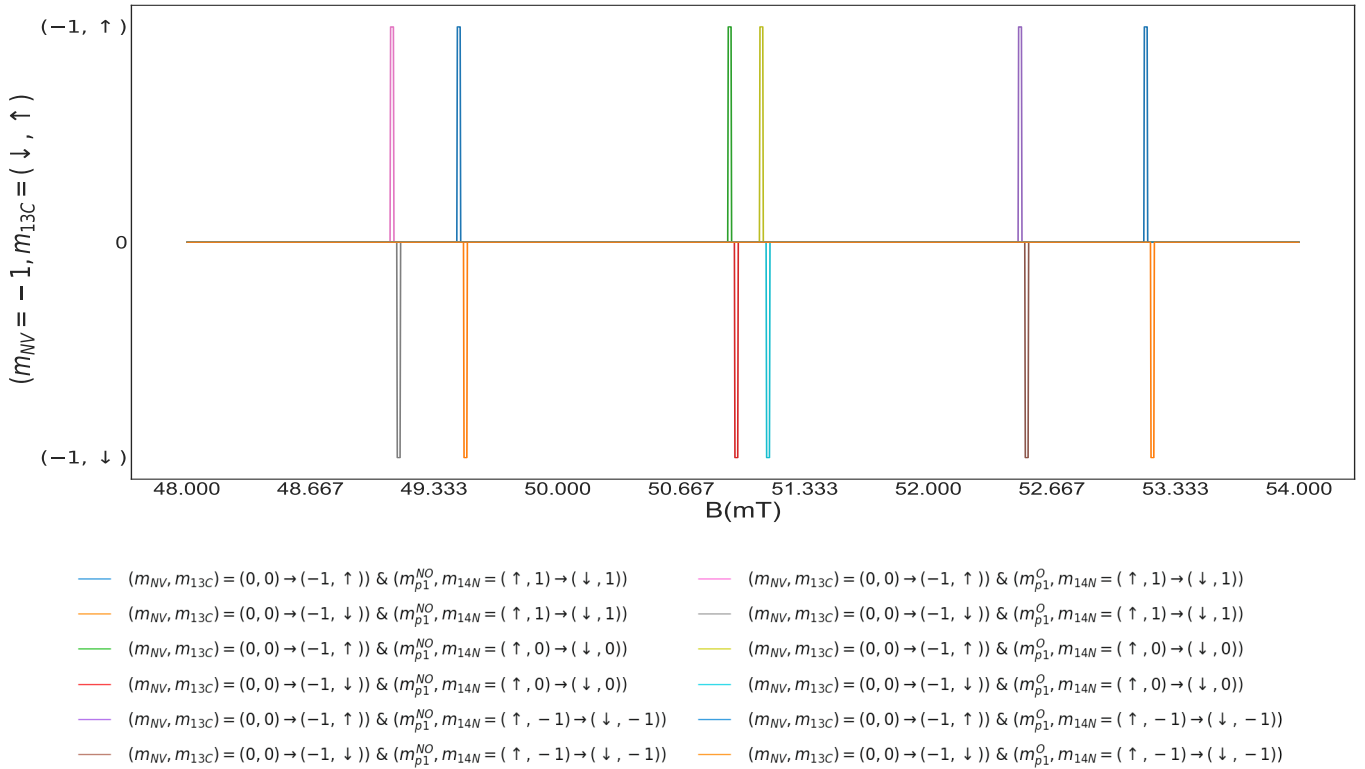|	
$(m_{NV}, m_{13C}) = (0,0) \rightarrow (-1,\uparrow)$ & $(m_{p1}^{NO}, m_{14N} = (\uparrow,1) \rightarrow (\downarrow,1))$	$(m_{NV}, m_{13C}) = (0,0) \rightarrow (-1,\uparrow)$ & $(m_{p1}^{O}, m_{14N} = (\uparrow,1) \rightarrow (\downarrow,1))$
$(m_{NV}, m_{13C}) = (0,0) \rightarrow (-1,\downarrow)$ & $(m_{p1}^{NO}, m_{14N} = (\uparrow,1) \rightarrow (\downarrow,1))$	$(m_{NV}, m_{13C}) = (0,0) \rightarrow (-1,\downarrow)$ & $(m_{p1}^{O}, m_{14N} = (\uparrow,1) \rightarrow (\downarrow,1))$
$(m_{NV}, m_{13C}) = (0,0) \rightarrow (-1,\uparrow)$ & $(m_{p1}^{NO}, m_{14N} = (\uparrow,0) \rightarrow (\downarrow,0))$	$(m_{NV}, m_{13C}) = (0,0) \rightarrow (-1,\uparrow)$ & $(m_{p1}^{O}, m_{14N} = (\uparrow,0) \rightarrow (\downarrow,0))$
$(m_{NV}, m_{13C}) = (0,0) \rightarrow (-1,\downarrow)$ & $(m_{p1}^{NO}, m_{14N} = (\uparrow,0) \rightarrow (\downarrow,0))$	$(m_{NV}, m_{13C}) = (0,0) \rightarrow (-1,\downarrow)$ & $(m_{p1}^{O}, m_{14N} = (\uparrow,0) \rightarrow (\downarrow,0))$
$(m_{NV}, m_{13C}) = (0,0) \rightarrow (-1,\uparrow)$ & $(m_{p1}^{NO}, m_{14N} = (\uparrow,-1) \rightarrow (\downarrow,-1))$	$(m_{NV}, m_{13C}) = (0,0) \rightarrow (-1,\uparrow)$ & $(m_{p1}^{O}, m_{14N} = (\uparrow,-1) \rightarrow (\downarrow,-1))$
$(m_{NV}, m_{13C}) = (0,0) \rightarrow (-1,\downarrow)$ & $(m_{p1}^{NO}, m_{14N} = (\uparrow,-1) \rightarrow (\downarrow,-1))$	$(m_{NV}, m_{13C}) = (0,0) \rightarrow (-1,\downarrow)$ & $(m_{p1}^{O}, m_{14N} = (\uparrow,-1) \rightarrow (\downarrow,-1))$

Figure 6.3: Energy matching conditions as a function of the magnetic fields

The energy eigenvalues and eigenvectors are obtained by solving numerically the eigenvalue problem for each Hamiltonian that compose the system, the energy diagram is represented in the figure 6.1.

In the energy diagram figure 6.2 the location of the vertical arrows indicate the magnetic field values where the energy matching condition necessary for the cross-relaxation to happen. Precisely, where the energy difference between the corresponding states $|m_s^{P1} = +1/2\rangle$ and $|m_s^{P1} = -1/2\rangle$ coincides with the energy difference between $|m_s^{NV} = 0\rangle$ and $|m_s^{NV} = -1\rangle$ within an energy threshold $\delta E = \pm 0.5$ MHz. Where the energy matching conditions are met, the expectation value of I_z^{13C} of the subsystem H^{NV} eigenfunctions is appended in a list to determine the spin polarization 6.3

The polarization signals in the simulations were obtained via the convolution of the polarization with a Gaussian function with a full width at half maximum of 0.15 mT.

The experimental results were presented in chapter 4 4.11 scaled to compare it with the simulation plot. In the figure 6.4, the simulation assumes that the applied magnetic field $\bar{B}$ is parallel to the Z axis as it was prepared in the experiment. Nevertheless, a better fitting between the results and the simulation 6.5 takes place when the simulation is performed considering a $\theta = 4°$ between the $\bar{B}$ and the NV axis. This can be attributed to issues related to the experimental set up shuttling process that prevented the sample to be aligned with respect the applied magnetic field $\bar{B}$.

On the other hand, comparing the simulation part of the plots 6.4 and 6.5, the polarization pattern is shifted to the right, in the case where both orientations were present in the sample, the negative and positive parts of the polarization pattern could cancel each other.

Approximately, in the region after B=52 mT, the experimental results do not match with the simulation. This can be attributed to the power instability of the laser that prevents the NV centers ensemble to initially completely polarize to $m_s = 0$.

In the simulation performed only single quantum transitions were considered. Conversely, the so called forbidden quantum transitions were not considered in the simulation. Regardless, around B=50.5 mT and B=52.0 mT two small peaks are observed and could be related to the forbidden transitions if compared to [44] figure 3.
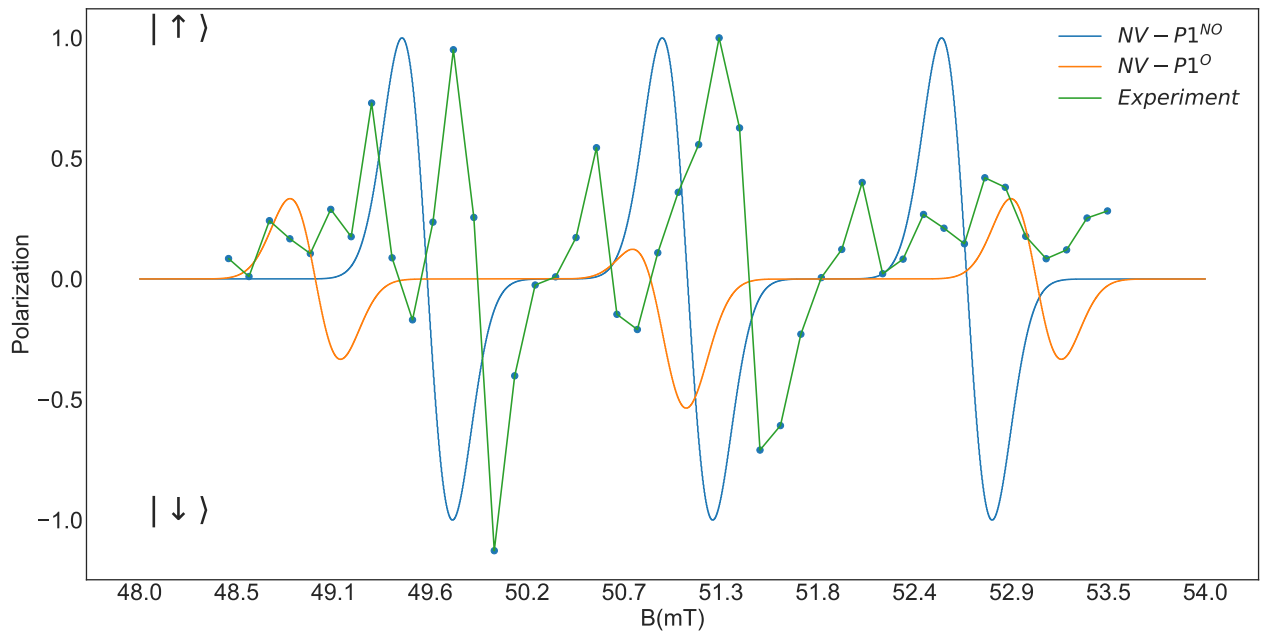
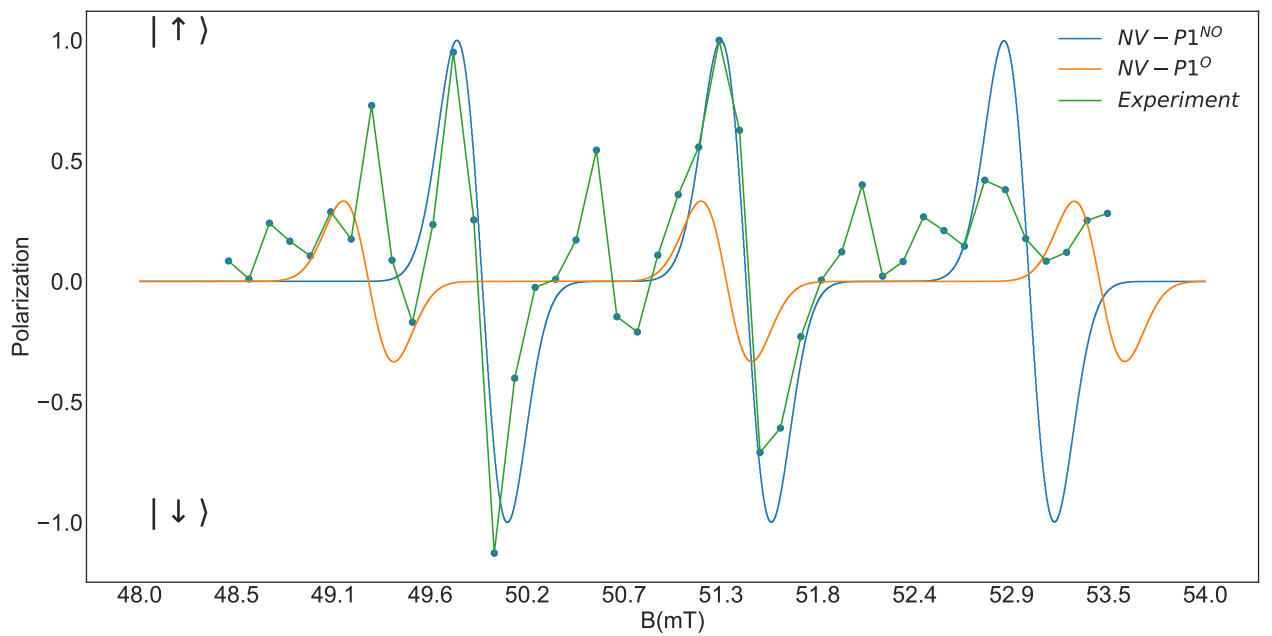**Figure 6.4:** Simulation and experimental result comparison for $\theta=0°$

Figure 6.5: Simulation and experimental result comparison for $\theta=4°$

6.2 Landau Zener induced transitions via magnetic field sweeps

In this subsection the dynamics of the NV–P1–^{13}C system is studied when the magnetic field sweeps are superposed to a static magnetic field $\overline{B}$ in principle oriented along the Z axis, as described in the experimental methods chapter of this master thesis 3, the dynamics can be explained with the Landau-Zener theory . The reference [45] is the main source in which this section is based.

First, in contrast to the Cross polarization case, the Hamiltonian system is not subdivided by two independent Hamiltonian terms but one total Hamiltonian with dipolar coupling terms between NV and P1 as well as between ^{13}C and NV. These last are the perturbation terms mentioned in chapter 5 that make possible the cross polarization of NV and P1 centers which leads to the dynamical polarization of ^{13}C nuclei.

$$H_{dip}^{P1,NV} = \frac{\mu_0 \gamma \gamma \hbar \pi}{r_1^3} \left(\bar{S}^{NV}.\bar{S}^{P1} - 3(\bar{S}^{NV}.\hat{r}_1)(\bar{S}^{P1}.\hat{r}_1) \right) \tag{6.2}$$

$$H_{dip}^{13C,NV} = \frac{\mu_0 \gamma_{13C} \gamma \hbar \pi}{r_2^3} \left(\bar{S}^{NV}.\bar{I}^{13C} - 3(\bar{S}^{NV}.\hat{r}_2)(\bar{I}^{13C}.\hat{r}_2) \right) \tag{6.3}$$

In the dipolar interaction terms, r_1 and r_2 are the modules of the vectors $\bar{r}_1$ and $\bar{r}_2$ that connect the already indicated spins, the respective unitary vectors are denoted by $\hat{r}_1$ and $\hat{r}_2$.
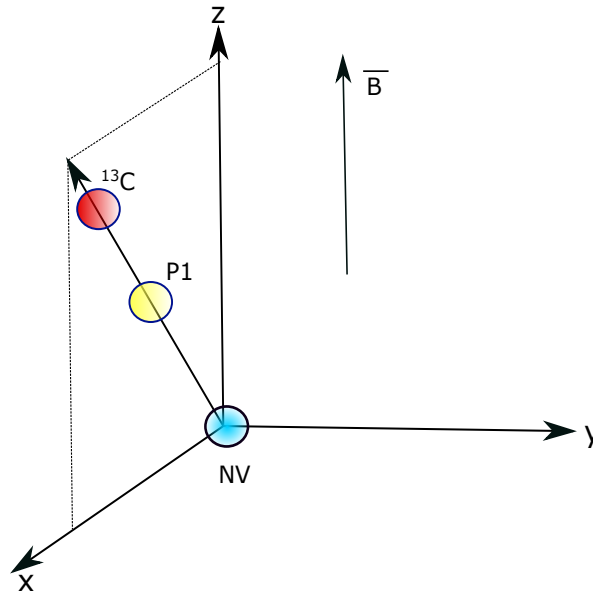

Figure 6.6: Scheme of the three spin system axes on the XZ plane, the magnetic field in this case is aligned in the Z axis

It is assumed that the the three spin system is collinear and its main axis lay on the $X - Z$ plane, similar to [46]. The three spin system can lay in any plane that includes the Z axis since that is the direction of the magnetic field.

The dipolar coupling Hamiltonian terms are defined by the dipolar coupling parameters outside the parentheses in 6.2 and 6.3 which are function of the distance modules that connect the spins.

$$H_{dip}^{P1,NV} = C_{NV-P1} \left(\bar{S}^{NV}.\bar{S}^{P1} - 3(\bar{S}^{NV}.\hat{r}_1)(\bar{S}^{P1}.\hat{r}_1) \right) \tag{6.4}$$

$$H_{dip}^{13C,NV} = C_{NV-13C} \left(\bar{S}^{NV}.\bar{I}^{13C} - 3(\bar{S}^{NV}.\hat{r}_2)(\bar{I}^{13C}.\hat{r}_2) \right) \tag{6.5}$$

In this master thesis, the value used for the coupling parameter between ^{13}C and NV center is C_{NV-13C} =0.92 MHz, this had been take it from the main reference [45].

NV-P1 dipole interaction coupling parameters estimation

The average distance between the P_1 and NV centers can be estimated from the concentration values of the P_1+NV centers calculated from the EPR CW-pulse experiments performed. This information is showed in the table 3.1

Two different approaches were tried to make an estimation of the coupling constant values between NV and P1 centers C_{NV-P1}. The first approach is going to be called Method I, which is based on obtaining the average distance between the defects from the concentration values (NV+P1) , the unit cell volume of the diamond lattice and the number of atoms per unit cell.

$$\text{Distance(nm)} = \left(\frac{a^3 c_u}{C^{P1}} \right)^{1/3} \tag{6.6}$$

In the expression 6.6 : The parameter C^{P1} is the concentration of P1 centers , the parameter (a) is the lattice constant of diamond and c_u is the number of carbon atoms per unit cell.

$$C^{P1} = \frac{C^{P1}(\text{ppm})}{10^6} \qquad\qquad a = 0.3567 \, \text{nm} \qquad\qquad c_u = 8$$

From the estimated distance the coupling constant is calculated. The values obtained are depicted in the table below.

sample id	distance (nm)	C_{NV-P1} (MHz)
280	16	0.08
277	19	0.05
276	17	0.06
275	18	0.05
274	17	0.06
273	18	0.05
291	22	0.03

Table 6.1: Average defect distance and their coupling strength parameters between NV-P1 defects calculated with the method I
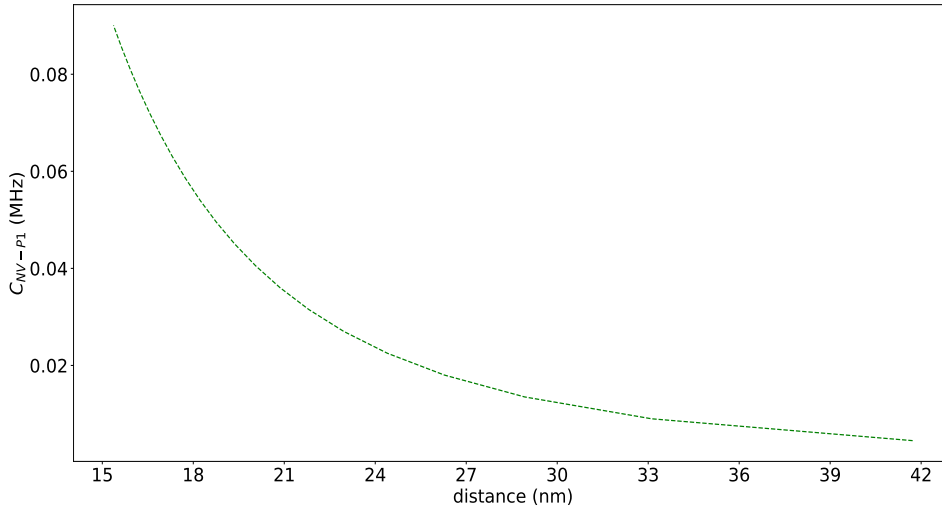
Figure 6.7: Method I: Dipolar coupling constant as a function of the average defect distance

The second approach is executed by applying a function [1] that calculate the average inter particle distance between NV and P1 centers from the Poisson distribution $P(r) = \exp\left(-4\pi N_c r_{ij}^3/3\right)$ where r_{ij} is the inter particle distance between particle i and j and N_c concentration in cm^{-3} [47], from this method the average inter particle distance from the concentration of P1 is given by

$$\text{Distance(nm)} = \left(\frac{3\text{M}\ln(0.5)10^{21}}{4\pi N_a \rho_C C^{P1}}\right)^{1/3} \tag{6.7}$$

In the expression 6.7 :The parameter M is the mass of carbon in atomic units, the parameter C^{P1} is the concentration of P1 centers , the parameter N_A is the Avogadro's number and ρ_C is the density of carbon in the form of diamond.

$$\text{M} = 12.011\,\text{amu} \qquad C^{P1} = \frac{C^{P1}(\text{ppm})}{10^6} \qquad N_A = 6.022\,141\,29 \times 10^{23}\,\text{mol}^{-1} \qquad \rho_C = 3.51\,\text{g\,cm}^{-3}$$

---

[1]This function was provided by Johannes Engel in a python script form

sample id	distance (nm)	C_{NV-P1} (MHz)
280	4.7	3.1
277	5.6	1.9
276	5.1	2.4
275	5.4	2.0
274	5.3	2.2
273	5.4	2.0
291	6.6	1.1

Table 6.2: Average defect distance and their coupling strength parameters between NV-P1 defects calculated with the method II
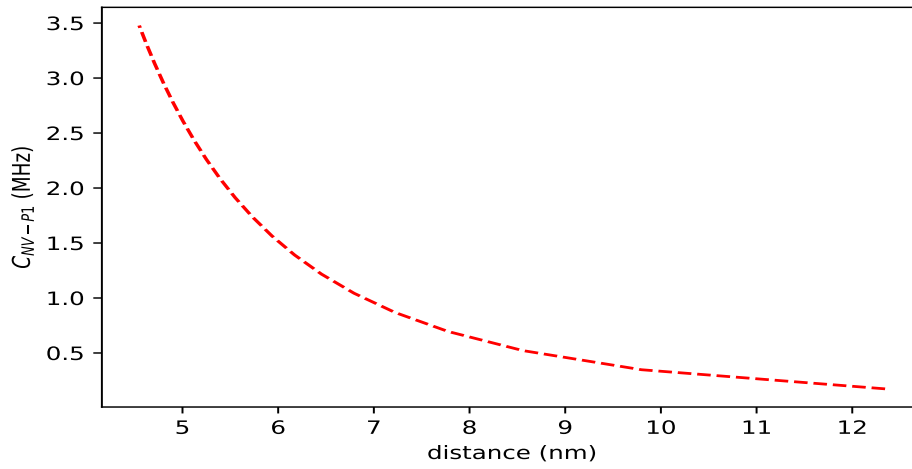

Figure 6.8: Method II: Dipolar coupling constant as a function of the expected defect distance

Two coupling constants C_{NV-P1} obtained by each method were used in the simulations in order to compare which method gives a value of C_{NV-P1} such that the dynamic nuclear polarization is more effective while C_{NV-13C} is kept at the value 0.92 MHz

In this work, it is not considered the Hyperfine coupling between P1 electron spin and its intrinsic ^{14}N nuclear spin neither between NV electron spin with ^{14}N nuclear spin. The reason for this is to preserve the simplicity of energy eigenvalues diagram since including those terms makes the energy diagram more complex and the simulation time also becomes longer. Moreover, the inclusion of these terms do not impact the system dynamics [45]

The Hamiltonian model that describes the NV–P1–^{13}C three-spin system for the static magnetic field B is denoted as H_0 :

$$H_0 = H_{ZFS}^{NV} + H_{dip}^{13C,NV} + H_{dip}^{P1,NV} + H_Z^{NV} + H_Z^{P1} + H_Z^{13C} \tag{6.8}$$

Where the term H_{ZFS}^{NV} is the zero field splitting Hamiltonian term and H_Z are Zeeman Hamiltonian terms for each spin. The Hamiltonian used is the one founded in the supplemental information in [48]

$$H_0 = D(S_z^{NV})^2 - \gamma \bar{B}.\bar{S}^{NV} - \gamma \bar{B}.\bar{S}^{P1} - \gamma_{13C}\bar{B}.\bar{I}^{13C} + C_{NV-P1}\left(\bar{S}^{NV}.\bar{S}^{P1} - 3(\bar{S}^{NV}.\hat{r}_1)(\bar{S}^{P1}.\hat{r}_1)\right)$$
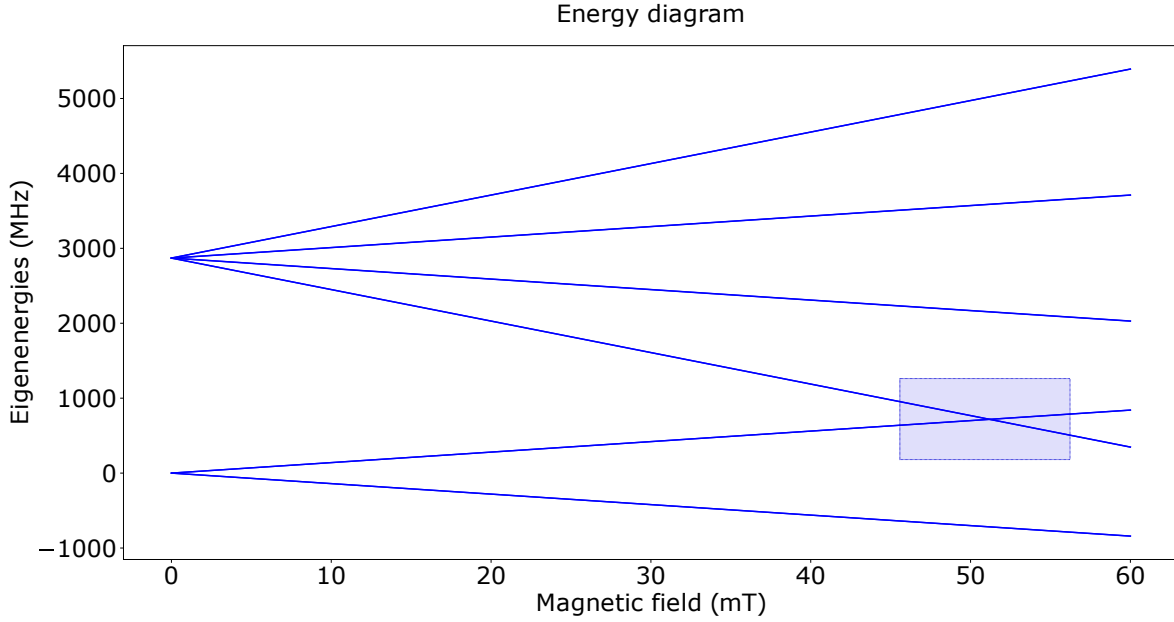$$+ C_{NV-13C}\left(\bar{S}^{NV}.\bar{I}^{13C} - 3(\bar{S}^{NV}.\hat{r}_2)(\bar{I}^{13C}.\hat{r}_2)\right) \tag{6.9}$$

Figure 6.9: Calculated energies eigenvalues as a function of the applied magnetic field along the Z axis. The shaded region is the avoided crossing region

The figure 6.9 presents the energy diagram as a function of the magnetic field, the shaded region is the avoided crossing region where the states $|0, 1/2, \downarrow\rangle$ and $|-1, -1/2, \uparrow\rangle$ nearly degenerate therefore the polarization transfer can take place.

The Hamiltonian that simulates the dynamic nuclear polarization via magnetic field sweeps is a modification of the Hamiltonian H_0 to a time dependent Hamiltonian H by introducing the magnetic field sweep rate R_s which, as seen in the toy example of chapter 5, is a key parameter that determine whether or not the diabatic transitions will take place. Similarly as in [49], the Hamiltonian can be expressed as follows, similar to how it is written in [49]

$$H = H_0 + H_Z(t)H_0 + R_s\left(\gamma S_z^{NV} + \gamma S_z^{P1} + \gamma_{13C}S_z^{13C}\right) \tag{6.10}$$

The system is considered closed since the interaction with the environment is not contemplated, therefore the evolution of the states Ψ and the eigenvalues are governed by the Schrö dinger equation which is solved numerically with the The Lindblad Master Equation Solver function (mesolve) from the python module QUTIP. Mesolve function.

$$i\hbar\frac{\partial \Psi}{\partial t} = \hat{H}\Psi \tag{6.11}$$

59

The following diagrams depicts the energy eigenvalues for the Hamiltonian H_0 near the avoided crossing region of one of the simulations performed, the purpose of this diagram is to introduce a relevant concept called energy gaps Δ_1 and Δ_0.
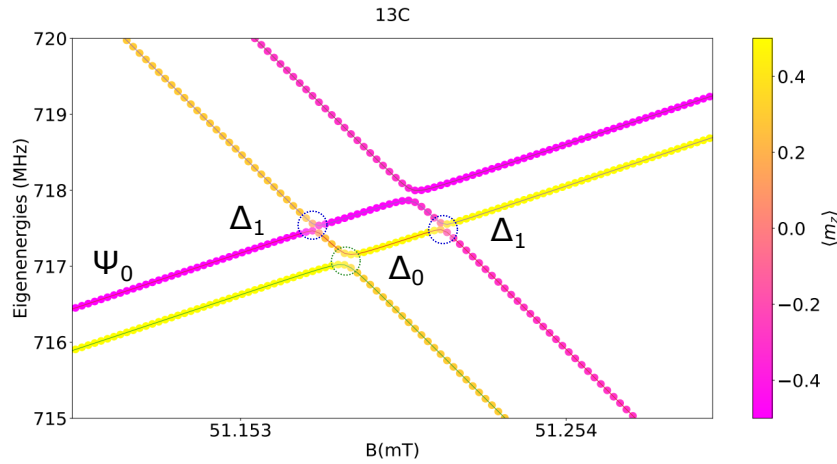

Figure 6.10: Energy diagram around the avoided crossing region , the energy gaps Δ_1 and Δ_0 are depicted in the figure. Generally, $\Delta_0 > \Delta_1$. The initial state Ψ_0 is also located in the figure

For all the Landau-Zener simulations performed in this master thesis , at the time t = 0, 100% of the NV centers are polarized in the $m_{NV} = 0$. Accordingly, the chosen initial state is $\Psi_0 = |0, 1/2, \downarrow\rangle$, where $m_{NV} = 0$, $m_{P1} = 1/2$ and $m_{13C} = -1/2$ represented by a down oriented arrow $\downarrow$.

The simulations are performed for a range of parameters R_s and magnetic field sweep range fixed for all simulations as $\delta B = 0.5$ mT with magnetic field initial and final values of $B_I = 51$ mT and $B_f = 51.5$ mT.

An estimation of which order of magnitude the energy gaps Δ_1 and Δ_0,indicated in the energy diagram 6.10, should have in order to optimize the Landau Zener dynamics can be useful. These gaps are defined by the values of the coupling strength parameters between C_{NV-P1} and C_{13C-NV}. According to the simulations here performed, the energy gaps Δ_1 and Δ_0 must lay in a restrictive range of values of maximum some tens of kHz when the sweep fields velocities take values in the range of those employed in the experiments: Between 100 mT/s and 2000 mT/s. A more accurate calculation is done with the Hamiltonian matrix representation of H_0 in [48] supplemental information.

In 5 considering expressions 5.12 and 5.13 and figure 5.2 it is clear that the varying parameter parameter q is the magnetic field $\bar{B}$ in our case, the parameters that determine the non-adiabatic (also known as diabatic) probability of crossing the gap Δ_1 is :

$$P_1 = \exp\left\{-\frac{\pi}{2} \times \frac{\Delta_1^2}{(2|\gamma| + \gamma_{13c})R_s}\right\} \tag{6.12}$$

The parameter R_s is the slope of the magnetic field sweeps. From this last expression, we can see that the interplay between Δ_1 and R_s are determinant parameters for the Landau Zener transitions to take place or not. Nevertheless, 6.12 alone does not model the polarization transfer, but also the probability of non adiabatic crossing the gap Δ_0 according to [45] is taken into consideration.

To decide a range in which the values of C_{NV-P1} are the best to induce the non-adiabatic Landau Zener transitions, we present four simulations for four different C_{NV-P1} values, two from the tables 6.1 and 6.2, and two intermediate values.

Before performing the simulations, it is noticeable that the C_{NV-P1} from 6.2 are to big and therefore the transitions are most likely to be adiabatic. For the case of $C_{NV-P1} = 1.1$ MHz, considering that $C_{13C-NV} = 0.92$ MHz, the diagram that corresponds to the energy eigenvalues obtained from the Hamiltonian H_0 is depicted below

Figure 6.11: Energy eigenvalues of the static Hamiltonian, with dipolar couplings C_{NV-13C}=0.92 MHz and C_{NV-P1}= 1 MHz, as a function of the magnetic fields around the avoided crossing. The color map bar indicates the expectation values of I_z correspondent to ^{13}C

Graphically, we can see that the energy gap Δ_1 is multiple times bigger than required, this feature makes the transition probability $P_1 \rightarrow 0$. Therefore the evolution of the expectation values of I_z is dominantly adiabatic as showed in 6.14, 6.15 and 6.16 for all the sweep magnetic field rates R_s included in the simulations.

For the rest of simulations with the other three different values for C_{NV-P1}, only the energy diagram color coded with respect to I_z of ^{13}C and the evolution of I_z with respect the magnetic field will be presented in this document because of text compilation difficulties.
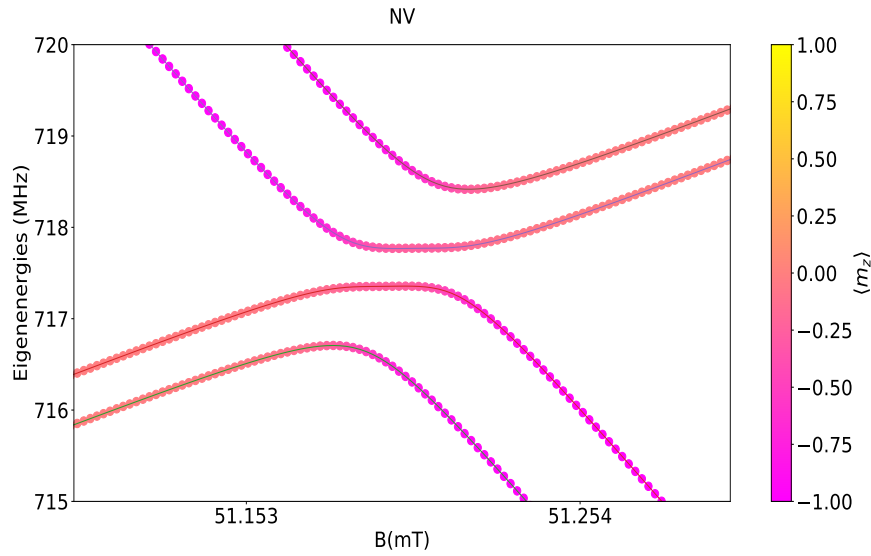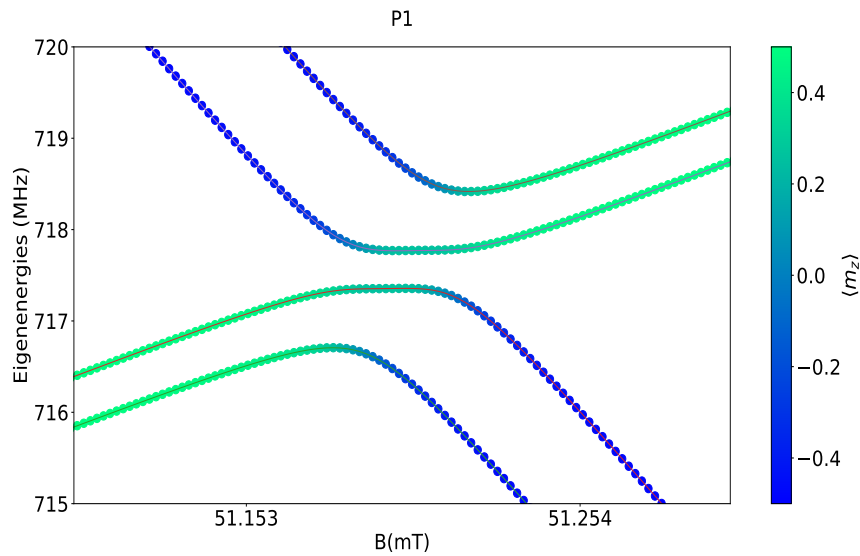
Figure 6.12: Energy eigenvalues of the static Hamiltonian, with dipolar couplings C_{NV-13C}=0.92 MHz and C_{NV-P1}= 1 MHz, as a function of the magnetic fields around the avoided crossing. The color map bar indicates the expectation values of S_z correspondent to NV
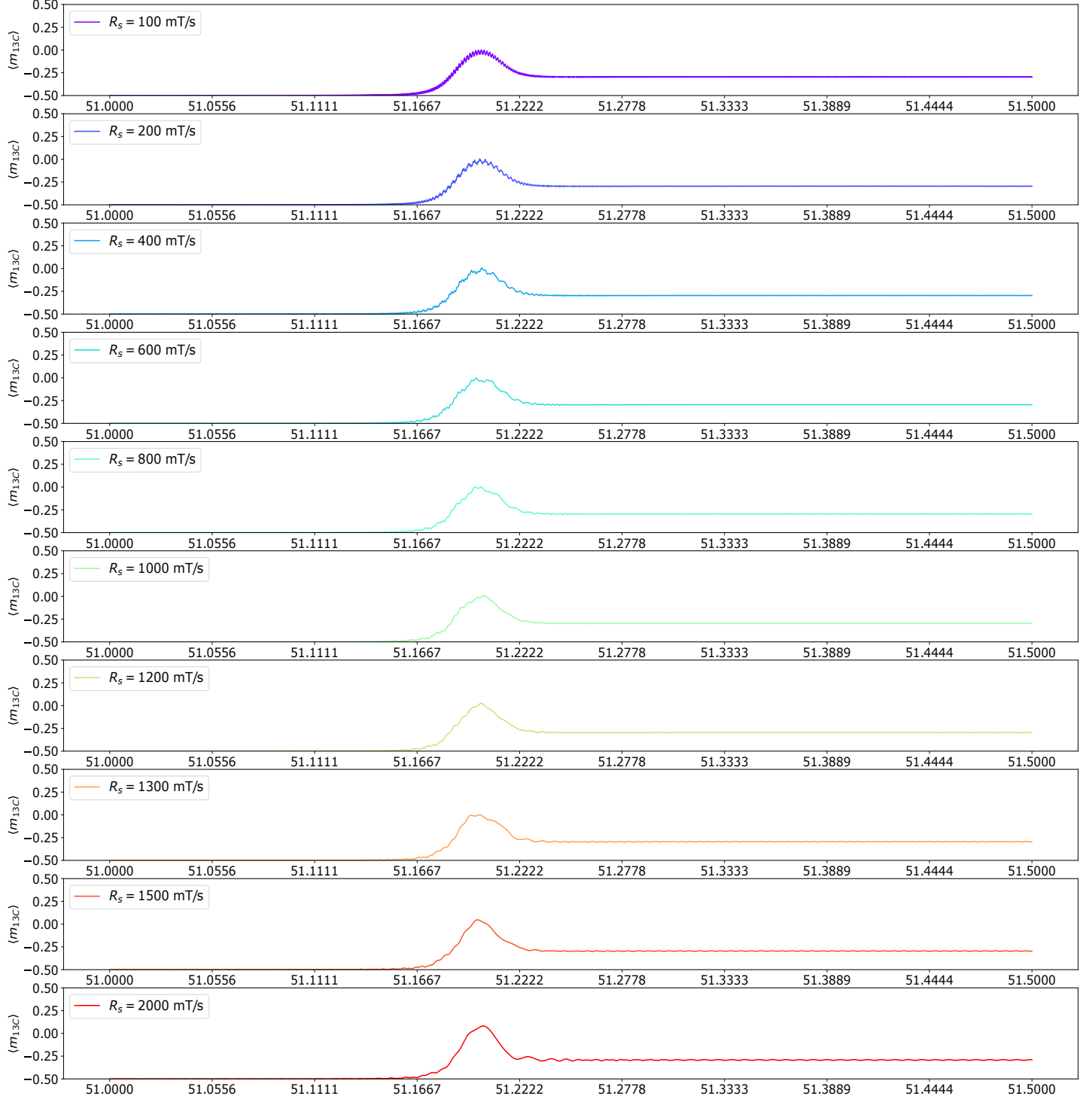

Figure 6.13: Energy eigenvalues of the static Hamiltonian, with dipolar couplings C_{NV-13C}=0.92 MHz and C_{NV-P1}= 1 MHz, as a function of the magnetic fields around the avoided crossing. The color map bar indicates the expectation values of S_z correspondent to P1

Figure 6.14: ^{13}C: Evolution of the expectation values of I_z for different magnetic field sweep rates R_s, magnetic field range $\delta B = 0.5$ mT, coupling constants $C_{NV-13C}=0.92$ MHz and $C_{NV-P1}=1$ MHz, initial state $\Psi_0 = |0, 1/2, \downarrow\rangle$, the figure shows one period of the magnetic field sweep.
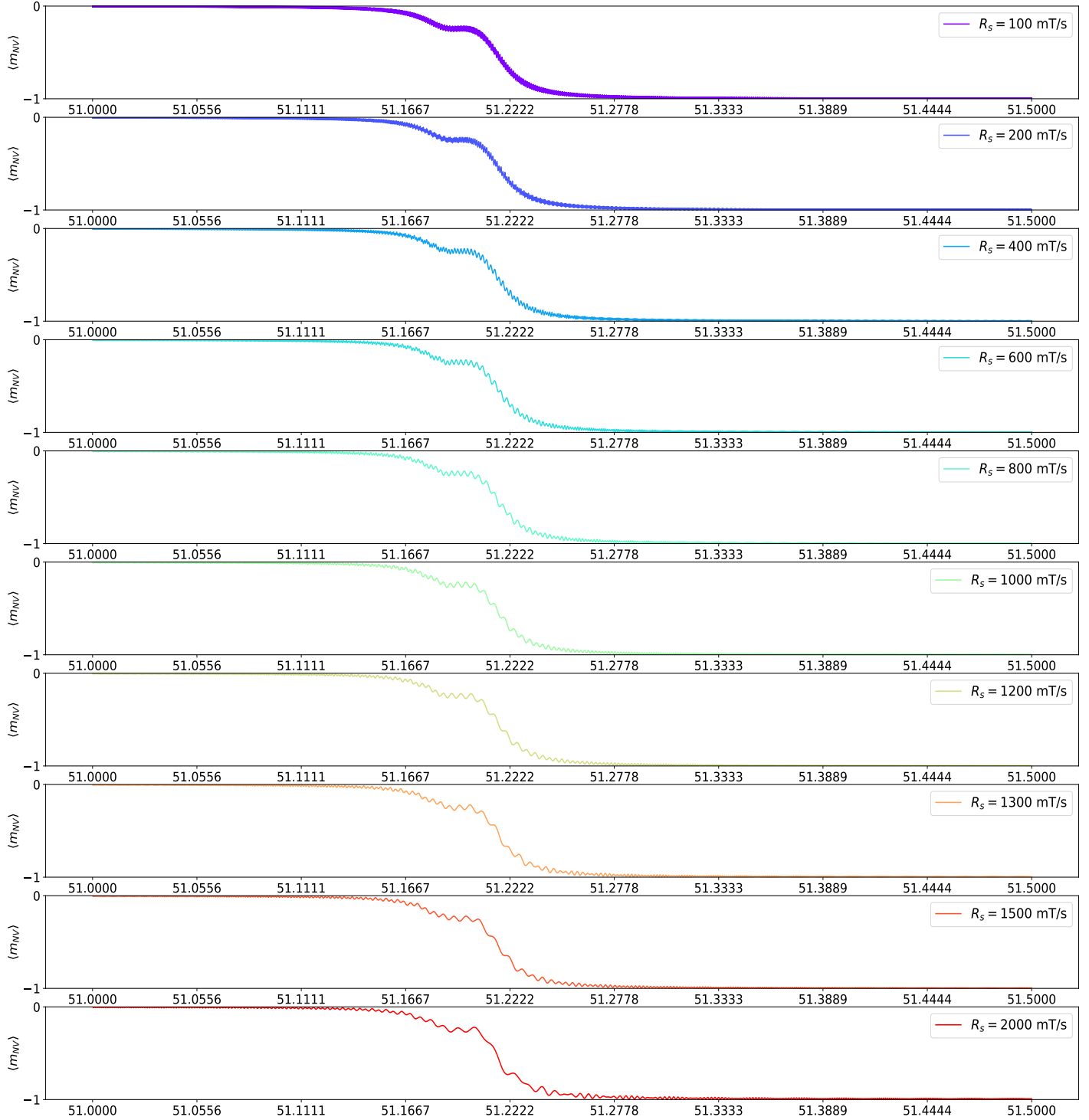
Figure 6.15: NV: Evolution of the expectation values of S_z for different magnetic field sweep rates R_s, magnetic field range $\delta B = 0.5$ mT, coupling constants $C_{NV-13C} = 0.92$ MHz and $C_{NV-P1} = 1$ MHz, initial state $\Psi_0 = |0, 1/2, \downarrow\rangle$, the figure shows one period of the magnetic field sweep.
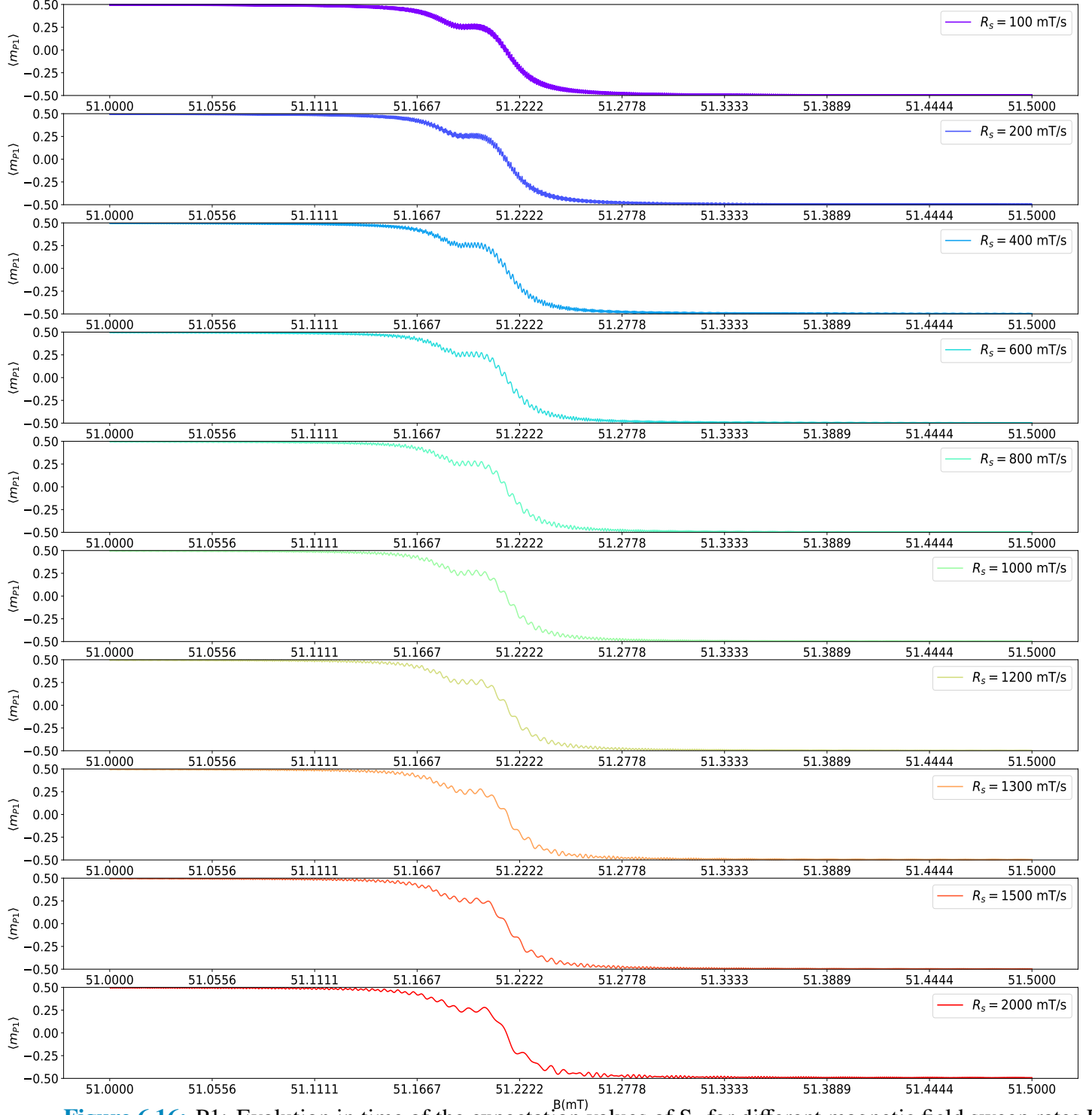
Figure 6.16: P1: Evolution in time of the expectation values of S_z for different magnetic field sweep rates R_s, magnetic field range $\delta B = 0.5$ mT, coupling constants $C_{NV-13C} = 0.92$ MHz and $C_{NV-P1} = 1$ MHz, initial state $\Psi_0 = |0, 1/2, \downarrow\rangle$, the figure shows one period of the magnetic field sweep.

The second simulation case corresponds to C_{NV-P1}= 0.5 MHz, it is noticeable that the energy gaps are smaller than in the case of C_{NV-P1}= 1 MHz, therefore it is expected a more efficient polarization of ^{13}C due to higher non-adiabatic transitions probability. The evolution of I_z showed in 6.18 suggests that the values of R_s that induce the Landau-Zener transition lay between 1000 mT/s and 1600 mT/s, values above or below this range are too fast or too slow to attain dominant Landau-Zener transitions.
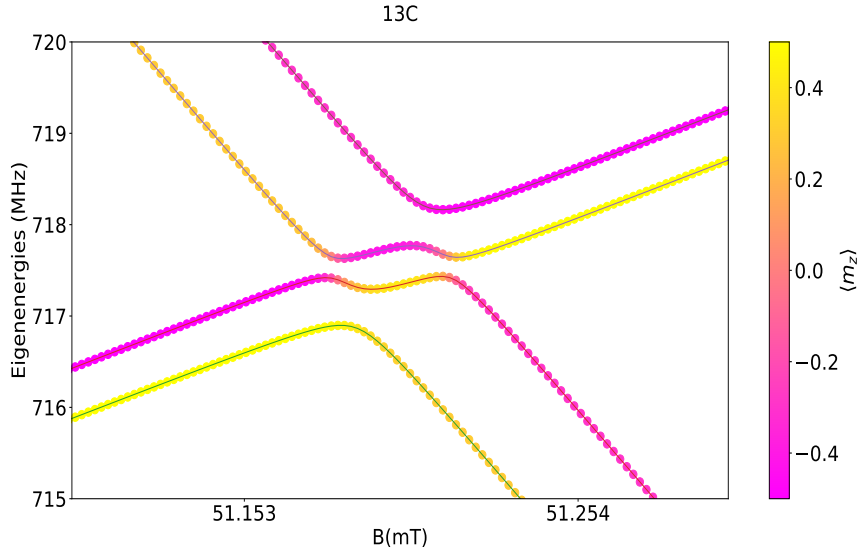

Figure 6.17: Energy eigenvalues of the static Hamiltonian, with dipolar couplings C_{NV-13C}=0.92 MHz and C_{NV-P1}= 0.5 MHz, as a function of the magnetic fields around the avoided crossing. The color map bar indicates the expectation values of I_z correspondent to ^{13}C

The third simulation case corresponds to C_{NV-P1}= 0.16 MHz. In 6.19 the energy gaps are smaller than in the previous cases of C_{NV-P1}, consequently it is still expected that the system exhibits dominant Landau-Zener transitions for certain values of R_s. The evolution of I_z showed in 6.21 shows that the values of R_s that induce the Landau-Zener transitions, in this case, are between 200 and 600 mT/s, values above this range are too fast to attain dominant Landau-Zener transitions.

The last simulation case corresponds to C_{NV-P1}= 0.08 MHz. In 6.20, the energy gaps are are smaller than in the other three cases of C_{NV-P1}. In addition, in the energy diagram it is visible that Δ_0 is much smaller that in the previous case. Considering the crude polarization transfer dynamics model proposed in [45], $\Delta_0 \rightarrow 0$ affects negatively the polarization efficiency. The evolution of I_z showed in 6.22 shows that there are no values of R_s which can optimally polarize the ^{13}C, compared to the previous cases. Nevertheless, R_s= 100 mT/s exhibits some degree of polarization.

From the results showed, the values of C_{NV-P1} that better accomplish ^{13}C polarization by induced Landau Zener transitions are C_{NV-P1}= 0.5 MHz, and C_{NV-P1}= 0.16 MHz. According to 6.2, these coupling parameters correspond to an average defect distance of 12 nm and 8 nm respectively. In practice, in the whole sample the coupling parameters can not be described by a unique average value for C_{NV-P1} and C_{13C-NV}, the defects interact with different coupling strengths which leads to a range of values for the energy gaps Δ_0 and Δ_1 that influence the transitions degree of adiabaticity.
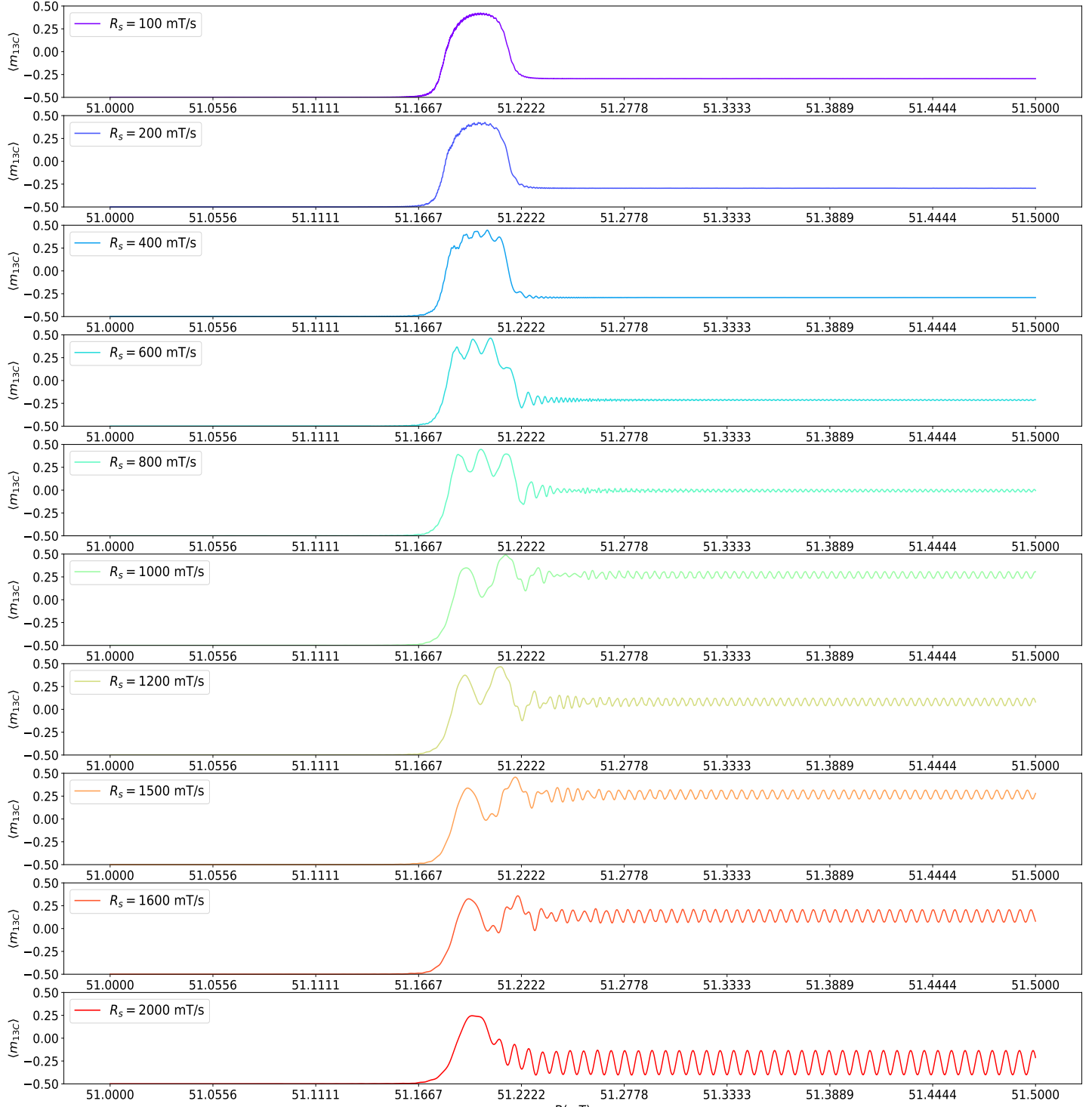
Figure 6.18: ^{13}C: Evolution of the expectation values of I_z for different magnetic field sweep rates R_s, magnetic field range $\delta B = 0.5$ mT, coupling constants $C_{NV-13C}=0.92$ MHz and $C_{NV-P1}=0.5$ MHz, initial state $\Psi_0 = |0, 1/2, \downarrow\rangle$, the figure shows one period of the magnetic field sweep.

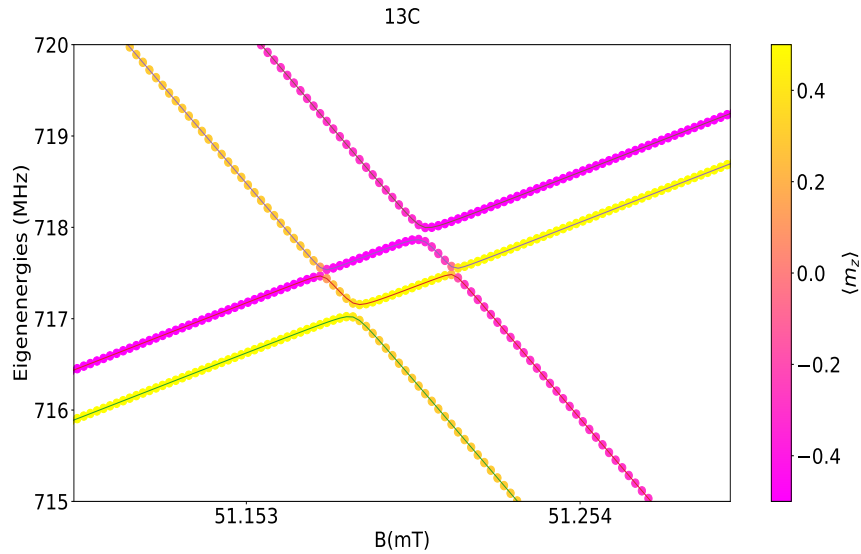**Figure 6.19:** Energy eigenvalues of the static Hamiltonian, with dipolar couplings C_{NV-13C}=0.92 MHz and C_{NV-P1}= 0.16 MHz, as a function of the magnetic fields around the avoided crossing. The color map bar indicates the expectation values of I_z correspondent to ^{13}C

Figure 6.20: Energy eigenvalues of the static Hamiltonian, with dipolar couplings C_{NV-13C}= 0.92 MHz and C_{NV-P1}= 0.08 MHz, as a function of the magnetic fields around the avoided crossing. The color map bar indicates the expectation values of I_z correspondent to ^{13}C
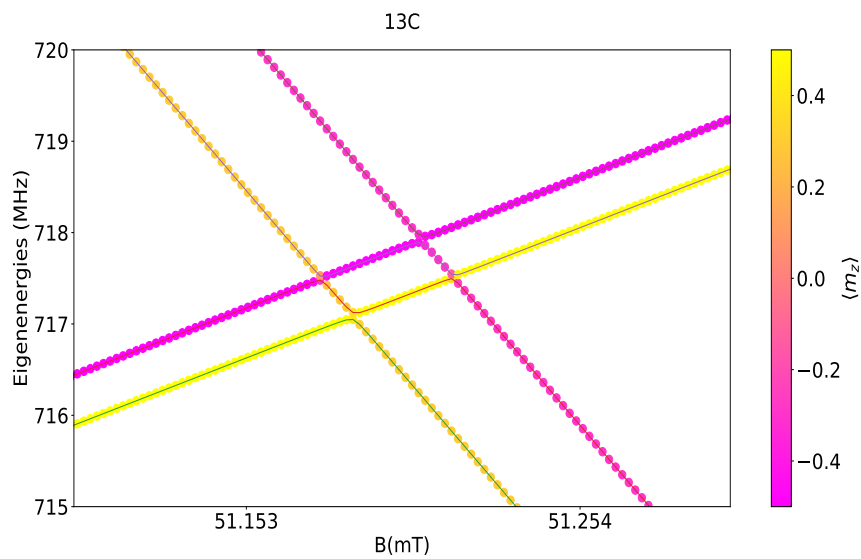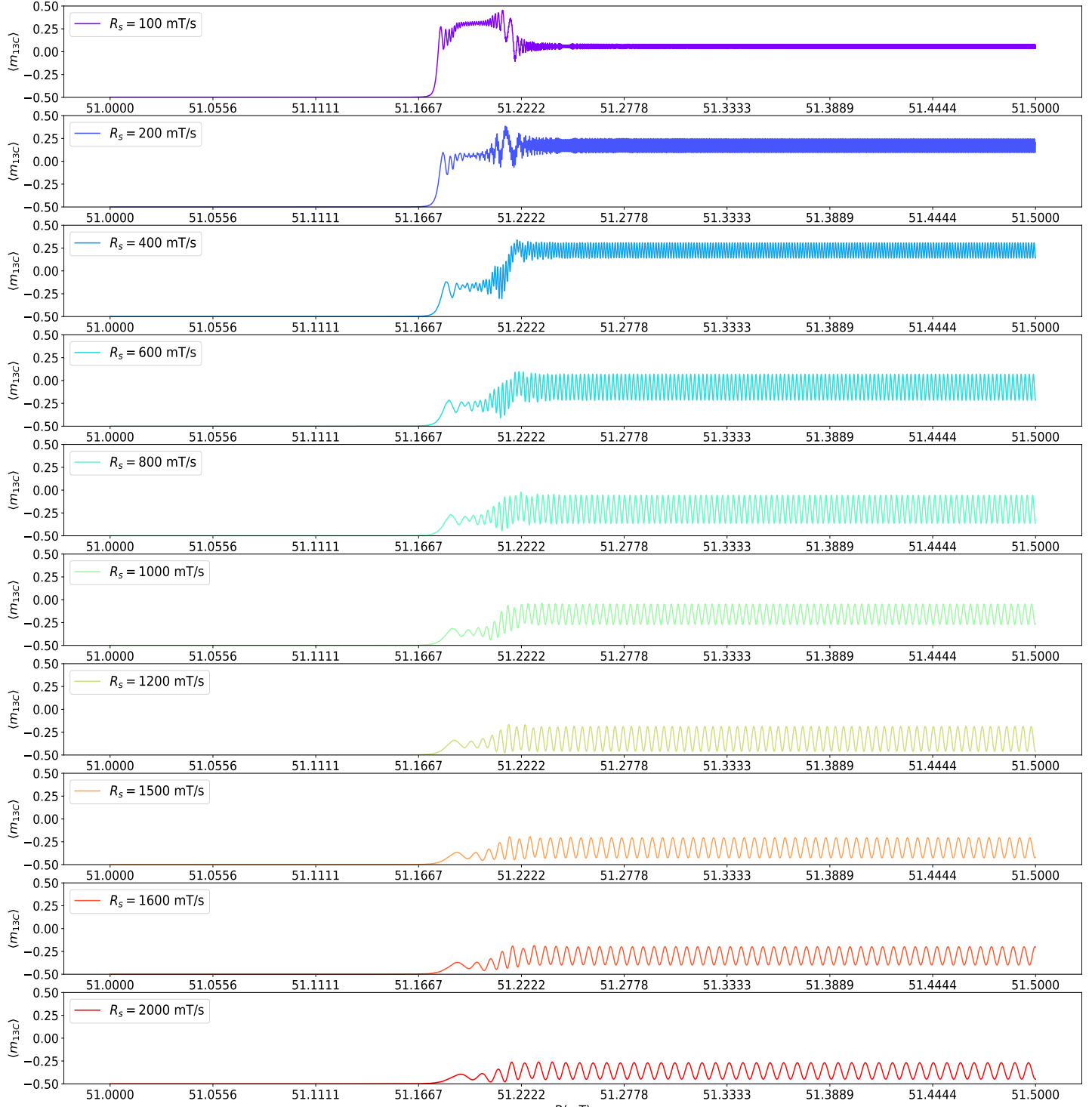
Figure 6.21: ^{13}C: Evolution of the expectation values of I_z for different magnetic field sweep rates R_s, magnetic field range $\delta B = 0.5$ mT, coupling constants $C_{NV-^{13}C}$=0.92 MHz and C_{NV-P1}=0.16 MHz, initial state $\Psi_0 = |0, 1/2, \downarrow\rangle$, the figure shows one period of the magnetic field sweep.
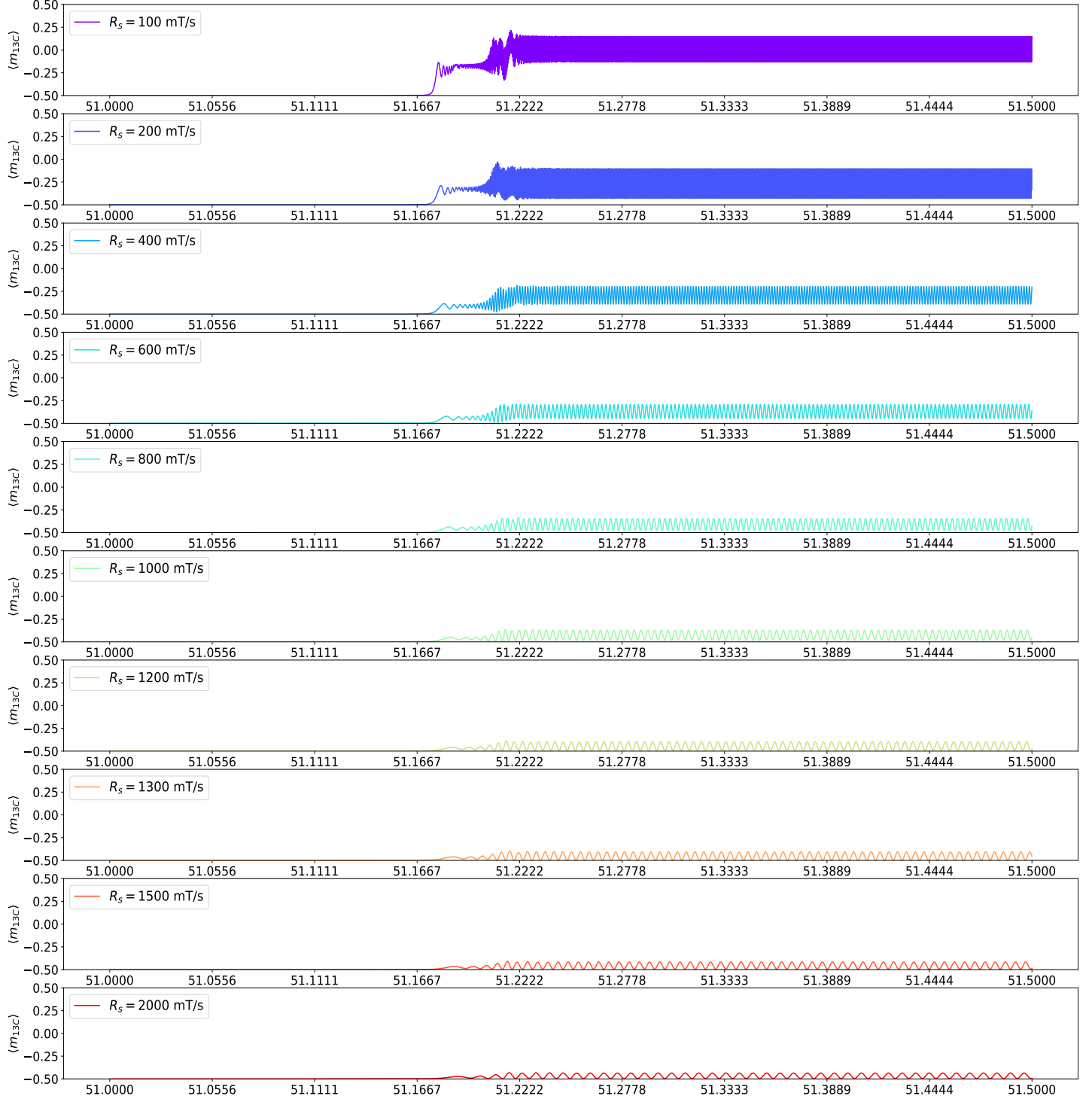
Figure 6.22: ^{13}C: Evolution of the expectation values of I_z for different magnetic field sweep rates R_s, magnetic field range $\delta B = 0.5$ mT, coupling constants $C_{NV-^{13}C} = 0.92$ MHz and $C_{NV-P1} = 0.08$ MHz, initial state $\Psi_0 = |0, 1/2, \downarrow\rangle$, the figure shows one period of the magnetic field sweep.

Chapter 7

Conclusions

During this master thesis, it is worth to remark the challenges present in the process of enhancing NMR signals. The Dynamic Hyperpolarization methods to enhance the NMR signals showed in this master thesis gives advantages in some important aspects because it makes use of the NV center optical polarization property which makes possible the polarization of ^{13}C in diamond by transferring the polarization of the NV centers to the ^{13}C nuclei at room temperature and magnetic fields in the order of millitesla.

Nevertheless, experimental difficulties that were partially not overcame were present during the experimental procedures (e.g sample heating, shuttling system that leads to misalignment of the sample respect to the magnetic fields generated by the Helmholtz-like coil pairs, decrease in the laser power) . In addition, in the case of this work the samples were far from ideal, the concentration of the NV centers measured with CW-EPR experiments showed to be too low, or even not possible to detect in the case of the sample id280 and id277.

On the other hand, a set of measurements that employed static magnetic fields to induce Cross polarization were used to be compared with the simulations performed, giving partially accurate results between the range of 49 mT and 52 mT.

Some calculations regarding the dynamic nuclear polarization by superposing time dependent magnetic field values to static ones were helpful to understand the Landau Zener theory that theoretically explains this technique . It was also useful to gain insight of how important is to chose adequate parameters on the experiments such as the magnetic field sweep rates, static magnetic fields and also the importance of the inter-defect distance parameter that defines the Hyperfine dipolar coupling parameters which make possible the Landau Zener transitions to happen.

Acknowledgements

Selbständigkeitserklärung

Hiermit erkläre ich, Fernanda Toledo, dass ich die vorliegende Masterarbeit selbständig verfasst und keine anderen als die angegebenen Hilfsmittel benutzt habe. Die Stellen der Masterarbeit, die anderen Quellen im Wortlaut oder dem Sinn nach entnommen wurden, sind durch Angaben der Herkunft kenntlich gemacht. Dies gilt auch für Zeichnungen, Skizzen, bildliche Darstellungen sowie für Quellen aus dem Internet. Ich versichere außerdem, dass die vorliegende Arbeit noch keinem anderen Prüfungsverfahren zugrunde gelegen hat bzw. keiner weiteren Stelle zur Prüfung vorgelegt wurde.

Leipzig, 10.11.2022

Fernanda Toledo

Bibliography

[1] Erwin Hahn. Felix bloch and magnetic resonance. *Felix Bloch Memorial Symposium* American Physical Society Washington D.C.*, May 1984.

[2] John Sque. *A first-principles Study on bulk and transfer doping of diamond*. PhD thesis, University of Exeter, 2005.

[3] Diamond structure. tex.stackexchange.com/questions/655049.

[4] E. "Ekimov, V. Sidorov, E. Bauer, and et al". Superconductivity in diamond. *Nature*, 428:542–545, 2004.

[5] *Diamond Films*, chapter 6, pages 389–449. John Wiley Sons, Ltd, 2010.

[6] F. Bundy, H. Hall, H Strong, and et al. Man-made diamonds. *Nature*, 176, 1955.

[7] R S Balmer, J R Brandon, S L Clewes, H K Dhillon, J M Dodson, I Friel, P N Inglis, T D Madgwick, M L Markham, T P Mollart, N Perkins, G A Scarsbrook, D J Twitchen, A J Whitehead, J J Wilman, and S M Woollard. Chemical vapour deposition synthetic diamond: materials, technology and applications. *Journal of Physics: Condensed Matter*, 21(36):364221, aug 2009.

[8] Farida Shagieva. *NMR spectroscopy with single shallow NV centers*. PhD thesis, Universität Stuttgart, 2016.

[9] C Breeding and J Shigley. "the type" classification system of diamonds and the importance in gemology.

[10] Claudia Avalos. *Detection and Polarization of Nuclear and Electron Spins using Nitrogen-Vacancy Centers*. PhD thesis, University of California, Berkely, 2014.

[11] Ralf Wunderlich, Robert Staacke, Wolfgang Knolle, Bernd Abel, and Jan Meijer. Magnetic field and angle-dependent photoluminescence of a fiber-coupled nitrogen vacancy rich diamond. *Journal of Applied Physics*, 130(12), 2021.

[12] M W Doherty, N B Manson, P Delaney, and L C L Hollenberg. The negatively charged nitrogen-vacancy centre in diamond: the electronic solution. *New Journal of Physics*, 13(2):025019, feb 2011.

[13] A. Lenef and S. C. Rand. Electronic structure of the n-v center in diamond: Theory. *Phys. Rev. B*, 53:13441–13455, May 1996.

[14] Christoph Müller. *Sensing single spins with colour centres in diamond*. PhD thesis, Universität Ulm, 2016.

[15] Shuya Ishii, Seiichi Saiki, Shinobu Onoda, Yuta Masuyama, Hiroshi Abe, and Takeshi Ohshima. Ensemble negatively-charged nitrogen-vacancy centers in type-ib diamond created by high fluence electron beam irradiation. *Quantum Beam Science*, 6(1), 2022.

[16] Prerna Baranwal. *Design of FPGA based Arbitrary Waveform Generator*. PhD thesis, 12 2020.

[17] Jianhua Zhang, Cai-Zhuang Wang, Z. Z. Zhu, and V. V. Dobrovitski. Vibrational modes and lattice distortion of a nitrogen-vacancy center in diamond from first-principles calculations. *Phys. Rev. B*, 84:035211, Jul 2011.

[18] Reinis Lazda, Laima Busaite, Andris Berzins, Janis Smits, Florian Gahbauer, Marcis Auzinsh, Dmitry Budker, and Ruvin Ferber. Cross-relaxation studies with optically detected magnetic resonances in nitrogen-vacancy centers in diamond in external magnetic field. *Phys. Rev. B*, 103:134104, Apr 2021.

[19] A. Batalov, C. Zierl, T. Gaebel, P. Neumann, I.-Y. Chan, G. Balasubramanian, P. R. Hemmer, F. Jelezko, and J. Wrachtrup. Temporal coherence of photons emitted by single nitrogen-vacancy defect centers in diamond using optical rabi-oscillations. *Phys. Rev. Lett.*, 100:077401, Feb 2008.

[20] M. Steiner, P. Neumann, J. Beck, F. Jelezko, and J. Wrachtrup. Universal enhancement of the optical readout fidelity of single electron spins at nitrogen-vacancy centers in diamond. *Phys. Rev. B*, 81:035205, Jan 2010.

[21] Philipp Neumann, Johannes Beck, Matthias Steiner, Florian Rempp, Helmut Fedder, Philip R. Hemmer, Jörg Wrachtrup, and Fedor Jelezko. Single-shot readout of a single nuclear spin. *Science*, 329(5991):542–544, 2010.

[22] Eisert. Quantum mechanics lecture notes.

[23] Zeeman effect. https://courses.physics.ucsd.edu/2016/Spring/physics4e/zeeman.pdf.

[24] Jiaxuan Wang, Hui Dong, and Sheng-Wen Li. Magnetic dipole-dipole interaction induced by the electromagnetic field. *Phys. Rev. A*, 97:013819, Jan 2018.

[25] C.P. Slichter. *Principles of Magnetic Resonance*. Advances in Anatomy, Embryology and Cell Biology. Springer-Verlag, 1978.

[26] Frank Neese. Calculation of the zero-field splitting tensor on the basis of hybrid density functional and hartree-fock theory. *The Journal of Chemical Physics*, 127(16):164112, 2007.

[27] Jeschke. Lecture notes physical chemistry iv, 2016.

[28] Hirsch. Quantum physics lecture notes.

[29] J. Keeler. *Understanding NMR Spectroscopy*. Wiley, 2011.

[30] Hyperpolarization (pines lab). https://pines.berkeley.edu/research/hyperpolarization.

[31] F. Bloch. Nuclear induction. *Phys. Rev.*, 70:460–474, Oct 1946.

[32] Sensitivity enhancement of nmr spectroscopy receiving chain used in condensed matter physics.

[33] P.J. Hore, J.A. Jones, and S. Wimperis. *NMR: The Toolkit*. Ocp Series. Oxford University Press, 2000.

[34] Zeeman effect (epr introduction). https://epr.ethz.ch/education/basic-concepts-of-epr/one-elect--in-the-magn--field/zeeman.html.

[35] Peter S.C. Wu and Gottfried Otting. Rapid pulse length determination in high-resolution nmr. *Journal of Magnetic Resonance*, 176(1):115–119, 2005.

[36] Ayush Joshi. Embedded Real Time Partial Discharge Pulse Feature Extraction . Master's thesis, Delft University of Technology, the Netherlands, 2017.

[37] Hall sensor datasheet. https://www.conrad.de/de/p/honeywell-aidc-hallsensor,.

[38] Ran Fischer, Christian O. Bretschneider, Paz London, Dmitry Budker, David Gershoni, and Lucio Frydman. Bulk nuclear polarization enhanced at room temperature by optical pumping. *Phys. Rev. Lett.*, 111:057601, Jul 2013.

[39] Clarence Zener and Ralph Howard Fowler. Non-adiabatic crossing of energy levels. *Proceedings of the Royal Society of London. Series A, Containing Papers of a Mathematical and Physical Character*, 137(833):696–702, 1932.

[40] Zwiebach. Quantum physics iii lecture notes, June 2017.

[41] Jan R. Rubbmark, Michael M. Kash, Michael G. Littman, and Daniel Kleppner. Dynamical effects at avoided level crossings: A study of the landau zener effect using rydberg atoms. *Phys. Rev. A*, 23:3107–3117, Jun 1981.

[42] Goldman. Landau-Zener Transitions and a Feshbach Resonance in Spinor Bose Einstein Condensates . B.S. Thesis, Amherst College, 2008.

[43] J.R. Johansson, P.D. Nation, and Franco Nori. QuTiP 2: A python framework for the dynamics of open quantum systems. *Computer Physics Communications*, 184(4):1234–1240, apr 2013.

[44] Ralf Wunderlich, Jonas Kohlrautz, Bernd Abel, Jürgen Haase, and Jan Meijer. Optically induced cross relaxation via nitrogen-related defects for bulk diamond ^{13}C hyperpolarization. *Phys. Rev. B*, 96:220407, Dec 2017.

[45] Jacob Henshaw, Daniela Pagliero, Pablo R. Zangara, María B. Franzoni, Ashok Ajoy, Rodolfo H. Acosta, Jeffrey A. Reimer, Alexander Pines, and Carlos A. Meriles. Carbon-13 dynamic nuclear polarization in diamond via a microwave-free integrated cross effect. *Proceedings of the National Academy of Sciences*, 116(37):18334–18340, 2019.

[46] Pablo R. Zangara, Jacob Henshaw, Daniela Pagliero, Ashok Ajoy, Jeffrey A. Reimer, Alexander Pines, and Carlos A. Meriles. Two-electron-spin ratchets as a platform for microwave-free dynamic nuclear polarization of arbitrary material targets. *Nano Letters*, 19(4):2389–2396, 2019. PMID: 30884227.

[47] A.M. Panich. Nuclear magnetic resonance studies of nanodiamond surface modification. *Diamond and Related Materials*, 79:21–31, 2017.

[48] Pablo R. Zangara, Jacob Henshaw, Daniela Pagliero, Ashok Ajoy, Jeffrey A. Reimer, Alexander Pines, and Carlos A. Meriles. Two-electron-spin ratchets as a platform for microwave-free dynamic nuclear polarization of arbitrary material targets. *Nano Letters*, 19(4):2389–2396, 2019. PMID: 30884227.

[49] Ralf Wunderlich, Robert Staacke, Wolfgang Knolle, Bernd Abel, Jürgen Haase, and Jan Meijer. Robust nuclear hyperpolarization driven by strongly coupled nitrogen vacancy centers. *Journal of Applied Physics*, 130(10):104301, 2021.